1-1-2005

Fluid-structure interaction considerations for solid rocket motor internal ballistics modeling

Giovanni Montesano
Ryerson University

FLUID-STRUCTURE INTERACTION CONSIDERATIONS FOR SOLID ROCKET MOTOR INTERNAL BALLISTICS MODELING

by

Giovanni Montesano
BEng, Aerospace Engineering, Ryerson University, Toronto, 2003

A thesis
presented to Ryerson University
in partial fulfilment of the
requirements for the degree of
Master of Applied Science
in the program of
Mechanical Engineering

Toronto, Ontario, Canada, 2005

I hereby declare that I am the sole author of this thesis.

I authorize Ryerson University to lend this thesis to other institutions or individuals for the purpose of scholarly research.

Giovanni Montesano

I further authorize Ryerson University to reproduce this thesis by photocopying or by other means, in total or in part, at the request of other institutions or individuals for the purpose of scholarly research.

Giovanni Montesano

Ryerson University requires the signature of all persons using or photocopying this thesis. Please sign below, and give address and date.

FLUID-STRUCTURE INTERACTION CONSIDERATIONS FOR SOLID ROCKET MOTOR INTERNAL BALLISTICS MODELING

Giovanni Montesano

MASc, Mechanical Engineering, Ryerson University, Toronto, 2005

Abstract

A study of the numerical modeling and prediction of nonlinear unsteady combustion instability within the combustion chamber of a solid rocket motor (SRM) is the main objective. The numerical model consists of a three-dimensional finite-element representation of a cylindrical-grain motor, coupled to a quasi-one-dimensional internal ballistic flow (IBF) model, where a quasi-steady rapid kinetic rate burning rate algorithm is used to model the propellant combustion and regression. Fluid-structure-combustion interaction subroutines are also employed to control the simulated motor firings and the data transferred between the fluid, structure and burning rate model components. Results illustrating the significant effects of structural vibrations on the burning rate and consequently the IBF are shown and compared to experimental data. Modeling considerations are illustrated, giving insight into the physical phenomena of SRM combustion instability.

Acknowledgements

I will begin by thanking both Primoz Cresnik and Hamid Ghaemi, technical officers at Ryerson University, for their continuous support and discussions on the structural modeling involved in this thesis; specifically in the area of finite element analysis. The early development stages of the simulation were critical and could not have been made possible without their help. An extra thanks is extended to Mr. Cresnik for his computational hardware support, which aided with the completion of the simulations. Furthermore, I would like to thank both Dr. Kamran Behdinan and Dr. Zouheir Fawaz, my thesis supervisor and co-supervisor, for their structural modeling advice and input on the numerical simulations throughout the development of my research. I would also like to thank Dr. David R. Greatrix, my thesis co-supervisor, for his many hours of discussion on the computational fluids and combustion modeling in this study; his advice and expertise made the outcome of this thesis possible. Finally, I would like to thank Dr. Behdinan, Dr. Greatrix and Dr. Fawaz for giving me the opportunity to pursue my master's degree at Ryerson, and for allowing me to study in this interesting field.

Table of Contents

List of Tables

List of Figures

Nomenclature

Mathematical Symbols

$[]^{-1}$	matrix inverse
$[]^T$, $\{\}^T$	matrix transpose, vector transpose
$\dot{u}$, $\ddot{u}$	time derivatives: velocity ($\dot{u}=du/dt$), acceleration ($\ddot{u}=d^2u/dt^2$)
$\hat{n}$	unit directional vector

English Symbols

A	local motor port area
a	sound speed
a_l	gas axial acceleration, vector sum of propellant lateral/axial acceleration
a_n	propellant surface normal acceleration
$[B]$	element strain-displacement matrix
$\bar{B}$	burning rate vector
$\{b\}$	element body load per unit volume vector
C	structural wave speed, burning rate coefficient
CFD	computational fluid dynamics
CFL	Courant, Friedrichs, Lewy
C_n	IBF Courant number
C_{nFE}	FE Courant number
C_p	gas specific heat
C_s	solid propellant specific heat
$[C]$, $[C']$	system damping matrix: w/ constraints, w/o constraints
$[C^e]$	element damping matrix
c	fluid wave speed
D	dissipation function, particulate phase drag
DOF	degrees-of-freedom
$[D]$	material property matrix
d	local port hydraulic diameter
E	structural – elastic modulus; fluid – total specific energy
FE	finite element
FSI	fluid-structure interaction
$\{F\}$, $\{F'\}$	system force vector: w/ constraints, w/o constraints
$\{F^e\}$	element force vector
$\{F_b\}^e$	element body load vector
$\{F_s\}^e$	element surface traction vector
f	total applied force on point mass, Darcy-Weisbach friction factor
G_a	propellant accelerative mass flux
g_{ax}	axial motor acceleration
h	convective heat transfer coefficient
h^*	zero-transpiration heat transfer coefficient

I	arbitrary integral expression
IBF	internal ballistic flow
$[I]$	identity matrix
i, j, n	indexing variables
$[J]$	Jacobian matrix
K	empirical orientation correction factor
$[K]$, $[K']$	system stiffness matrix: w/ constraints, w/o constraints
$[K^e]$	element stiffness matrix
k	spring stiffness; gas thermal conductivity
$[L]$	three-dimensional operator matrix, factorized lower triangular matrix
$[M]$, $[M']$	system mass matrix: w/ constraints, w/o constraints
$[M^e]$	element mass matrix
m	point mass, total element mass
m_p	particulate mass
$[N]$	shape function matrix
n	empirical pressure exponent
Pr	Prandtl number
p	pressure
$\{p\}$	pressure vector acting on element surface
Q	heat transfer to particulate phase
R	cylindrical-grain motor radius, specific gas constant
Re	Reynolds number
RCM	random choice method
r	radius from motor centerline
r_1, r_2	point mass position in time
r_b	overall burning rate
r_o	base burning rate component
r_p	pressure-dependent burning rate
S	element surface area
SRM	solid rocket motor
s, t, r	local element directions
T	kinetic energy
T_f	flame temperature
T_i	initial propellant temperature
T_s	propellant surface temperature
t	time
t_{al}, t_s, t_p	motor material thickness (aluminium, steel and propellant respectively)
$[t]$	skewed support transformation matrix
U	strain energy (elastic potential)
$\{\bar{U}\}$	free vibration or harmonic analysis amplitude vector (eigenvector)
u	local fluid velocity
u, v, w	structural displacements (Cartesian x, y, z directions)
u_p	particulate phase velocity
$\{u\}$	system displacement vector
$\{\bar{u}\}$	element displacement polynomial in vector form

$\{u^e\}$	element displacement vector
V	potential energy, element volume
v_w	mass injection velocity
W	work done by a force (conservative or non-conservative)
W_n	numerical integration weight factor
x, y, z	Cartesian directions
x	distance aft of motor head-end

Greek Symbols

α, β	Rayleigh damping constants
α_p	particulate mass fraction
β	Newmark stability constant
γ	Newmark accuracy constant, gas ratio of specific heats
ΔH_s	propellant surface heat of reaction
ΔL	minimum element length
Δl	minimum distance between IBF grid nodes
Δp	disturbance strength
Δt	time step
Δx	distance between IBF grid nodes, axial distance between FE nodes
δ_o	reference propellant energy film thickness
ε	propellant surface roughness
$[\varepsilon]$	three-dimensional strain matrix
$\{\varepsilon\}$	strain vector
ζ	system damping ratio
θ_{cr}	skewed support angle offset
κ	local port dilatation
λ	arbitrary flow property (i.e., u, p)
μ	gas absolute viscosity
ν	Poisson's ratio
ξ, ζ, η	arbitrary local element coordinates
ρ	mass density
σ_p	burning rate temperature sensitivity
σ_r, σ_θ	thick-walled cylinder radial and tangential stress
$[\sigma]$	three-dimensional stress matrix
$\{\sigma\}$	stress vector
Φ	arbitrary integral variable
ϕ	normal orientation angle
ϕ_d	displacement angle
χ	arbitrary structural parameter (i.e., u, $\ddot{u}$)
ω	constant angular velocity of spinning motor, system natural frequency

1 Introduction

1.1 Objective

The objective of this study is to predict and simulate the nonlinear unsteady internal ballistic flow (IBF) in the combustion chamber of a solid rocket motor (SRM), with the intention of better understanding the physical phenomena innate to SRM axial combustion instability. This requires understanding the mechanisms that actually sustain the instabilities in a motor. The hypothesis, pertinent to the present study, is that structural oscillations of the motor help to sustain the instability symptoms. Thus, if the numerical results are comparable to the available experimental results, then the theory is accurate; otherwise, there may be further considerations necessary for this type of instability analysis. The significant effects of structural oscillations on the propellant burning rate and the combustor flow will be presented. This will ultimately reveal that the structural vibrations are a major factor in sustaining combustion instability symptoms. Also, as a secondary objective, insight on the modeling of the internal fluid-structure interaction (FSI) of an SRM for this type of complex problem is provided. The structure and fluid present highly nonlinear transient responses, which are difficult to model in a coupled multidisciplinary simulation environment. Also, the FSI of this study is not typical for most applications, due to the regression of the propellant structure. This requires extra considerations for the structure and the fluid, due to the added burning rate model component coupled directly to both. The modeling considerations will primarily focus on the structural component representation; however, insight into other portions of the simulation will also be discussed. Various SRM internal flow models have been previously developed; the goal here is to develop a more accurate model for combustion instability symptom prediction, including relevant structural effects.

1.2 Relevant Literature Review

The instabilities that are native to SRM combustion have been an area of ongoing research, specifically when designing and developing new motors. The instant that an SRM

is disturbed from its normal operational conditions signifies the potential initiation of combustion instability. These disturbances can be caused by two main types of sources, either internal or external. The internal sources include unstable burning of the propellant due to cracks or voids being exposed to the combustion flame in the propellant structure, unburned propellant particles suddenly ignite in the gas path, or due to passage of igniter material, insulation or unburned solid propellant through the nozzle. Conversely, the external sources can include structural vibrations due to an external blast wave or failure of an external structural component, and non-conventional flight vehicle accelerations.[1] A stable motor could potentially become unstable if exposed to any of these disturbances, which could lead to reduced performance, a significant deviation from the desired flight mission, or if prolonged for a long time duration, catastrophic failure of the motor structure components.

A primary symptom of axial SRM combustion instability is a sustained travelling axial pressure wave present in the motor chamber. The pressure waves are typically limited in their amplitude and are commonly accompanied by an overall increase in the base (or dc) chamber pressure. Transverse pressure waves moving in the radial or tangential motor directions can also form as a result of combustion instability. Axial waves travel along the axis of the motor, reflecting off the head-end cap and the nozzle structure, and having a relatively low or intermediate frequency (typically the resonant longitudinal acoustic frequency in the gas cavity). Conversely, transverse waves oscillate at a much higher frequency[2] but more commonly with lower wave amplitudes. Generally, combustion instability is defined by one of two potential categories: linear and nonlinear.[3] A linearly unstable motor experiences a relatively weak initial disturbance, which causes small amplitude pressure waves to oscillate in the motor chamber. These waves eventually grow into stronger sustained pressure or shock waves. Nonlinear combustion instability is initiated when there are stronger initial disturbances (i.e., shock waves) present in the motor combustion chamber. In both cases, the potential result is sustained steep-fronted shock waves oscillating in the combustion chamber. The focus of this study is axial nonlinear combustion instability, where a sustained, large-amplitude shock wave oscillates in the axial direction in the motor combustion chamber. This presented acoustic instability is consistent

with conventional combustion instability theory, since the motor chamber pressure will oscillate by more than 5% of the base chamber pressure in this study.[4]

During unstable motor operation, decay or growth of an axial shock wave in an SRM combustion chamber is governed by the shifting balance between the amplifying and damping factors as the shock wave oscillates. This affects the response of the propellant, which describes the gas mass production or energy release at the propellant surface when it is stimulated by the changing flow conditions.[4] For example, when the pressure peak of the axial shock wave reaches an arbitrary axial location, the instantaneous increase in the local burning rate causes an increase in the local heat transfer or energy into the core flow. Conventional combustion instability theory suggests the following factors that can contribute to amplifying the acoustic energy are: a dynamic combustion process response caused by the flow disturbance, the interactions of flow oscillations with the main flow and influences of fluid dynamic vortexes. Factors that contribute to dissipating acoustic energy include: viscous damping in the boundary layers at the inner propellant walls, damping by particles included in the core flow (particles are expelled from the propellant grain, and are dragged through the chamber), energy from mixing longitudinal and transverse waves being lost through the nozzle, and acoustic energy being dissipated by the viscoelastic solid propellant structure.[4] Moreover, when a shock wave is sustained with a limited amplitude, the energy dissipated is equivalent to the energy added to the motor core flow (i.e., damping factor effects are equal to amplifying factor effects).

There are various mechanisms believed to sustain combustion instability symptoms in SRMs, which influence the acoustic energy dissipation and amplification factors. Traditionally, the mechanism for sustaining an axial wave has been ascribed to an unsteady augmented frequency-dependent pressure-coupled and/or velocity-coupled combustion response (i.e., enhanced local burning rate feeding and sustaining the wave). Recent research (Greatrix[1, 5] and Chopra, Greatrix and Kawall[6]) suggests that there are two other possible mechanisms for sustaining a shock wave in the motor chamber: local propellant burning rate augmentation due to structural acceleration fields, and gasdynamic reflected-wave reinforcement in the vicinity of the nozzle convergence. In the present numerical analysis

the former mechanism is the focus, where the effects of the acceleration field on the local burning rate will be presented. From various experimental tests,[4] motor spinning has shown to augment the propellant combustion, as has the changing of the material for external static-test sleeves during static motor firings. These findings reinforce the fact that acceleration fields caused by structural vibrations do augment the propellant burning rate.

1.3 Current Study Model

There have been various early attempts to accurately model the internal ballistics in a SRM, some empirical and others numerical, one of which was done by Gottlieb and Greatrix.[7] Here a one-dimensional flow model was used to simulate the IBF of an SRM, incorporated with an erosive burning model and an empirical pressure-based burning law that represented the overall combustion model. The propellant burning was solved in conjunction with the one-dimensional flow equations of motion. Also, longitudinal and lateral acceleration effects on combustion were discussed but not included in the model. Later work by Greatrix[8, 9] and Greatrix and Harris[1] attempted to model more accurately the effects of the surrounding structure's radial and axial vibration on the IBF. It was shown that the added structural effects played a significant role in altering the combustion and thus the internal flow. In the numerical model, the structural dynamics were modeled using differential equations based on independent ring elements along the length of the motor. Numerical results proved to be fairly consistent with the presented experimental results, but the structural model used did not provide results for a continuous structure.

Later research by Loncaric, Greatrix and Fawaz[10] attempted to more accurately model the structural portion of the simulation, independently from the internal ballistic portion. Here, a finite element model was used to represent the structural response of the SRM and was coupled with the internal ballistics code during simulation. The propellant regression was also considered in the finite element model, where an adaptive mesh was created over time to mimic the regression of the propellant. This work attempted to simulate the true fluid-structure interaction in the SRM, but there were several assumptions made in the finite

element model that must be noted. Primarily, the finite element model consisted of many independent planar sections along the length of the SRM. There must in fact be some interaction between these sections, especially since longitudinal acceleration effects do to some degree affect the combustion and internal flow in the SRM.

Other researchers[11, 12] have also attempted to model the structure and internal flow of a SRM in order to run a fully coupled fluid-structure interaction simulation. Various attempts have been made to represent the propellant regression through an adaptive mesh generation, in order to accurately run a simulation. It is the motivation of this investigation to create an accurate structural finite element component for the SRM model, and perform an accurate simulated motor firing. The SRM physical processes can be highly complex, including nonlinear and unsteady behaviour. This naturally requires some assumptions to be made in order to produce a feasible simulation.

The simulation model of this study is comprised of three main components: a three-dimensional structural solver, a one-dimensional IBF solver and a burning rate algorithm. The structural solver is employed to provide an accurate response for the SRM structure (see Chapter 2), since both longitudinal and radial acceleration fields affect the burning rate algorithm, as discussed in Chapter 3. The IBF solver follows the work of Greatrix and Harris[1] for the analysis of unsteady flow in a cylindrical SRM. The structural component is indirectly coupled to both the burning rate algorithm and the IBF component, while the IBF and burning rate components are directly coupled (see Chapter 4). The main focus will be the analysis and prediction of combustion instability for a cylindrical-grain SRM. Various parameters such as numerical constants and system damping terms will be altered in order to extract accurate results. Also, the effects of changing the motor structural geometry and material properties will be considered. The desired results from the various simulations are mainly the pressure-time profiles at various axial locations in the chamber, for example, the head-end of the motor or, say, the grain mid-point. Other results include both structural radial and axial displacement and acceleration values at key points in the motor, and burn rate values from various locations in the motor as well (see Chapter 5). The structural effects on the motor simulation are of key interest and will be emphasized.

2 Structural Component Modeling

2.1 Introduction

The structural finite element (FE) component is the main focus of this study. It is coupled with the existing IBF and burning rate components, along with coupling algorithms to complete the SRM simulated firing. This chapter details the FE modeling considerations, as well as the structural governing equations. The reference SRM material properties and geometry are presented along with the FE structural discretization. The FE modeling and governing equations are also presented, along with the different solutions to these equations. Preliminary results for the FE component will be included and compared to output from commercial software, in order to establish its validity. The FE considerations toward the overall simulation will also be discussed here.

2.2 Structure Representation

2.2.1 Material Properties and Geometry

The SRM model used for this analysis is that of a cylindrical grain, which was extracted from the literature.[1] There is extensive experimental data in the literature for this particular motor, thus the numerical simulation predicted results can be compared to the experimental results. This is one of the main reasons this particular motor is chosen for this study. The specific material properties and geometry are summarized below in Table 2-1. Note that the steel and aluminium alloy material properties have typical values. However, the propellant material has a Poisson's ratio close to 0.5 with its behaviour characterized as a nonlinear viscoelastic material. For the purposes of this analysis, the material is treated as linearly elastic since the exact response of the propellant structure is not fully known.[13] Also note that the propellant grain length is 0.52 m, i.e., the distance from the head-end of the SRM to the grain end in the vicinity of the nozzle convergence. A schematic representation

of the SRM is illustrated in Figure 2-1, which shows a side section of the geometry and includes the various components of the motor physical structure.

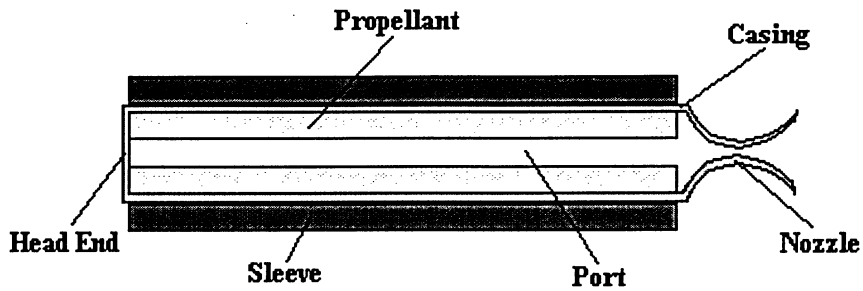

Figure 2-1 Cylindrical SRM component schematic

Steel (Sleeve)		
Modulus of Elasticity (E_s)	200	GPa
Poisson's Ratio (ν_s)	0.3	-----
Density (ρ_s)	7850	kg/m^3
Inner Wall Radius (R_{is})	33.67	mm
Thickness (t_s)	4.67	mm
Aluminium (Casing)		
Modulus of Elasticity (E_{al})	80	GPa
Poisson's Ratio (ν_{al})	0.33	-----
Density (ρ_{al})	2700	kg/m^3
Inner Wall Radius (R_{ial})	32.4	mm
Thickness (t_{al})	1.27	mm
Propellant (Grain)		
Modulus of Elasticity (E_p)	0.045	GPa
Poisson's Ratio (ν_p)	0.497	-----
Density (ρ_p)	1730	kg/m^3
Inner Wall Radius (R_{ip})	18	mm
Thickness (t_p)	14.4	mm

Table 2-1 Cylindrical SRM material properties and geometric measurements

Consider the fact that the propellant material potentially possesses nonlinear viscoelastic behaviour. Viscoelastic materials typically exhibit a combination of both elastic and viscous mechanical characteristics, where deformation is not totally recoverable.[14] Since all the deformation in the propellant is not recoverable, any propellant damage due to manufacturing or transportation may affect the response of the propellant during operation. This phenomenon makes it difficult to predict the physical properties and behaviour of the propellant material. Also, consider the fact that the propellant is a rubber-like material and nearly incompressible.[4] For this reason, its modulus of elasticity is low and it has the ability to deform to very large deformations and almost return to its original form upon unloading. This represents a geometric nonlinearity because the stiffness is a function of the strain or magnitude of the deformation. Typical SRM structural analysis ignores any nonlinear effects due to the increased complexity. The problem is typically reduced to a linear elastic analysis since a sophisticated nonlinear model is currently unavailable,[4] which is evidently the case for the present analysis.

Moreover, the three-dimensional nature of the motor requires the modeling of the end structural components, mainly the head-end and nozzle-end. The head-end structure is essentially a flat plate acting as an end-cap; however, due to the external steel static-test sleeve added to simulate a motor on a static test stand, further structural modeling must be considered. For example, load cells are typically used at the head-end to measure the thrust profile during experimental firing, and thus must be considered for design. At the nozzle-end, a converging-diverging nozzle open to the atmosphere is the sole structural component past the end of the propellant grain (refer to Figure 2-1).

2.2.2 SRM Numerical Representation

In order to numerically represent the SRM structure, the physical structure must be simplified to allow for the approximate numerical techniques (i.e., FE analysis) to be used. One simplification is to omit any detailed modeling of the head-end and nozzle-end structures; these components can be represented by simplified boundary conditions. The

reason for this simplification is to avoid any difficulties with the complex end-structures and motor boundaries. The three-dimensional idealization of the cylindrical grain SRM is shown in Figure 2-2.

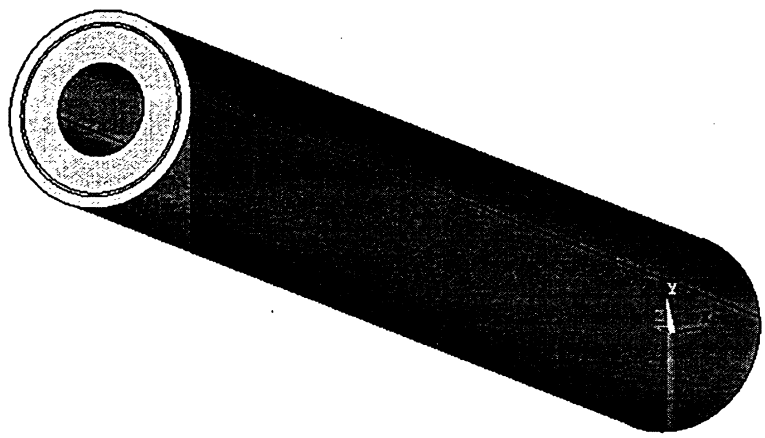

Figure 2-2 SRM structure idealization

With the idealized structure defined, the FE discretization can begin, which is the first step in any FE structural analysis. The detail of the type of elements used will be discussed in Section 2.3.2; here, the discretization (i.e., structural meshing) will be shown, as will the use of structural symmetry. For this particular study, structural symmetry can be utilized for two main reasons: the quasi-one-dimensional nature of the flow algorithm allows for constant pressure around the periphery at each axial location of the motor, and the cylindrical grain geometry is rotationally symmetric. In order to have a plane of symmetry or rotational symmetry, a structure must have symmetry of shape, material properties and support conditions.[15] This is shown in the idealized SRM structure illustrated above. Also, since the flow algorithm is one-dimensional in nature, i.e., has a linear pressure distribution in the axial direction of the SRM model, it allows for ease of implementing the periodically rotational structure in the overall simulation. The use of symmetry reduces the total degrees-of-freedom of the structural mesh, which is necessary to reduce the overall computation time. Another method of reducing the total degrees-of-freedom would be to reduce the number of elements in the structural mesh, and thus the number of nodes in the system. The downside of making the element mesh unrefined is a loss in accuracy, which is not the case when using

symmetry. Simplifying a structure with the use of symmetry maintains the accuracy of the solution relative to an analysis with the entire structure, but reduces the computational effort significantly.

With the idealized SRM structure reduced due to symmetry, the model can now be meshed into finite elements. There are a number of three-dimensional structural elements available;[15, 16] however, for this particular study a structured mesh is desired for reduced complexity in the overall simulation. A structured mesh consists of having a fixed number of elements in each Cartesian direction of the motor structure, versus a random unstructured mesh. Elements that can easily be implemented into a structured three-dimensional mesh are the hexahedral family of elements.[16] This allows for a fixed number of elements in the radial, tangential and axial directions of the model. Hexahedral elements are also preferred for vibration analysis over triangular three-dimensional elements because of their superior performance.[16] The use of isoparametric formulation also allows the hexahedral elements to be used around curved boundaries. This will be discussed further in Section 2.3.

There are many different structural meshes used in this study, some being fine and others coarser. One sample mesh for the partial section of the cylindrical grain SRM is illustrated in Figure 2-3. Note the use of symmetry previously discussed is shown with the use of only an 18° section of the motor. The three-dimensional hexahedral element mesh is created using the meshing tools in ANSYS, a commercial FE package.[17] The reason for this is to avoid any difficulties in creating a custom three-dimensional meshing algorithm. This would have been a complex task, and since it is not a primary objective of this study, the commercial package is used. Batch files with parametric flexibility enable a mesh to be created with ease in the ANSYS program. Various geometric, element, and mesh density parameters are defined at the beginning of the file, and the mesh is then generated automatically. The ANSYS batch file also outputs the nodal coordinates and the element connectivity tables into files, which are then used as input files for the overall simulation. The nodal coordinates are based on a Cartesian coordinate system in three dimensions (i.e., *x-y-z*) with the same reference origin used in the simulation. Also, the element connectivity

table entries, which are dependent on the specific hexahedral element used, defined the node numbers connected to each element in the mesh.

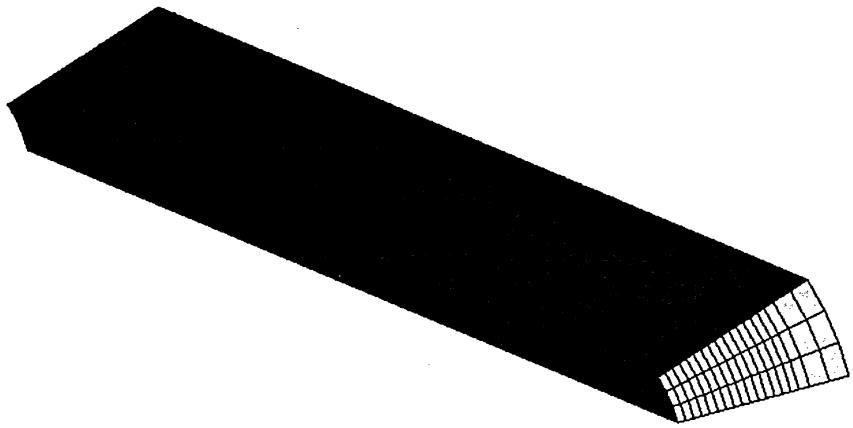

Figure 2-3 Cylindrical SRM 18° section FE mesh

The mesh has a direct affect on the response of the structure and the performance of the FE transient solvers. Thus, as with any structural analysis, various meshes are used to determine which is preferable with respect to accuracy and solution time. This is the trade-off existing with any FE analysis, where the number of elements in the mesh must be increased to a point where high accuracy is reached, but not too high as to be detrimental to computation time. The effects of element number and size in the structural mesh are compared in Section 2.6.1, where various meshed models are subjected to the same loading condition and their results compared. Here, some of the meshes to be used in this study for the cylindrical grain motor are presented in Table 2-2. Each mesh is similar to that shown in Figure 2-3, with a different number of axial and radial elements as indicated. Note that some of the meshes listed also have a head-end plate added to the mesh. Also, all meshes listed are for the 8-node hexahedral element, where identical meshes using the same number of elements are also created using the 20-node hexahedral element. The element meshes are identical, but because of the higher order 20-node element, the number of nodes in the mesh is higher.

Total Number of Nodes	Total Number of Elements	Number of Elements in Radial Direction: Propellant	Number of Elements in Radial Direction: Aluminium	Number of Elements in Radial Direction: Steel	Number of Elements in Axial Direction
882	520	8	2	3	20
2142	1300	8	2	3	50
1890	1160	20	3	6	20
2424	1400	4	1	2	100
19796	14400	30	3	15	100

Table 2-2 Various element meshes used in this study

2.2.3 Assumptions and Boundary Conditions

As with most structural numerical models, assumptions are made in order to simplify the analysis and to maintain low computational requirements for the numerical solvers. Other assumptions are made due to lack of a more sophisticated model at this time. Any assumptions warranted in this study are discussed in the subsequent paragraphs.

The more significant assumptions are with respect to the material properties and behaviour of the propellant structure. It is assumed that all materials behave in a linearly elastic and isotropic manner. For the aluminium casing and steel sleeve, these properties most definitely hold true since they are both exposed to stresses well below their yielding limits; however, this may not be the case for the propellant. Since the propellant most definitely behaves as a nonlinear viscoelastic material, the linear elastic assumption may not accurately capture the response of the structure over time. The main reason for this simplification is to reduce the complexity of the analysis, and to also reduce computation time of the simulation; a nonlinear analysis could potentially increase the solution time by over 100 times, which is not economical.[15] There are some linear viscoelastic formulations that can be used in lieu of a nonlinear viscoelastic model; however, accuracy is very problem dependent. Also, since the propellant is a composite material and may experience different values of modulus under various directional loading conditions,[4] the value for modulus of elasticity may not be accurate and the isotropic material assumption may be invalid. In

addition, since the propellant is a composite, the structure may not necessarily exhibit homogeneous material properties. These assumptions are made primarily for simplicity, since the exact material properties of the propellant used are not known, as previously mentioned.

Also, since the propellant is nearly incompressible (i.e., $\nu \sim 0.5$), the strain will be relatively small. A typical linearly elastic analysis would overestimate the deformation of the propellant structure, which is why a nonlinear type of analysis or penalty constraint formulation is required. This type of formulation may not necessarily provide a better solution since it is dependent on the types of elements and time integration scheme used, which is the reason it is omitted here.[15] Also, because the motor chamber pressures experienced in the present analysis are much lower than the assumed elastic modulus used, the propellant strain would actually remain low with a linear elastic analysis, and the deformations may not be over-estimated. Up to this date of reporting, development of good finite elements for modeling of three-dimensional nearly-incompressible media is an active area of research.[15]

Other less significant assumptions are made primarily because their influence on the overall simulation are not as large a factor as are the propellant material property assumptions discussed. One such assumption is to neglect the SRM core flow temperature effects on the structure. Since the propellant has a very high specific heat capacity, a very low thermal conductivity, and the burning of the propellant reduces the heat penetration to a very small zone, neglecting any heat transfer to the propellant is a reasonable approximation. For this reason, the propellant grain acts as an insulator to the surrounding structure. Another assumption is to neglect any structural shear loads caused by the core flow. This assumption is also reasonable because the shear loads acting on the nearly incompressible propellant are negligible compared to the normal loads (i.e., due to pressure). Any externally applied shear forces due to aerodynamic loading are not considered in this study.

Other assumptions include keeping the propellant burning rate constant over a single time step. This is reasonable since the time steps used in this study are small, due to the

explicit flow algorithm. Also, the structural damping ratio and natural frequencies are assumed constant over the entire simulation, which is not necessarily accurate. As the propellant burns away during motor operation, the damping properties of the structure probably change. This would require eigenvalue extraction and damping ratio change calculations to be done at every time step, which would not be economical. It is also assumed that the elements used in the FE mesh have constant mass and stiffness properties throughout the unsteady portion of the simulation. Since the unsteady portion is simulating a relatively short actual time range, and elements with transient mass and stiffness properties would cause both numerical and modeling difficulties, this is deemed the best choice for this study. Finally, it is assumed that the material contacts between the aluminium casing and both the steel sleeve and the propellant grain are ignored. This is required to keep the analysis linear, since modeling the contacts between the materials would lead to nonlinear analysis. This is a fairly good assumption because relative motion between the various materials is negligible in this study, thus coinciding the nodes on the boundaries between the different materials will represent the physical problem with enough accuracy.

For any type of finite element analysis, the boundary conditions must be specified and modeled to accurately represent the physical problem. In this study, the main boundary conditions are those that restrict rigid body motion on the finite element model (including the head-end and nozzle-end), and the external loads applied to the structure. The structural external loads applicable to this study are the internal chamber pressure acting on the inner propellant surface, the external atmospheric pressure acting on the outer steel surface, the longitudinal acceleration on the SRM caused by axial flight acting as a structural body load, and the potential spinning of the motor about the longitudinal axis also acting as a structural body load. Since the internal chamber pressure acting on the propellant surface is a gauge pressure relative to standard sea level and the SRM during a static firing is at constant atmospheric pressure, the effects of the external atmospheric pressure can be ignored. This is done in the present study, which is depicted in Figure 2-4 showing only a 90° two-dimensional section of the motor. The internal chamber pressure is of prime importance because the shock wave development inside the SRM chamber will directly impact the structure. Note that when simulating a flight case, the change in external atmospheric

pressure does need to be accounted for. Furthermore, spinning of the motor with angular speed of ω is also illustrated below, while any longitudinal acceleration due to flight would be directed towards the head-end of the motor. Details of the formulation of the finite element force vector are found in Section 2.4, while details of the pressure interpolation from the flow calculations applied to the finite element model are found in Chapter 4.

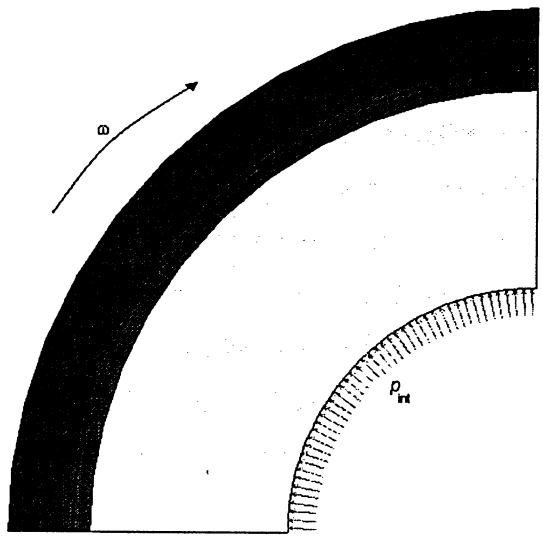

Figure 2-4 SRM applied loading

The main rigid body constraints on the motor due to the symmetry of the structure are those restricting any normal displacements on the planes of symmetry. As mentioned, use of symmetry is necessary in order to reduce the total degrees-of-freedom of the structure, which consequently reduces the computation time. Referring to Figure 2-5, it can be seen that all nodes on both symmetry planes cannot move in the normal direction, on the respective planes. This restricts rigid body motion in the tangential direction. The motor is however free to move in the radial direction, which is consistent with the physical SRM.

With respect to axial motion, the motor ends must be treated accordingly in order to prevent rigid body motion and to accurately represent the physical system. Whether the simulation is of a motor on a static test stand or in flight, the structure and internal flow move together relative to any external motion or acceleration. This is depicted in Figure 2-6 (a) and (b), where a schematic represents both the static test and the in-flight cases, respectively.

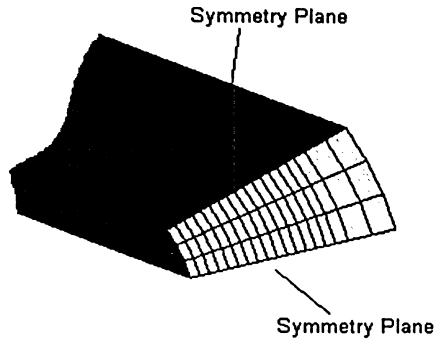

Figure 2-5 Planes of symmetry

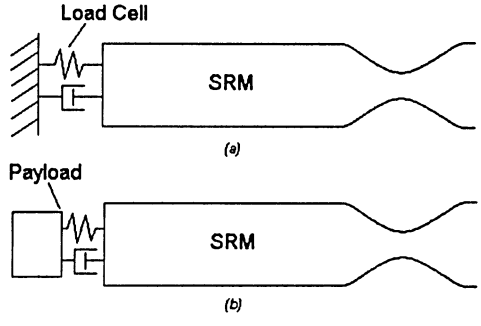

Figure 2-6 Axial motion: (a) static test stand, (b) in-flight

In both cases, the external axial acceleration relative to either the load cell or payload can be applied to the motor structure as a body load. This enables the head-end of the motor to be fixed from moving in the axial direction, eliminating any axial rigid body motion. Also since external aerodynamic loads are not being considered in this study, the structural model does correctly represent the physical motion of the motor relative to the internal flow. Note that any gap between the propellant and the head-end plate is neglected for this study, as shown below in Figure 2-7 (a). With respect to the nozzle-end structure, the nozzle itself is not modeled in this study (treated as rigid) in order to simplify the finite element model. However, the end grain of the propellant is free to move in the axial direction. A locally applied pressure on the end face of the propellant grain is applied normal to the surface as shown in Figure 2-7 (b). Since the radial motion of the SRM structure is more significant than the axial motion, the omitted nozzle structure will not be a large factor in the simulation. Also, since the flow past the nozzle structure is open to the atmosphere, there is no radial constraint on the structure, except that from the steel sleeve modeled in this study.

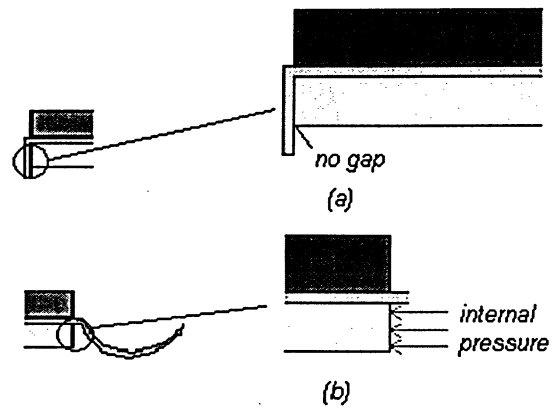

Figure 2-7 SRM model: (a) head-end, (b) nozzle-end

Moreover, at the motor head-end a flat plate is added in the structural model for each simulation acting as an end-cap. This is necessary to represent the locally reduced radial response caused by the head-end plate in the physical model, which is analogous to typical end-capped pressure vessel structures.[18] This is also shown in Figure 2-7 (a), where the aluminium end-cap is attached to the main aluminium casing.

2.3 Derivation of FE Equations of Motion

2.3.1 Physical Problem

After the physical structure is represented by an equivalent numerical model, the next step in any structural vibration problem is to formulate the equations of motion. There are various techniques available to derive the equations of motion correctly. The method presented here is known as Hamilton's Principle.

First, consider a mass, m, which contains a force f_T acting on it that causes a displacement of u, as shown in Figure 2-8.

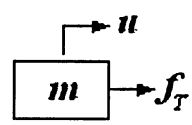

Figure 2-8 Physical mass representation

The force represents the sum of all the applied forces, both conservative and non-conservative. The work done by a conservative force in moving a mass from one point to another depends only on the position of the two points, and is independent of the path taken.[16] The work done by a non-conservative force does depend on the path, these forces being energy dissipating forces (i.e., friction forces or external forces imparting energy to the system). The work, W, done by a conservative force can be obtained from the change in potential energy, V from position r_1 to r_2 via:[16]

$$W = \int_{r_1}^{r_2} f dr = -\left(V(r_2) - V(r_1)\right) \quad so \ that \quad \delta W = -\delta V \tag{2.1}$$

The potential energy generally considered is elastic potential or strain energy, U. If a simple stretched spring is considered, the strain energy is equal to $U = \frac{1}{2} k u^2$, where k is the spring stiffness factor. Using the principle of virtual displacements for the system shown above with Newton's second law yields the following equation of motion:[16]

$$f_T \delta u - m\ddot{u}\delta u = 0 \tag{2.2}$$

The $\ddot{u}$ term is the mass acceleration, and with $\delta W = f_T \delta u$ the equation becomes:

$$m\ddot{u}\delta u = m\frac{d}{dt}(\dot{u}\delta u) - m\dot{u}\delta\dot{u} \tag{2.3}$$

Equation (2.3) can be expressed as $m\ddot{u}\delta u = m\frac{d}{dt}(\dot{u}\delta u) - \delta T$, where the kinetic energy is given by $T = \frac{1}{2} m\dot{u}^2$, and the $\dot{u}$ term is the mass velocity. Further simplification results in the equation of motion, given here as:

$$\delta T + \delta W = m\frac{d}{dt}(\dot{u}\delta u) \tag{2.4}$$

When the above equation is integrated between two time points the equation yields the general form of Hamilton's principle as:

$$\int_{t_1}^{t_2} \left(\delta(T - U) + \delta W_{nc}\right) dt = 0 \tag{2.5}$$

The δW_{nc} term represents non-conservative work usually imparted to the system by a dissipation function representing damping, but varies for a particular problem. The application of this principle leads directly to the equations of motion and to the boundary terms for a given domain, and it can also be applied to multiple-degree of freedom systems

and continuous systems. The application of Hamilton's Principle will now be shown for a three-dimensional hexahedral element.

The general governing energy equation was obtained from the energy functions of a system (i.e., U, T and W_{nc}). Now, the energy functions will be derived for the three-dimensional hexahedral elements to be used in this study. The assumptions made here are that all materials behave in a linearly elastic manner, thus the stress-strain and strain-displacement relationships are linear. The state of stress defined for a three dimensional elastic body is given by:[16]

$$[\sigma]=\begin{bmatrix}\sigma_x & \tau_{xy} & \tau_{xz}\\ \tau_{yx} & \sigma_y & \tau_{yz}\\ \tau_{zx} & \tau_{zy} & \sigma_z\end{bmatrix} \tag{2.6}$$

The state of strain is similarly given by:

$$[\varepsilon]=\begin{bmatrix}\varepsilon_x & \gamma_{xy} & \gamma_{xz}\\ \gamma_{xy} & \varepsilon_y & \gamma_{yz}\\ \gamma_{xz} & \gamma_{yz} & \varepsilon_z\end{bmatrix} \tag{2.7}$$

The matrix entries of Equations (2.6) and (2.7) represent the normal and shear stresses and strains, in a global Cartesian coordinate system (x, y, z). The stress-displacement relationships for an infinitesimal three-dimensional solid are given by:

$$\varepsilon_x = \frac{\partial u}{\partial x} \tag{2.8a}$$

$$\varepsilon_y = \frac{\partial v}{\partial y} \tag{2.8b}$$

$$\varepsilon_z = \frac{\partial w}{\partial z} \tag{2.8c}$$

$$\gamma_{xy} = \frac{\partial u}{\partial y} + \frac{\partial v}{\partial x} \tag{2.8d}$$

$$\gamma_{xz} = \frac{\partial u}{\partial z} + \frac{\partial w}{\partial x} \tag{2.8e}$$

$$\gamma_{yz} = \frac{\partial v}{\partial z} + \frac{\partial w}{\partial y} \tag{2.8f}$$

Here u, v, w are the displacement components in the x, y, z directions respectively.

Consider a three-dimensional solid of volume V enclosed by a surface S. The strain energy, based on the state of stress and strain mentioned above, is given by:[16]

$$U = \frac{1}{2}\int_V \left(\sigma_x\varepsilon_x + \sigma_y\varepsilon_y + \sigma_z\varepsilon_z + \tau_{xy}\gamma_{xy} + \tau_{xz}\gamma_{xz} + \tau_{yz}\gamma_{yz}\right) dV = \frac{1}{2}\int_V \{\sigma\}^T \{\varepsilon\}\, dV \tag{2.9}$$

where $\{\sigma\}^T = \lfloor \sigma_x \quad \sigma_y \quad \sigma_z \quad \tau_{xy} \quad \tau_{xz} \quad \tau_{yz} \rfloor$ and $\{\varepsilon\}^T = \lfloor \varepsilon_x \quad \varepsilon_y \quad \varepsilon_z \quad \gamma_{xy} \quad \gamma_{xz} \quad \gamma_{yz} \rfloor$. The stress-strain relationship governed by Hooke's law is $\{\sigma\} = [D]\{\varepsilon\}$, where for an isotropic material $[D]$ is given by:

$$[D] = \frac{E}{(1+\nu)(1-2\nu)} \begin{bmatrix} (1-\nu) & \nu & \nu & 0 & 0 & 0 \\ \nu & (1-\nu) & \nu & 0 & 0 & 0 \\ \nu & \nu & (1-\nu) & 0 & 0 & 0 \\ 0 & 0 & 0 & \frac{1}{2}(1-2\nu) & 0 & 0 \\ 0 & 0 & 0 & 0 & \frac{1}{2}(1-2\nu) & 0 \\ 0 & 0 & 0 & 0 & 0 & \frac{1}{2}(1-2\nu) \end{bmatrix} \tag{2.10}$$

The variables E and ν represent the material elastic modulus and Poisson's ratio, respectively. Thus, the total strain energy expression given by Equation (2.9) becomes

$$U = \frac{1}{2}\int_V \{\varepsilon\}^T [D]\{\varepsilon\}\, dV \tag{2.11}$$

Also, the kinetic energy is given by

$$T = \frac{1}{2}\int_V \rho\left(\dot{u}^2 + \dot{v}^2 + \dot{w}^2\right) dV \tag{2.12}$$

where $\dot{u}, \dot{v}, \dot{w}$ are the velocities in the x, y, z directions respectively and ρ is the material density. Also, if p_x, p_y, and p_z are components of applied surface forces per unit area on surface S, the virtual work is given by[16]

$$\delta W = \int_S \left(p_x\delta u + p_y\delta v + p_z\delta w\right) dS \tag{2.13}$$

Now, the energy expressions and work expression for a three-dimensional solid (or the hexahedral element) can be substituted into the expression of Hamilton's Principle given by Equation (2.5), and the equations of motion along with the boundary terms can be found for the element. This derivation is omitted here since the details can be found in the literature.[15, 16] After the integration and algebraic calculations, the equations of motion for

the three-dimensional element are found in partial-differential form, along with any natural and geometric boundary conditions. The response of simple structures may be obtained by solving the differential equations of motion together with the boundary conditions. In various cases, such as the present, the structure becomes too complex consisting of many different types of elements or irregular geometries, thus the equations of motion become too difficult to be solved analytically. This difficulty is overcome by finding approximate solutions that satisfy Hamilton's principle. One such approximation is the FE displacement method. The basic premise of the FE method is to discretize a structure into a set of nodes that make up a finite number of elements, associate with each node a given number of degrees-of-freedom (DOF), and construct a set of shape functions to interpolate the geometry and the displacement of the nodes. This will be discussed in detail in the subsequent section.

2.3.2 Finite Element Formulation

The discretization of the structure was discussed in Section 2.2.2, thus the focus here will be on the element shape functions and the derivation of the equations of motion in matrix form from Hamilton's principle. For any type of element, a conventional way to find appropriate shape functions is to assume a polynomial function with the appropriate number of terms, and evaluate it and its derivatives at the element nodes to obtain the polynomial coefficients.[16] The general polynomial function with respect to nodal displacements is given by:

$$u^n(x,t) = \sum_{j=1}^{n} N_j(x) u_j^n(t) \tag{2.14}$$

where the u_j^n terms are unknown functions of time (i.e., nodal displacements) and the N_j terms are prescribed linearly independent functions of space (i.e., shape functions). The displacement is approximated so that it satisfies both Hamilton's principle and the system boundary conditions (BC's).

The choice of the shape functions is dependent on the type of element chosen in the structural discretization. Shape functions are typically found for an element, and the

equations of motion derived for that particular element. The equations of motion for each element are then assembled into the global set of equations, and the system can be solved for unknown functions, such as displacement. Derivation will now focus on the elements used to model the presented SRM. First, consider the 20-node higher-order three-dimensional hexahedral element used in the present study, as shown in Figure 2-9. The node numbering used in the present study is also shown, which is the convention for this element type.

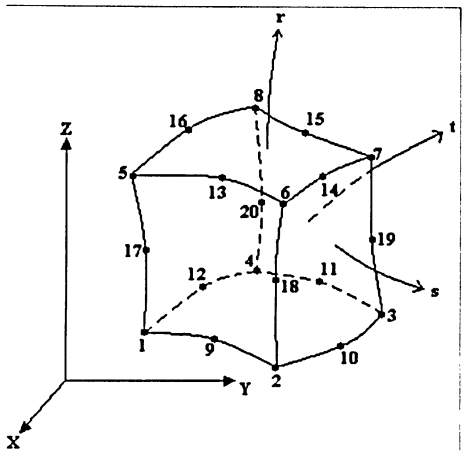

Figure 2-9 20-node hexahedral element

The global Cartesian coordinates are shown as (x, y, z), whereas the local element coordinates are shown as (s, t, r). This specific element is known as an isoparametric element since the local coordinates are mapped to the global coordinate system with the same shape functions that were used in the displacement approximation given by Equation (2.14). This isoparametric element formulation is useful in many applications because these elements adapt well to curved boundaries, which is seen in the SRM structure of the present study. The corresponding shape functions for this element are given by:[16]

$$N_j = \frac{1}{8}(1+s_j s)(1+t_j t)(1+r_j r)(s_j s + t_j t + r_j r - 2), \textit{for local nodes 1 to 8} \quad (2.15a)$$

$$N_j = \frac{1}{4}(1-s^2)(1+t_j t)(1+r_j r), \textit{for local nodes 9, 11, 13, 15} \quad (2.15b)$$

$$N_j = \frac{1}{4}(1+s_j s)(1-t^2)(1+r_j r), \textit{for local nodes 10, 12 14, 16} \quad (2.15c)$$

$$N_j = \frac{1}{4}(1+s_j s)(1+t_j t)(1-r^2), \textit{for local nodes 17 to 20} \quad (2.15d)$$

Here, the s_j, t_j, and r_j terms correspond to the nodal coordinate values based on the local coordinate system at the j^{th} node. For example, based on the local coordinate system shown above with three nodes on each edge of the element, the corresponding local coordinate values would be -1, 0 or +1.

Now, mapping of the local coordinates (and consequently the local displacements since the formulation is isoparametric) to the global system is achieved with the use of the shape functions defined. The relevant polynomial expressions for the coordinates in terms of x, y, z are given by:[16]

$$x = \sum_{j=1}^{20} N_j x_j \ , \ y = \sum_{j=1}^{20} N_j y_j \ , \ z = \sum_{j=1}^{20} N_j z_j \tag{2.16}$$

These expressions are analogous to the expression defining the displacement approximation defined by Equation (2.14), with the use of the same shape functions. Note the displacements in each Cartesian direction (u, v, w) have similar polynomial approximations, with the same shape functions. In matrix notation, the displacement expressions can be combined to give:

$$\{\overline{u}\} = \begin{Bmatrix} u \\ v \\ w \end{Bmatrix} = [N]\{u^e\} = \begin{bmatrix} N_1 & 0 & 0 & \cdots & N_{20} & 0 & 0 \\ 0 & N_1 & 0 & \cdots & 0 & N_{20} & 0 \\ 0 & 0 & N_1 & \cdots & 0 & 0 & N_{20} \end{bmatrix} \begin{Bmatrix} u_1 \\ v_1 \\ w_1 \\ \vdots \\ u_{20} \\ v_{20} \\ w_{20} \end{Bmatrix} \tag{2.17}$$

where $[N]$ is the shape function matrix and $\{u^e\}$ is the element displacement vector. This element with its defined shape functions given by Equation (2.15) assumes a quadratic displacement distribution along any edge of the element. Consequently, the mapped local coordinates also assume a quadratic profile along each element edge. This enables fewer elements to be used in a FE mesh in order to represent a curved boundary.

Now, consider a reduced order hexahedral element with 8 nodes shown in Figure 2-10. This element is similar to the 20-node hexahedral element, except that the mid-side nodes are omitted. Note the same local coordinate system is used, with a similar numbering scheme to the corner nodes of the 20-node hexahedral element.

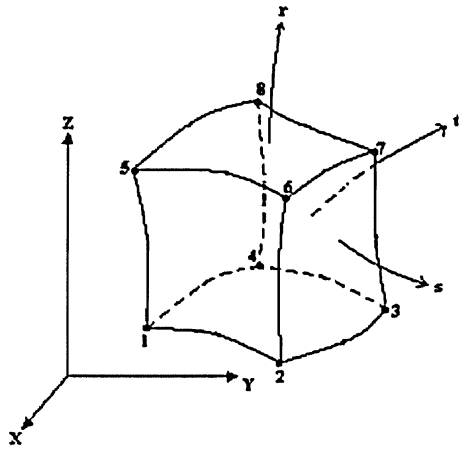

Figure 2-10 8-node hexahedral element

The corresponding shape functions for all 8 element nodes are given by:[16]

$$N_j = \frac{1}{8}(1+s_j s)(1+t_j t)(1+r_j r) \tag{2.18}$$

Here the s_j, t_j, and r_j terms correspond to local coordinate values of -1 and +1. Mapping of local coordinates and local displacements to the global system are found similar to the 20-node element. The polynomial expressions for the coordinates in terms of x, y, z is given by:[16]

$$x = \sum_{j=1}^{8} N_j x_j \ , \ y = \sum_{j=1}^{8} N_j y_j \ , \ z = \sum_{j=1}^{8} N_j z_j \tag{2.19}$$

Note the displacements in each Cartesian direction (u, v, w) also have similar polynomial approximations, with the same shape functions defined by Equation (2.18). The matrix displacement expressions can be written as:

$$\{\overline{u}\} = \begin{Bmatrix} u \\ v \\ w \end{Bmatrix} = [N]\{u^e\} = \begin{bmatrix} N_1 & 0 & 0 & \cdots & N_8 & 0 & 0 \\ 0 & N_1 & 0 & \cdots & 0 & N_8 & 0 \\ 0 & 0 & N_1 & \cdots & 0 & 0 & N_8 \end{bmatrix} \begin{Bmatrix} u_1 \\ v_1 \\ w_1 \\ \vdots \\ u_8 \\ v_8 \\ w_8 \end{Bmatrix} \tag{2.20}$$

This element assumes a linear displacement and linear coordinate profile along each element edge. Thus, in order to correctly represent a curved boundary, more elements must be used in the mesh relative to the 20-node hexahedral mesh. The advantages and disadvantages of

each presented element for this particular study will be shown through the preliminary FE results presented and discussed in Section 2.6.

Now that the shape functions for both element types are known, the displacement polynomial expression defined by Equation (2.14) can be substituted back into the energy expressions for the particular element (i.e. T_e, U_e, δW_e) given by Equations (2.11) – (2.13), and the equations of motion can be determined via Hamilton's principle. The energy expressions re-defined in matrix form for a particular element are given by:

$$T_e = \frac{1}{2}\{\dot{u}^e\}^T [M^e]\{\dot{u}^e\} \tag{2.21a}$$

$$D_e = \frac{1}{2}\{\dot{u}^e\}^T [C^e]\{\dot{u}^e\} \tag{2.21b}$$

$$U_e = \frac{1}{2}\{u^e\}^T [K^e]\{u^e\} \tag{2.21c}$$

where D_e is the element dissipation function and $[C^e]$ the element damping matrix. Based on the presented shape function matrices, the element mass $[M^e]$ and stiffness $[K^e]$ matrices are calculated to be:[16]

$$[M^e] = \int_V [N]^T \rho [N] dV \tag{2.22}$$

$$[K^e] = \int_V [B]^T [D][B] dV \tag{2.23}$$

where ρ is the material density and $[D]$ is the material matrix defined by Equation (2.10). The matrix $[B]$ is found via the strain-displacement relationship, which is defined by the following expression:[16]

$$\{\varepsilon\} = \begin{Bmatrix} \frac{\partial u}{\partial x} \\ \frac{\partial v}{\partial y} \\ \frac{\partial w}{\partial z} \\ \frac{\partial u}{\partial y} + \frac{\partial v}{\partial x} \\ \frac{\partial u}{\partial z} + \frac{\partial w}{\partial x} \\ \frac{\partial v}{\partial z} + \frac{\partial w}{\partial y} \end{Bmatrix} = [L]\{\bar{u}\} = \begin{bmatrix} \frac{\partial}{\partial x} & 0 & 0 \\ 0 & \frac{\partial}{\partial y} & 0 \\ 0 & 0 & \frac{\partial}{\partial z} \\ \frac{\partial}{\partial y} & \frac{\partial}{\partial x} & 0 \\ \frac{\partial}{\partial z} & 0 & \frac{\partial}{\partial x} \\ 0 & \frac{\partial}{\partial z} & \frac{\partial}{\partial y} \end{bmatrix} [N]\{u^e\} = [B]\{u^e\} \tag{2.24}$$

Thus, when multiplying the operator matrix [L] with the shape function matrix [N], [B] can be calculated to be:

$$[B]=[B_1 \quad \cdots \quad B_{20}] \tag{2.25}$$

The sub-matrices included in Equation (2.25) are defined as:

$$B_i=\begin{bmatrix} \frac{\partial N_i}{\partial x} & 0 & 0 \\ 0 & \frac{\partial N_i}{\partial y} & 0 \\ 0 & 0 & \frac{\partial N_i}{\partial z} \\ \frac{\partial N_i}{\partial y} & \frac{\partial N_i}{\partial x} & 0 \\ \frac{\partial N_i}{\partial z} & 0 & \frac{\partial N_i}{\partial x} \\ 0 & \frac{\partial N_i}{\partial z} & \frac{\partial N_i}{\partial y} \end{bmatrix} \tag{2.26}$$

Note that for an 8-node hexahedral element, the B_i terms in the [B] matrix only range from 1 to 8.

Given that the shape functions are expressed in terms of local coordinates, their derivatives can be expressed in terms of local coordinates also. This is not done directly, but by using the Jacobian, which is a scale factor that describes the physical dimensions (x, y, z) associated with the reference local dimensions (s, t, r). In a three-dimensional element, the Jacobian is in the form of a three-by-three matrix and is defined by the expression:[16]

$$[J]=\begin{bmatrix} \frac{\partial x}{\partial s} & \frac{\partial y}{\partial s} & \frac{\partial z}{\partial s} \\ \frac{\partial x}{\partial t} & \frac{\partial y}{\partial t} & \frac{\partial z}{\partial t} \\ \frac{\partial x}{\partial r} & \frac{\partial y}{\partial r} & \frac{\partial z}{\partial r} \end{bmatrix} \tag{2.27}$$

where the x, y, z terms are given by either Equation (2.16) or Equation (2.19). The elemental volume term in the mass and stiffness matrix integral expressions is defined by $dV=\det[J]dsdtdr$. The shape function derivative terms in the [B] matrix are found using the Jacobian via the expression:

$$\begin{bmatrix} \partial N_1/\partial x & \cdots & \partial N_{20}/\partial x \\ \partial N_1/\partial y & \cdots & \partial N_{20}/\partial y \\ \partial N_1/\partial z & \cdots & \partial N_{20}/\partial z \end{bmatrix}=[J]^{-1}\begin{bmatrix} \partial N_1/\partial s & \cdots & \partial N_{20}/\partial s \\ \partial N_1/\partial t & \cdots & \partial N_{20}/\partial t \\ \partial N_1/\partial r & \cdots & \partial N_{20}/\partial r \end{bmatrix}. \tag{2.28}$$

Again note that for an 8-node hexahedral element, the matrix terms in Equation (2.28) only range from 1 to 8. Thus the element mass and stiffness matrices given in Equations (2.22) and (2.23) are represented by the following expressions.

$$[M^e] = \int_{-1}^{+1}\int_{-1}^{+1}\int_{-1}^{+1} \rho [N]^T [N] \det[J] \, ds dt dr \tag{2.29}$$

$$[K^e] = \int_{-1}^{+1}\int_{-1}^{+1}\int_{-1}^{+1} [B]^T [D][B] \det[J] \, ds dt dr \tag{2.30}$$

The integration limits here are -1 and +1, which are the ends of the respective elements based on the local coordinate system values.

The mass matrix defined by Equations (2.22) and (2.29) is denoted as being consistent, since the same shape functions used to define the element stiffness matrix are used. A more simplified formulation is termed as a lumped mass matrix. This type of matrix is obtained by placing particle masses at all the nodes in an element, such that the sum of these particle masses is equal to the total mass of the element.[15] A lumped mass matrix is diagonal, while a consistent mass matrix is not. There are obvious merits with both types of mass matrices, which will be compared in Section 2.6. One method commonly used to formulate a lumped mass matrix is known as HRZ lumping.[15] The idea is to formulate the consistent mass matrix for an arbitrary element, and use only the scaled diagonal elements of that matrix to form the entries in the lumped mass matrix. The element mass, *m*, is given as the sum of all the entries in the element consistent mass matrix. The constant *d* is defined as the sum of the diagonal entries in the element consistent mass matrix. Thus, to form the diagonal entries in the lumped mass matrix, the diagonal entries of the consistent mass matrix are multiplied by the factor *m/d*. The mathematical representation on a matrix entry level is shown by the following equation.

$$[M^e{}_{ii}]_{lumped} = \frac{m}{d}[M^e{}_{ii}]_{consistent} \tag{2.31}$$

As mentioned, the lumped mass matrix is diagonal, where the *ii* terms in Equation (2.31) are the diagonal entries of both the consistent and lumped mass matrices. This formulation is valid for all elements used in this study. From this point on the element mass matrix, whether it is consistent or lumped, will be denoted as $[M^e]$.

2.3.3 Numerical Integration and Constraints

The numerical integration schemes used in this study are based on Gaussian quadrature and are typically used for finite element analysis. Full details of the integration schemes can be found in the literature;[15] thus, only information pertaining to this study will be presented. The main premise behind Gaussian quadrature is to take the integrand of an integral expression and approximate its integration using various sampling points with respective weight factors. Since this study requires the integration of the entries in the element mass and stiffness matrices of three-dimensional elements, two and three dimensional quadrature over the interval (-1, +1) is required. Consider the general integral expression given by Equation (2.32), where Φ is the arbitrary integration variable.

$$I = \int_{-1}^{+1} f(\Phi) d\Phi \tag{2.32}$$

The integration scheme approximates this integral with the expression:

$$I = W_1 f(\Phi_1) + W_2 f(\Phi_2) + \cdots + W_n f(\Phi_n) \tag{2.33}$$

Here the weight factors are denoted by W_n and n is the order of the integration. The Φ_n terms are the sampling points of the integration, and their number is dictated by the order of the integration. Below, Table 2-3 lists the respective sampling points and weight values for an integration scheme over the interval (-1, +1), for various orders.

Order n	Location of Sampling Points, Φ_n	Weight Factor, W_n
1	0.	2.
2	$\pm 1/\sqrt{3}$	1.
3	$\pm\sqrt{0.6}$	5/9
	0.	8/9
4	$\pm\left[\frac{3+2\sqrt{1.2}}{7}\right]^{1/2}$	$\frac{1}{2}-\frac{1}{6\sqrt{1.2}}$
	$\pm\left[\frac{3-2\sqrt{1.2}}{7}\right]^{1/2}$	$\frac{1}{2}+\frac{1}{6\sqrt{1.2}}$

Table 2-3 Gaussian quadrature sampling points and weight factors[15]

Consequently, in two and three dimensions, the integration scheme is an extension of Equation (2.33). Consider the integration of the element force vector representing surface traction on the element face, on the local *s-t* plane (see Figure 2-9 or Figure 2-10). Assuming the use of a second order integration scheme (i.e., n=2), the sampling points are located on the element face as shown in Figure 2-11 (a). The expression representing the integral and its approximation is given by:

$$I = \int_{-1}^{+1}\int_{-1}^{+1} f(s,t)dsdt \approx \sum_i \sum_j W_i W_j f(s_i,t_j) \tag{2.34}$$

Similarly, consider the second order integration of the element mass and stiffness matrix expressions given by Equations (2.29) and (2.30). The integration sampling points are shown in Figure 2-11 (b), with the integral expression in three-dimensions given by:

$$I = \int_{-1}^{+1}\int_{-1}^{+1}\int_{-1}^{+1} f(s,t,r)dsdtdr \approx \sum_i \sum_j \sum_k W_i W_j W_k f(s_i,t_j,r_k) \tag{2.35}$$

Note that the integration in Equations (2.29) and (2.30) is of the individual entries in the element mass and stiffness matrices, as will be shown for the element force vector.

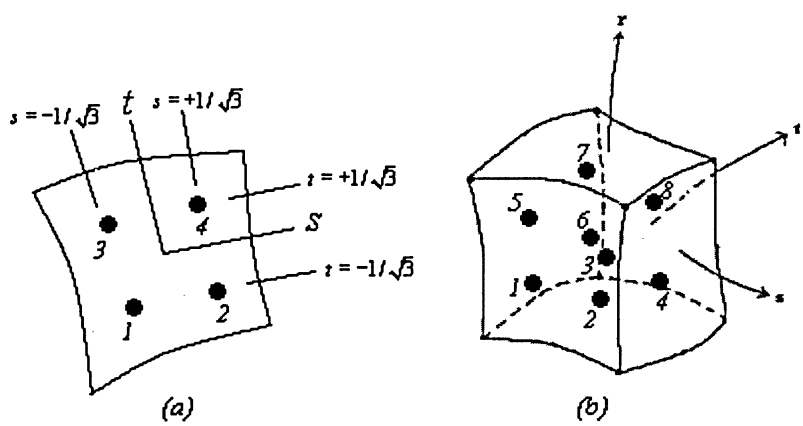

Figure 2-11 Sampling points, second order: (a) two-dimensional, (b) three-dimensional

For the 20-node hexahedral element, a third order integration scheme for the mass and stiffness matrices and the force vector is required for accuracy of integration. This means that 27 points (i.e., 3x3x3) are required to accurately solve for the element mass and stiffness matrices, and 9 points (i.e., 3x3) are required for the element force vector. For the 8-node hexahedral element, a second order scheme will suffice due to the reduced order of

the shape functions, yielding 8 sampling points in total for the element mass and stiffness matrices, and 4 sampling points for the element force vector.[15, 16] The number of integration points for a particular element affects the accuracy of both the mass and stiffness matrices, as well as the force vector. If the number of integration points is reduced below the above specified amounts, the accuracy of the integration will reduce. This, however, may not necessarily reduce the accuracy of the finite element solution, where it is sometimes convenient to use fewer sampling points in order to 'soften' an elements response.[15] This reduction in sampling points can make an element respond less rigid versus using more sampling points. In the case of the present study where the propellant material is nearly incompressible, the number of integration points can severely affect the response of the structure. From this point on, unless otherwise stated, the number of integration points used in the FE analysis is that which has been presented above, which is required for integration accuracy for each element.

Using the energy expressions along with the shape functions, the defined mass and stiffness matrices, and carrying out the variation leads to the element equations of motion, which are known as Lagrange's equation. It is, however, more convenient to assemble the element matrices and load vectors into the global system equations of motion based on the nodal connectivity of each element. This is done element by element, where the global mass and stiffness matrices are defined as:

$$[M^{'}] = \sum_{i=1}^{\#\,elements} [M^{e}]_i \quad and \quad [K^{'}] = \sum_{i=1}^{\#\,elements} [K^{e}]_i \tag{2.36}$$

The global force vector $\{F\}$ is assembled in a similar manner. This ultimately leads to Lagrange's equation of motion for the entire global system, which is given by the following expression:[16]

$$[M^{'}]\{\ddot{u}\} + [C^{'}]\{\dot{u}\} + [K^{'}]\{u\} = \{F^{'}\} \tag{2.37}$$

The single and double dots over the global displacement vector $\{u\}$ indicate derivatives with respect to time of velocity and acceleration, respectively. Lagrange's equations of motion are for the domain of a structure, and are a product of the calculation of Hamilton's principle defined by Equation (2.5).

Now that the global system matrices and vectors are assembled, the rigid body constraints can be applied to the system before the equations of motion are solved. This ensures there is no structural rigid body motion and that the global matrices are not singular, which can cause numerical instabilities during FE solution.[15] Operations to the global mass, stiffness, and damping ([C']) matrices for rigid body constraints are identical. In the case of this study, the constraint nodal transients (i.e., displacements, velocities and accelerations) are set to zero based on the global Cartesian coordinate system. Also because of the skewed plane of symmetry shown in Figure 2-5, relative to the Cartesian coordinate system, skewed boundary constraints must be applied to the nodes on the symmetry plane. This requires the formulation of a transformation matrix used to convert the nodal coordinates on the skewed plane of symmetry to the local coordinate system, which is offset by angle θ_{cr} with respect to the x-y plane. The three-dimensional transformation matrix used in this study is defined by[19]

$$[t]=\begin{bmatrix}\cos\theta_{cr} & -\sin\theta_{cr} & 0\\ \sin\theta_{cr} & \cos\theta_{cr} & 0\\ 0 & 0 & 1\end{bmatrix} \tag{2.38}$$

Since the plane of symmetry has no offset to the axial axis of the motor, the transformation matrix only transforms the global x and y coordinates. This is also illustrated below in Figure 2-12, where only a two-dimensional section of the motor is shown.

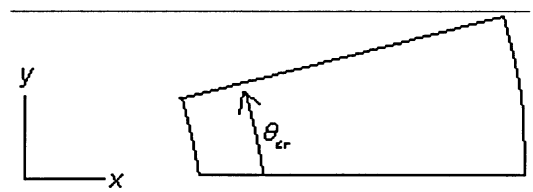

Figure 2-12 Critical angle used for transformation of skewed boundaries

Now, the global matrices and force vector can be transformed to include the skewed constraints. Thus the constrained global equations of motion are given by:

$$[M]\{\ddot{u}\}+[C]\{\dot{u}\}+[K]\{u\}=\{F\} \tag{2.39}$$

where the constrained system mass matrix, stiffness matrix, damping matrix and force vector are given by $[M]=[T]^T[M']$[T], $[K]=[T]^T[K']$[T], $[C]=[T]^T[C']$[T], and $\{F\}=[T]^T\{F'\}$, respectively. The matrix [T] is composed of the transformation matrix given by Equation

(2.38), and can be found in the literature.[19] Equation (2.39) can now be solved using various techniques depending on the type of structural analysis, but first the details of the damping matrix [C] and force vector $\{F\}$ will be presented.

2.4 Force Vector and Damping Considerations

2.4.1 External Force Terms

The focus now will be on the calculation of the element force vector and the damping matrix, respectively. The force vector consists of the combination of all the applied loading on the structure that is relevant to this study. In this particular study, the force vector contributions come from two main types of loading as mentioned previously: surface traction imparted by the applied chamber pressure, and body loads caused by motor spinning and longitudinal accelerations.

Based on the principle of virtual work, traction loads can be applied to the nodes of an element on the structure by integrating the load distribution on any surface of the element. The general governing equation for surface traction is given by:[16]

$$\{F_s\}^e = \int_S [N]^T \{p\} ds \tag{2.40}$$

Here S denotes the element surface that is subjected to the load, and $\{p\}$ is the pressure vector with components in the three Cartesian coordinates. This applied loading is illustrated in Figure 2-13, where the pressure is applied normal to the element surface.

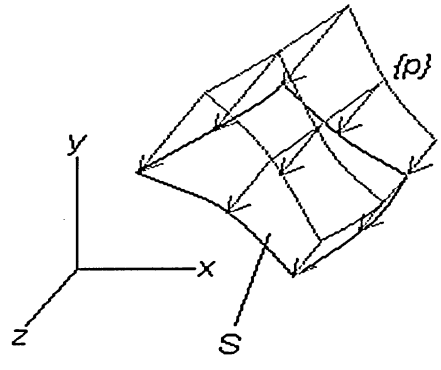

Figure 2-13 Surface pressure on element face

Generally, and certainly in the present study, the pressure vector components are given in the local element coordinate system, not the global Cartesian coordinate system. The formulation would be far less complicated if the pressure vector in Equation (2.40) is converted to local coordinates. Since the elements used in this study are isoparametric, a similar Jacobian defined by Equation (2.27) can be used in two-dimensions to formulate the element force vectors.

If an arbitrary face for either the 8-node or 20-node hexahedral elements is subjected to pressure, the Jacobian can be determined based on the specific element face. For example, consider that the pressure being applied in Figure 2-13 is on the ξ-ζ face of a hexahedral element. The ξ-ζ face can be any two local coordinate directions (i.e., *s*-*t*), where the remaining direction is denoted by η (i.e., *r*), and is the direction normal to the face the load is applied on. The elemental surface term in Equation (2.40) is given by the cross product of the local direction vectors, namely:[16]

$$dS = \left| d\vec{\xi} \times d\vec{\zeta} \right|_{\eta=\pm 1} = J d\xi d\zeta \tag{2.41}$$

The force vector equation now becomes:

$$\{F_S\}^e = \int_{-1}^{+1}\int_{-1}^{+1} [N]^T \{p\} J d\xi d\zeta \tag{2.42}$$

Note the integration limits are from -1 to +1, the element span, in two directions on the face of the element. There are obvious complications with this formulation, thus a more appropriate form is necessary in order to be applicable to the SRM structure. Meguid[20] has introduced a formulation for the equivalent nodal force vector with respect to a discretized pressure, $p = \{p_1 \quad p_2 \quad \cdots \quad p_8\}$, applied to any face consisting of 8 nodes of a 20-node hexahedral element. A similar formulation would be applicable to a face on an 8-node hexahedral element, consisting of 4 nodes. The components of the discretized pressure are the pressure values at the nodes on the applied surface. Thus the pressure over any element face can vary, and the formulation will still be valid. This seems to be convenient for the SRM application, seeing as the output of the fluid algorithm is an axial pressure variation.

Consider the +*t* face on the *s*-*r* plane of a 20-node hexahedral element with applied pressure discretized on each node as mentioned above. The area differential given above is

now given by Equation (2.43), with $J = \sqrt{J_x^2 + J_y^2 + J_z^2}$. This area differential is specific to the face that is subjected to the pressure load.

$$dS = \begin{vmatrix} \hat{i} & \hat{j} & \hat{k} \\ \frac{\partial x}{\partial s} & \frac{\partial y}{\partial s} & \frac{\partial z}{\partial s} \\ \frac{\partial x}{\partial r} & \frac{\partial y}{\partial r} & \frac{\partial z}{\partial r} \end{vmatrix} dsdr = \left(J_x \hat{i} + J_y \hat{j} + J_z \hat{k}\right) dsdr \tag{2.43}$$

The equivalent loading vector terms in the x, y, z global Cartesian directions at each element node are given by:

$$F_{x_i} = -\sum_{j=1}^{20} Q_{x_{i,j}} p_j \tag{2.44a}$$

$$F_{y_i} = -\sum_{j=1}^{20} Q_{y_{i,j}} p_j \tag{2.44b}$$

$$F_{z_i} = -\sum_{j=1}^{20} Q_{z_{i,j}} p_j \tag{2.44c}$$

The p_j terms are the discretized pressure values (zero if node is not on applied face), and the $Q_{ri,j}$ terms are defined by Equation (2.45), with the r subscript equal to x, y, or z.

$$Q_{r_{i,j}} = \iint N_i N_j J_r dsdr \tag{2.45}$$

The equivalent element loading vector for surface traction is finally given by:

$$\{F_S\}^e = \left\{F_{x_1} \quad F_{y_1} \quad F_{z_1} \quad \cdots \quad F_{x_{20}} \quad F_{y_{20}} \quad F_{z_{20}}\right\}^T \tag{2.46}$$

Note, the $Q_{ri,j}$ terms can be evaluated using the presented Gaussian integration schemes in two-dimensions. For the purposes of this study, a 3rd order scheme is found to be sufficient. Also note that for an 8-node hexahedral element, the summation of Equations (2.44a) – (2.44c) and the force vector defined by Equation (2.46) are only for the 8 nodes, not the 20 nodes.

Based on the principle of virtual work, body loads acting on a structure can be applied to the nodes of an element by integrating the load distribution over the volume of the element. Thus, the equivalent element body load force vector is given by:[16]

$$\{F_b\}^e = \int_V [N]^T \{b\} dV \tag{2.47}$$

The $\{b\}$ vector terms are the components of the body load per unit volume in the global Cartesian directions. For a motor spinning at a constant angular speed ω about its axis, the centripetal acceleration is given by $\omega^2 r$, where r is the radial distance from the centerline of the motor. The body load per unit volume is then given by $\rho\omega^2 r$, which can then be used to determine the global coordinate system components in the vector $\{b\}$. Similarly, for axial acceleration acting on the motor, the body load per unit volume is given by ρg_{ax}, where g_{ax} is the motor axial acceleration. In the case of axial acceleration, the body load per unit volume would be applied in one global direction, while the contribution in the other two directions would be zero.

If the $\{b\}$ vector components at each node are represented in discrete form as $\{b\} = \{b_{x_1} \quad b_{y_1} \quad b_{z_1} \quad \cdots \quad b_{x_{20}} \quad b_{y_{20}} \quad b_{z_{20}}\}^T$, the equivalent load vector components in terms of global Cartesian coordinates are given by:

$$F_{x_i} = \sum_{j=1}^{20} Q_{i,j} b_{x_j} \tag{2.48a}$$

$$F_{y_i} = \sum_{j=1}^{20} Q_{i,j} b_{y_j} \tag{2.48b}$$

$$F_{z_i} = \sum_{j=1}^{20} Q_{i,j} b_{z_j} \tag{2.48c}$$

The Q_{ij} terms are defined by:

$$Q_{i,j} = \iiint N_i N_j dV = \int_{-1}^{+1}\int_{-1}^{+1}\int_{-1}^{+1} N_i N_j \det[J] ds dt dr \tag{2.49}$$

Since the body load acts over the entire volume of an element, the formulation of the Jacobian is similar to that used for element mass and stiffness matrices in Equations (2.29) and (2.30). Also, 3rd order three-dimensional Gaussian integration is acceptable for the elements employed in this study. Finally, the equivalent element loading vector for body loads is given by:

$$\{F_b\}^e = \{F_{x_1} \quad F_{y_1} \quad F_{z_1} \quad \cdots \quad F_{x_{20}} \quad F_{y_{20}} \quad F_{z_{20}}\}^T \tag{2.50}$$

Note that the shape functions denoted by N_i and N_j in Equations (2.45) and (2.49) are for nodes i and j, respectively. Also for an 8-node hexahedral element, the summations in

Equations (2.48a) – (2.48c) and the equivalent loading vector terms in Equation (2.50) are only for 8 nodes, not 20 nodes.

Now, the total element force vector can be defined by summing both the surface traction force vector and body load force vector as:

$$\{F\}^e = \{F_s\}^e + \{F_b\}^e \tag{2.51}$$

The global external force vector $\{F'\}$ is then found by summing the contributions of each element force vector, based on the connectivity of the elements in the mesh. This is analogous to the formulation of the global mass and stiffness matrices in Equation (2.36). The constraint operations mentioned previously are then applied to the global external force vector, details of which can be found in the literature.[19]

2.4.2 FE Damping Matrix

The dissipation or damping function for a particular structure is difficult to derive since damping is an inherent property of a vibrating structure that is not easily modeled. Damping forces depend on the structure itself and also on the surrounding medium; thus, two main types of damping exist. Structural damping depends on the internal friction and hysteresis within the material, while viscous damping occurs when a structure is moving in air or any fluid.[15] Formulation of damping models can become quite complicated mathematically, thus simplified models are developed, and have been found to be adequate for most analyses.[16] In order to model the actual physical structural damping in any system, a phenomenological method would be necessary. These models are generally complicated and not necessarily accurate because there is usually a lack of information about the materials. The material dissipative mechanisms such as hysteresis loss and structural joint friction must be modeled, which can lead to nonlinear analysis and even greater complications. Viscous damping models have the easiest formulation; thus, other damping models can be replaced by equivalent viscous damping models. One common method for modeling the equivalent viscous damping of a system is a spectral damping method, where the viscous damping is introduced by means of a specified fraction of critical damping, or a

damping ratio, ζ.[15] Here, experimental observations of the response of the vibrating structural system are used to assign a damping ratio as a function of natural frequency. More commonly, a single damping ratio is used for the entire frequency range of a structure in order to keep the model as simplified as possible. Typically, the damping ratio depends on the materials in the structure and the stress levels exhibited by the materials.

One common spectral damping method used in FE analysis is proportional or Rayleigh damping. The premise with this method is to form the system damping matrix, [*C*] as a linear combination of both the system mass and stiffness matrices, as given by:

$$[C]=\alpha[K]+\beta[M] \tag{2.52}$$

The α and β terms are called the stiffness and mass proportional damping constants, respectively. The relationship between the damping ratio at a frequency ω and the stiffness and mass proportional damping constants is given by:

$$\zeta=\frac{1}{2}\left(\alpha\omega+\frac{\beta}{\omega}\right) \tag{2.53}$$

The constants α and β are found by choosing two damping ratios (ζ_1 and ζ_2) corresponding to two natural frequencies (ω_1 and ω_2). The two equations to be solved simultaneously are:

$$\alpha=2\frac{(\omega_2\gamma_2-\omega_1\gamma_1)}{(\omega_2^{\,2}-\omega_1^{\,2})} \tag{2.54a}$$

$$\beta=2\omega_1\omega_2\frac{(\omega_2\gamma_1-\omega_1\gamma_2)}{(\omega_2^{\,2}-\omega_1^{\,2})} \tag{2.54b}$$

The relationship given by Equation (2.52) can be shown graphically with a plot of damping ratio versus frequency, which is illustrated in Figure 2-14. The trends shown are common for the Rayleigh damping model used in this study. The mass proportional and stiffness proportional terms are included to show their individual influence on the overall damping. It becomes evident that as frequency increases the stiffness damping term is more dominant, but at lower frequencies the mass damping term is more dominant.

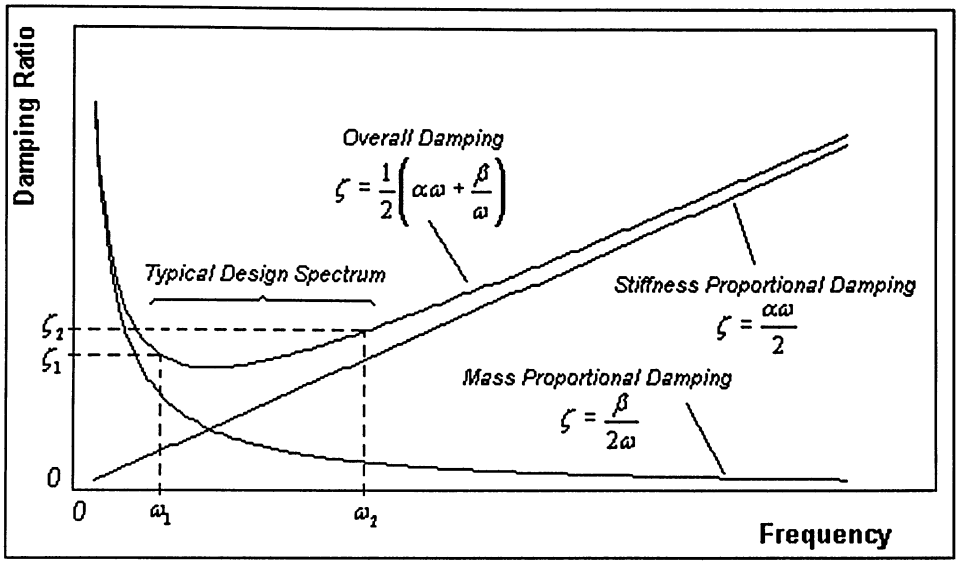

Figure 2-14 Plot of Rayleigh damping terms, with respect to ζ and ω

The next step is to determine the two damping ratios and their corresponding frequencies to be used in Equations (2.54a) and (2.54b). Typically, the two frequencies are chosen as the bounds of the design spectrum, as shown in Figure 2-14. Thus, ω_1 is taken as the first natural frequency of the structure and ω_2 is the maximum frequency of interest in the loading or response of the structure.[15] The maximum frequency is usually the dominant response frequency of the structure during transient loading. This typically occurs around the trough region for the overall damping plot in Figure 2-14, as shown. Now, the two damping ratios corresponding to the two frequencies can be chosen. For simplicity, the two damping ratios will be set equal, which is typically done with Rayleigh damping models.[15] Details of the choice in damping ratio for the structure can be found in Section 2.6, as are the details for the calculation of the system frequencies for various FE meshes employed in this study.

In the particular case when it is desirable to use either mass proportional or stiffness proportional damping, the damping matrix of Equation (2.52) is further simplified. Specifically, for mass proportional damping, the coefficients become $\alpha=0$ and $\beta=2\omega_2\zeta_2$, whereas for stiffness proportional damping the coefficients become $\beta=0$ and $\alpha=2\zeta_2/\omega_2$. In both cases, the frequency used is the dominant response frequency of the structure. When

using certain time integration methods, the use of mass proportional damping may be warranted for economical reasons.

2.5 Solution of FE Equations of Motion

The focus of this section will be the solution of the equations of motion for static, free vibration, and transient analyses, respectively. The system matrices and force vector have already been defined, thus the analysis is generally applied to any linear system. First, the static equations of motion and their solution will be discussed. Then, the solution procedure for a free vibration analysis will be detailed, as well as the application to the current study. Finally, a detailed analysis of all the transient time integration methods to be used will be presented hereafter.

2.5.1 Static Analysis

The equations of motion for a static solution consist of omitting the inertial and damping terms in Equation (2.39); thus, the velocity and acceleration vectors are omitted from the equations of motion. The remaining terms yield the equation for a static solution as:

$$[K]\{u\} = \{F\} \tag{2.55}$$

Note that the system displacement vector, $\{u\}$ is given by the expression:

$$\{u\} = \{u_1 \quad v_1 \quad w_1 \quad u_2 \quad v_2 \quad w_2 \quad \cdots \quad u_{n/3} \quad v_{n/3} \quad w_{n/3}\}^T \tag{2.56}$$

The elements used in this study all contain nodes with three degrees-of-freedom, thus the u, v, w components are the respective nodal displacements in the global x, y, z coordinate system. The total number of nodes is denoted by $n/3$, while the total degrees-of-freedom for this system is given by n. The system velocity and acceleration vectors denoted by $\{\dot{u}\}$ and $\{\ddot{u}\}$, respectively, are analogous to the system displacement vector. Equation (2.55) can now be solved for the system displacements using a relevant numerical scheme. Since the present study does not warrant a nonlinear analysis, the stiffness matrix is independent of the displacements and the solution to the equation is trivial.[15] A typical method used in FE

analysis to decompose the stiffness matrix is Cholesky factorization. This method assumes that the matrix is symmetric and positive definite, which is the case for all matrices used here. Also, since the system matrices have the appropriate physical constraints applied to them, there will not exist any rigid body motion and the solution will be feasible without any numerical problems. Details of the factorization are left out in order to be brief on the subject, but any details can be found in the literature.[16] The factorization produces a lower triangular matrix $[L]$ from the stiffness matrix, such that $[K] = [L][L]^T$, thus substituting into the equation of motion the formulation yields:

$$[L][L]^T \{u\} = \{F\} \tag{2.57}$$

In fact, a general equation of the form $[A]\{X\} = \{B\}$ can also be factored into the form $[L][L]^T\{X\} = \{B\}$, so long as $[A]$ is symmetric and positive definite. Equation (2.57) is now solved for $\{u\}$ by a simple forward and back substitution on a matrix-vector entry level. Static analysis is used in this study as an initial verification for the FE algorithm developed for this study.

2.5.2 Free Vibration

For a free vibration analysis, the equations of motion consist of omitting the damping term and the force vector from Equation (2.39). The resulting expression is given here as:

$$[M]\{\ddot{u}\} + [K]\{u\} = \{0\} \tag{2.58}$$

A trivial steady state solution to Equation (2.58) is setting $\{u\} = 0$; however, for the purposes of this study a state of free vibration is of interest, where the system displacement vector is non-zero. The vibratory response is sinusoidal over time relative to an arbitrary equilibrium position; thus, the displacement vector and associated acceleration vector are represented by:[21]

$$\{u\} = \{\bar{U}\} \sin \omega t \tag{2.59a}$$

$$\{\ddot{u}\} = -\omega^2 \{\bar{U}\} \sin \omega t \tag{2.59b}$$

Note that $\{\bar{U}\}$ is the maximum amplitude due to vibration, ω is the natural frequency, and t represents time. Substitution of Equations (2.59a) and (2.59b) into Equation (2.58) yields:

$$([K]-\omega^2[M])\{\bar{U}\}=\{0\} \tag{2.60}$$

This is a typical eigenproblem found in FE analysis,[15] where the ω^2 term is the eigenvalue of the system. To ensure the eigenvector (or mode shape) $\{\bar{U}\}$ is nontrivial, it is required that the following expression hold true, i.e., the determinant must be equal to zero.

$$\left|[K]-\omega^2[M]\right|=\{0\} \tag{2.61}$$

The eigenvalues of Equation (2.61) can be found by taking the determinant of the left-hand-side expression, and determining the characteristic polynomial expression in terms of the eigenvalues. If the system stiffness and mass matrices are of order n by n, then the polynomial expression will be of order n, and the solution will yield n eigenvalues from the roots of the polynomial (i.e., $\omega^2_1, \omega^2_2, \ldots, \omega^2_n$). This is however, analytically impractical for large systems with many degrees-of-freedom; thus, a numerical method can be used to extract the eigenvalues. Note that since the system mass and stiffness matrices are positive definite, all extracted eigenvalues will be zero or positive. Also, since the system is constrained and there is no rigid body motion, all eigenvalues will be distinct.

First, consider the transformation of Equation (2.61) to a typical standard form:[16]

$$\left|[A]-\omega^2[I]\right|=\{0\} \tag{2.62}$$

This is done by factoring the mass matrix, say using Cholesky factorization as described in Section 2.5.1, to $[M]=[L][L]^T$, then using two forward substitutions to yield the expression $[A]=[L]^{-1}[K][L]^{-T}$. Note that $[I]$ is an identity matrix of order n by n. In this form, the eigenvalues can be extracted by simply analyzing one matrix, $[A]$. Now that the standard form of the eigenproblem is defined, a suitable algorithm to extract the eigenvalues can be used. There are many types of methods that are commonly used to extract eigenvalues, many of which are commercially available algorithm packages. Some common methods used for large FE systems are transformation methods, which are efficient in extracting all the eigenvalues of a system. Although only the first few eigenvalues of all FE systems analyzed in this study are required, a transformation method is used because of the availability of a *computer algorithm to the author. In the interest of reducing algorithm development time,* this is deemed the best choice.

The main idea behind transformation methods is to reduce the matrix [A] to tri-diagonal form using a finite number of transformations. Then, the eigenvalues of the symmetric tri-diagonal matrix are easily extracted using another technique. The transformation method used in this study is Householder's Method, which uses a sequence of orthogonal transforms, each one of which produces a complete row and column of zeros apart from the elements within the tri-diagonal form. The previous rows and columns are unaffected, thus only (n-2) transformations are required. Details of the orthogonal transformations have been omitted for briefness, but can be found in the literature.[16] This leads to the matrix [A] converted to tri-diagonal form, which can be easily manipulated to extract the eigenvalues. The QL method is used to find the eigenvalues of the symmetric tri-diagonal matrix. Generally, the QL method can be used to find the eigenvalues of the matrix [A] without having it transformed to tri-diagonal form; however, this would take $2n^3$ operations. In tri-diagonal form only $2n$ operations are necessary, which proves to be a significant reduction in computation time. Details of this method are also located in the literature.[16]

At this point all the eigenvalues of the system are known, and sorted from lowest to highest. The system natural frequencies (ω_n) are then found by taking the root of the eigenvalues (i.e., $\sqrt{\omega_n^2}$). There will be a number of calculated eigenvalues equal to zero, which all correspond to the rigid body modes of the constrained system. This is inherent to any eigenvalue extraction method since the mass and stiffness matrices are both constrained from rigid body motion. The number of calculated eigenvalues equal to zero is the number of constrained degrees-of-freedom for the system, thus the first system eigenvalue (ω^2_1) is the first calculated non-zero eigenvalue.[16] This overall eigenproblem solution methodology typically requires a large amount of computation time, thus the number of degrees-of-freedom in the FE mesh must be reduced for efficiency. One way to reduce the number of degrees-of-freedom is to use a coarser mesh. This provides a quicker solution to the system eigenvalues for a given structure of the same geometry. Refining the mesh would require much more computation time and would provide more eigenvalues corresponding to higher modes, but would provide the same first few natural frequencies. Since only the first few natural frequencies are needed here, this is deemed the best option. It should also be noted

that the symmetric mesh, similar to that shown in Figure 2-3, is used to extract the eigenvalues of the system in order to further reduce the number of degrees-of-freedom. This may not necessarily be accurate since some vibration modes may be eliminated upon using symmetry. The proper method would be to analyze each section of the full geometry individually using periodic symmetry.[15] However, since symmetry is utilized during transient analysis, these eliminated modes are not needed, and the approximation will provide satisfactory results.

2.5.3 Transient Analysis

For a dynamic or time varying FE analysis, the equation of motion for the system to be solved is given by Equation (2.39). Since the response frequency of the structure is higher than one-third of the lowest natural frequency of the system, the damping and inertia terms significantly influence the time varied dynamic response of the structure, which is the reason they are maintained in the formulation. This equation must be solved for the system displacement, velocity, and acceleration vectors over time. The types of methods used to solve the equation of motion and the formulation of these methods depends greatly on the type of dynamic problem being analyzed. There are two main types of dynamic problems, mainly structural dynamics and wave propagation.[15] In wave propagation problems, the excitation and thus the response of the structure occurs at higher frequencies; thus, the inertia term is not a large factor. The analysis is done over a small time range, typically of the order of one passing of the wave across the structure. The present study will focus on structural dynamics, where the inertia term is significant as will be shown. One type of structural dynamic problem was presented in Section 2.5.2, that is free vibration and natural frequency calculation. The other type is time-history analysis, which requires tracking the response of the structure over time. Two popular methods for time-history analysis are modal and direct integration methods. Modal methods require the use of calculated eigenvalues, but since the eigenvalues are of little importance in this study, direct integration methods are used to solve Equation (2.39). Also, the direct integration method to be used depends on the type of loading (i.e., transient, harmonic, periodic, or random) on the structure. If a structure is

excited by a sudden non-periodic applied excitation, the response is transient since steady state oscillations are not produced. Generally, the term transient is applicable to a situation where the forces are applied for a short time interval, and any subsequent motion of the structure is free vibration, which eventually decays due to damping. However it is often applied to a continually changing situation for an indefinite period of time. In this case, the system force vector $\{F_{(t)}\}$ is arbitrarily varying with time, thus the analysis is deemed to be transient. This is the case in the present study, where the internal chamber pressure in the motor is varying with time, and the structural displacements and accelerations at discrete points in time are required for the simulation. All the direct time integration methods used in this transient analysis of this study will now be presented.

Direct time integration methods used for transient analysis can be categorized as either implicit or explicit methods. In either case, the time derivatives appearing in the equations of motion (i.e., $\{\dot{u}\}$ and $\{\ddot{u}\}$) are replaced by differences in the displacements $\{u\}$ at various instances in time, based on a finite difference approximations.[15] The idea is to write Equation (2.39) at a specific time instance, as shown by the two example expressions.

$$[M]\{\ddot{u}\}_j + [C]\{\dot{u}\}_j + [K]\{u\}_j = \{F\}_j \tag{2.63a}$$

$$[M]\{\ddot{u}\}_{j+1} + [C]\{\dot{u}\}_{j+1} + [K]\{u\}_{j+1} = \{F\}_{j+1} \tag{2.63b}$$

The subscripts j and j+1 denote times $j\Delta t$ and $(j+1)\Delta t$, respectively, while Δt is the size of the time increment (i.e., time step). In this study nonlinearities are not modeled, thus the system matrices are not functions of the transients ($\{u\}$, $\{\dot{u}\}$ and $\{\ddot{u}\}$) or of time. Two implicit and two explicit time integration methods will be presented and compared, with respect to accuracy and computational economy.

The first implicit method used in this study is the Houbolt method, which consists of expressing velocity and acceleration at time t_{j+1} in terms of displacements at time t_{j-2} to t_{j+1} using a backward difference scheme. The response curve and acceleration is approximated by a cubic polynomial in the interval (t_{j-2}, t_{j+1}). Formulation of velocity and acceleration yields the following two approximate expressions, in which the error is of the order $(\Delta t)^3$:[16]

$$\{\dot{u}\}_{j+1} = \frac{1}{6\Delta t}\left(-2\{u\}_{j-2} + 9\{u\}_{j-1} - 18\{u\}_j + 11\{u\}_{j+1}\right) \tag{2.64}$$

$$\{\ddot{u}\}_{j+1} = \frac{1}{(\Delta t)^2}\left(-\{u\}_{j-2} + 4\{u\}_{j-1} - 5\{u\}_j + 2\{u\}_{j+1}\right) \tag{2.65}$$

Substituting these expressions into the equation of motion evaluated at time t_{j+1}, Equation (2.63b), yields an expression for the response at time t_{j+1}, as shown by:

$$\frac{1}{(\Delta t)^2}[M]\left(-\{u\}_{j-2} + 4\{u\}_{j-1} - 5\{u\}_j + 2\{u\}_{j+1}\right) + \frac{1}{6\Delta t}[C]\left(-2\{u\}_{j-2} + 9\{u\}_{j-1} - 18\{u\}_j + 11\{u\}_{j+1}\right) + [K]\{u\}_{j+1} = \{F\}_{j+1} \tag{2.66}$$

Since the equation of motion is evaluated at time t_{j+1}, this method is known as implicit. Upon simplification of Equation (2.66), the expression for $\{u\}_{j+1}$ becomes:

$$\left(\frac{2}{(\Delta t)^2}[M] + \frac{11}{6\Delta t}[C] + [K]\right)\{u\}_{j+1} = \{F\}_{j+1} + \left(\frac{5}{(\Delta t)^2}[M] + \frac{3}{\Delta t}[C]\right)\{u\}_j - \left(\frac{4}{(\Delta t)^2}[M] + \frac{3}{2\Delta t}[C]\right)\{u\}_{j-1} + \left(\frac{1}{(\Delta t)^2}[M] + \frac{1}{3\Delta t}[C]\right)\{u\}_{j-2} \tag{2.67}$$

Thus, given $\{u\}_{j-2}, \{u\}_{j-1}, and \{u\}_j$ the displacement vector $\{u\}_{j+1}$ can be found using a numerical solver such as Cholesky factorization with forward and back substitution, as presented previously. The current velocity and acceleration vectors are found using Equations (2.64) and (2.65). A special starting procedure is necessary with this method. Given the displacements and velocities at time t=0 (i.e., $\{u\}_0$ and $\{\dot{u}\}_0$), the acceleration $\{\ddot{u}\}_0$ can be found using the equation of motion evaluated at time t=0. Also, the displacement vectors $\{u\}_1$ and $\{u\}_2$ must be known, and can be found using the following expressions.

$$\{u\}_1 = \{u\}_0 + \Delta t\{\dot{u}\}_0 + \frac{1}{2}(\Delta t)^2\{\ddot{u}\}_0 \tag{2.68a}$$

$$\{u\}_2 = \{u\}_1 + \Delta t\{\dot{u}\}_1 + \frac{1}{2}(\Delta t)^2\{\ddot{u}\}_1 \tag{2.68b}$$

The unknown velocity and acceleration vectors can be found via Equations (2.64) and (2.65). Once the starting procedure is complete, the time-history iterations are determined for indices j=2, 3, 4, . . . , etc. The Houbolt method does provide uncontrolled artificial damping,[15] which may be undesired for low frequency response. However for this study, response is higher in frequency and the artificial damping does not affect the response significantly. Furthermore, the method is unconditionally stable because it is implicit, thus the only restriction on the time step is that due to accuracy. For implicit methods, a typical value used

for the time step to ensure accuracy is given by $\Delta t = \frac{\pi}{50\omega_o}$, where ω_o is taken as the highest frequency of interest (i.e., ω_2 for Rayleigh damping).

The second implicit method to be used in this study is the Newmark method, which is a generalization of the linear acceleration method, which assumes acceleration varies linearly over the interval (t_j, t_{j+1}). The response at time t_{j+1} is obtained by evaluating the equation of motion at t_{j+1}, thus for this reason the method is implicit. The expressions for velocity and acceleration are given by:[16]

$$\{\ddot{u}\}_{j+1} = \frac{1}{\beta(\Delta t)^2}\left(\{u\}_{j+1} - \{u\}_j\right) - \frac{1}{\beta\Delta t}\{\dot{u}\}_j - \left(\frac{1}{2\beta} - 1\right)\{\ddot{u}\}_j \tag{2.69}$$

$$\{\dot{u}\}_{j+1} = \frac{\gamma}{\beta\Delta t}\left(\{u\}_{j+1} - \{u\}_j\right) + \left(1 - \frac{\gamma}{\beta}\right)\{\dot{u}\}_j + \Delta t\left(1 - \frac{\gamma}{2\beta}\right)\{\ddot{u}\}_j \tag{2.70}$$

Here γ and β are user defined numerical constants, which control accuracy and stability of the transient analysis, respectively. Substitution of Equations (2.69) and (2.70) into Equation (2.63b) yields the expression:

$$\begin{aligned}[M]\left(\frac{1}{\beta(\Delta t)^2}\left(\{u\}_{j+1} - \{u\}_j\right) - \frac{1}{\beta\Delta t}\{\dot{u}\}_j - \left(\frac{1}{2\beta} - 1\right)\{\ddot{u}\}_j\right) \\ +[C]\left(\frac{\gamma}{\beta\Delta t}\left(\{u\}_{j+1} - \{u\}_j\right) + \left(1 - \frac{\gamma}{\beta}\right)\{\dot{u}\}_j + \Delta t\left(1 - \frac{\gamma}{2\beta}\right)\{\ddot{u}\}_j\right) + [K]\{u\}_{j+1} = \{F\}_{j+1}\end{aligned} \tag{2.71}$$

Upon simplification of Equation (2.71), the expression to calculate the displacement vector $\{u\}_{j+1}$ is given by:

$$\begin{aligned}\left(\frac{1}{\beta(\Delta t)^2}[M] + \frac{\gamma}{\beta\Delta t}[C] + [K]\right)\{u\}_{j+1} = \{F\}_{j+1} + \left(\frac{1}{\beta(\Delta t)^2}[M] + \frac{\gamma}{\beta\Delta t}[C]\right)\{u\}_j \\ + \left(\frac{1}{\beta\Delta t}[M] - \left(1 - \frac{\gamma}{\beta}\right)[C]\right)\{\dot{u}\}_j + \left(\left(\frac{1}{2\beta} - 1\right)[M] - \Delta t\left(1 - \frac{\gamma}{2\beta}\right)[C]\right)\{\ddot{u}\}_j\end{aligned} \tag{2.72}$$

Thus if $\{u\}_j, \{\dot{u}\}_j, and \{\ddot{u}\}_j$ are known, then $\{u\}_{j+1}$ can be found, with $\{\dot{u}\}_{j+1}$ and $\{\ddot{u}\}_{j+1}$ found using Equations (2.69) and (2.70). There is no special starting procedure for this method, other that finding the acceleration vector at time t=0, thus the time-history iterations begin with j=0. This method is unconditionally stable provided that $\gamma \geq 1/2$ and $\beta \geq \gamma/2$.[15] If the constant γ=0.5, then the method is second order accurate (i.e., error is of the order $(\Delta t)^2$), and there is no artificial (or numerical) damping in the solution. Numerical damping is controlled

by the parameter γ, and as γ increases above 0.5, numerical damping increases. If numerical damping is used, the analysis is only first order accurate. Also, if numerical damping is desired, then taking $\beta = 1/4(\gamma + 1/2)^2$ maximizes the high frequency dissipation in the solution. For the purposes of this study, numerical damping is used at times in order to eliminate the artificial response found in certain simulations. This will be discussed further in Section 2.6, with the effects of changing the constant γ shown. If numerical damping is unwanted, experience has also shown that using $\gamma = 1/2$ and $\beta = 1/4$ (i.e., trapezoidal rule) provides the best results.[15] To ensure accuracy a time step of $\Delta t = \frac{\pi}{50\omega_o}$ is typically used, similar to most implicit methods.

A special case of the Newmark method is when the constant β=0, which makes the Newmark method explicit.[15] The same linear acceleration approximation is assumed, but a slightly different formulation to the solution algorithm will be presented. Here, the displacement and velocity at time t_{j+1} are given by the expressions:

$$\{u\}_{j+1} = \{u\}_j + \Delta t\{\dot{u}\}_j + \frac{\Delta t^2}{2}\left((1-2\beta)\{\ddot{u}\}_j + 2\beta\{\ddot{u}\}_{j+1}\right) \tag{2.73}$$

$$\{\dot{u}\}_{j+1} = \{\dot{u}\}_j + \Delta t\left((1-\gamma)\{\ddot{u}\}_j + \gamma\{\ddot{u}\}_{j+1}\right) \tag{2.74}$$

Substitution into Equation (2.63b) yields the following expression:

$$\begin{aligned}[M]\{\ddot{u}\}_{j+1} + [C]\left(\{\dot{u}\}_j + \Delta t\left((1-\gamma)\{\ddot{u}\}_j + \gamma\{\ddot{u}\}_{j+1}\right)\right) \\ + [K]\left(\{u\}_j + \Delta t\{\dot{u}\}_j + \frac{\Delta t^2}{2}\left((1-2\beta)\{\ddot{u}\}_j + 2\beta\{\ddot{u}\}_{j+1}\right)\right) = \{F\}_{j+1}\end{aligned} \tag{2.75}$$

Setting β=0 and further simplifying Equation (2.75) yields the expression to find $\{\ddot{u}\}_{j+1}$ as:

$$\begin{aligned}\left([M] + \Delta t\gamma[C]\right)\{\ddot{u}\}_{j+1} = \{F\}_{j+1} - [K]\{u\}_j - \left([C] + \Delta t[K]\right)\{\dot{u}\}_j \\ - \left(\Delta t(1-\gamma)[C] + \frac{\Delta t^2}{2}[K]\right)\{\ddot{u}\}_j\end{aligned} \tag{2.76}$$

Thus, if $\{u\}_j, \{\dot{u}\}_j, and \{\ddot{u}\}_j$ are known, then $\{u\}_{j+1}$ can be found. The displacement, $\{u\}_{j+1}$ and velocity, $\{\dot{u}\}_{j+1}$ are found using Equations (2.73) and (2.74), with β=0. The starting procedure and time-history iterations are the same as for the implicit Newmark method. The numerical damping is also controlled by the constant γ, where if γ=0.5 there is no numerical damping and second order accuracy is attained. Furthermore, this explicit method is only

conditionally stable since β=0. The stability limit is set on the time step size based on the Courant, Friedrichs, and Lewy (CFL) condition.[15] This condition states that the time step must be small enough so that information does not propagate across more than one element per time step. The mathematical representation is given by:

$$\Delta t \le C_{n_{FE}} \frac{\Delta L}{C} \tag{2.77}$$

The wave speed is given by $C = \sqrt{\frac{E(1-\nu^2)}{\rho}}$, where E is the material modulus of elasticity, ν is the material Poisson's ratio, and ρ is the material density. The term ΔL is the element size and C_{nFE} is the Courant number. The wave speed is found for each material in the mesh, and the largest is used in Equation (2.77). The element size used for the time step calculation must be determined by finding the smallest dimension of an element, and comparing to all other elements in the mesh, which is simple since the mesh used in this study is structured. Also, the FE Courant number is set to a value of 0.5 for all simulations in this study, unless otherwise specified.

The second explicit method used in this study is the central difference method, which consists of expressing velocity and acceleration at time t_j in terms of displacements at times t_{j-1}, t_j, and t_{j+1} using a central difference scheme. The assumption is that the response curve over time is approximated by a quadratic polynomial, given as $u = at^2 + bt + c$, $-\Delta t \le t \le \Delta t$, where t is an arbitrary point in time. Differentiating this expression with respect to t, while using a Taylor series expansion gives the expressions for velocity and acceleration as:[16]

$$\{\dot{u}\}_j = \frac{1}{2\Delta t}\left(\{u\}_{j+1} - \{u\}_{j-1}\right) \tag{2.78}$$

$$\{\ddot{u}\}_j = \frac{1}{(\Delta t)^2}\left(\{u\}_{j+1} - 2\{u\}_j + \{u\}_{j-1}\right) \tag{2.79}$$

The error in these approximations is of the order $(\Delta t)^2$, thus the method is second order accurate. Substitution of Equations (2.78) and (2.79) into Equation (2.63a) yields:

$$\frac{1}{(\Delta t)^2}[M]\left(\{u\}_{j+1} - 2\{u\}_j + \{u\}_{j-1}\right) + \frac{1}{2\Delta t}[C]\left(\{u\}_{j+1} - \{u\}_{j-1}\right) + [K]\{u\}_j = \{F\}_j \tag{2.80}$$

Simplification of Equation (2.80) yields the equation to solve for the displacement vector as:

$$\left(\frac{1}{(\Delta t)^2}[M]+\frac{1}{2\Delta t}[C]\right)\{u\}_{j+1}=\{F\}_j+\left(\frac{2}{(\Delta t)^2}[M]-[K]\right)\{u\}_j-\left(\frac{1}{(\Delta t)^2}[M]-\frac{1}{2\Delta t}[C]\right)\{u\}_{j-1} \quad (2.81)$$

To start the time integration at j=0, $\{u\}_{-1}$ and $\{u\}_0$ must be known. The $\{u\}_0$ vector can be found using the original equation of motion, assuming that $\{\dot{u}\}_o$ and $\{\ddot{u}\}_o$ are known. The $\{u\}_{-1}$ term can be approximated from the equation given by:

$$\{u\}_{-1}=\{u\}_o-\Delta t\{\dot{u}\}_o+\frac{1}{2}(\Delta t)^2\{\ddot{u}\}_o \quad (2.82)$$

This explicit method is also conditionally stable, where the limit for the maximum time step is given by the CFL condition in Equation (2.77). Note that the central difference method does not allow for any artificial damping, as do the other implicit and explicit methods presented above.

When comparing the four time integration methods presented, it becomes evident that some may be better suited for computational economy, while others for accuracy. For example, consider the two explicit methods presented by analyzing Equations (2.76) and (2.81). Notice that the system stiffness matrix does not appear in either equation on the left-hand side. Thus, if a lumped mass matrix and a mass proportional damping model are used, the solution to the linear equation becomes trivial since a diagonal matrix results on the left-hand side. This greatly reduces computational time, allowing for significant mesh refinements. An obvious disadvantage is the limitation on the time step, which is overcome when using either of the two implicit methods. The disadvantage with the implicit methods is that they are much slower computationally versus the explicit methods. Also, an advantage with the two Newmark methods over the Houbolt and central difference methods is the ability to control numerical damping. The disadvantage in this is the reduced accuracy, which is not the case otherwise. Some preliminary results comparing the various time integration methods are included in the subsequent section.

2.6 Preliminary FE Component Results

2.6.1 Verification of Algorithm, Natural Frequencies and Damping Ratio

As with any FE algorithm or numerical model, it is necessary for the results to be verified. This is done to ensure that the FE component provides reliable and accurate solutions, which is critical for the overall simulation. Common practice for the generation of in-house FE algorithms is to compare the results to commercially available algorithms, and the solutions of similar problems using other methods (numerical or analytical). Thus, the purpose of this section is to take output from the FE component and compare it to output produced by the commercial finite element solver ANSYS.[17] Also transient results produced by Greatrix and Kudriavtsev,[22] using the commercial program CFD ACE+, will be compared to the transient results produced by the FE component. The FE verification for the presented cylindrical grain motor includes static, free vibration, and transient results. Also, a discussion on the choice of the natural frequencies and damping ratios used for the presented damping model will be included here.

The first static solution is performed in order to test the accuracy of the calculated nodal forces caused by the applied internal chamber pressure on the presented model, and to test the solvers of the FE component. The equation governing the static motion is given by Equation (2.55), and the solution is detailed in Section 2.5.1. The model tested here contains the solid propellant, aluminium casing and the steel sleeve. In order to simplify the model, the head end face plate and nozzle are not included in the element mesh. Thus, the model tested is similar to that shown in Figure 2-3, with a slightly refined mesh. Also, the model is constrained to move in the radial direction only, which is representative of the actual response for a constant applied pressure on the inner propellant surface. Thus, both the grain at the head-end and nozzle-end is restricted from moving in the axial direction. The constant pressure applied to the inner propellant surface representing the chamber pressure is 10.5-MPa. The same 20 node hexahedral element, 882 node mesh that is tested using ANSYS is used to test the static capabilities of the FE component algorithm. The outward radial

displacement values for the inner propellant surface, the aluminium inner surface, and the outer steel surface are shown in Figure 2-15, and are denoted as u_1, u_2 and u_3 respectively.

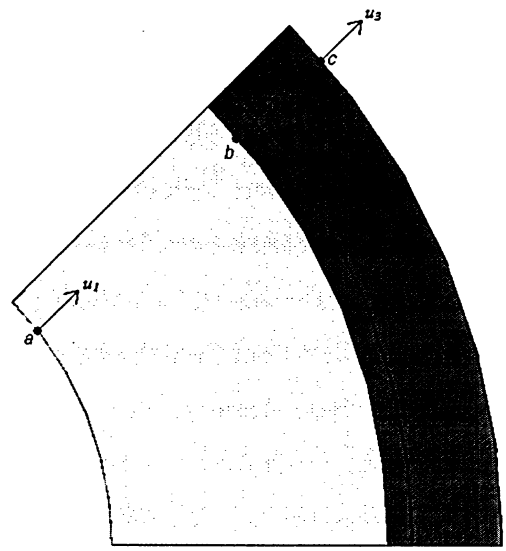

Figure 2-15 SRM two-dimensional schematic of static displacements

The results from ANSYS and the FE component are presented in the Table 2-4. The percent error of the inner propellant surface displacement for the FE component is calculated using the ANSYS value as the reference. The difference in the results between the FE component and the commercial package ANSYS is negligible, thus the accuracy of the FE component solvers and model are demonstrated.

Solver	u_1 (μm)	u_2 (μm)	u_3 (μm)	% error (u_1)
FE Algorithm	103.37	11.54	10.54	0.01
ANSYS	103.38	11.54	10.54	-----

Table 2-4 First static test results

A second static analysis is performed on the presented motor, in this case with the intention of comparing the FE component results (or simply the numerical idealized results) to the analytical static solution. This has the same affect of a 'patch test', since the numerical model is tested with an analytical model. To simplify the analytical solution, the aluminium casing of the previous motor of the first static test is replaced with a steel casing. The same constraints and applied pressure used in the first static test are used here. The outward radial

motion shown in Figure 2-15 is applicable here, except that u_2 represents the steel inner surface radial displacement. Thus, the presented constrained motor to be used for the second static test, with constant internal pressure, somewhat resembles a thick-walled composite cylinder under constant internal loading. Also, since the motor ends are not modeled and left free, a plane strain assumption can be used in this particular case of FE static testing.[23] This is physically incorrect since the motor structure is three-dimensional and its ends are modeled in the simulations; however, in order to have a simple analytical solution for comparison, this is necessary. To reemphasize, the plane strain assumption is only applicable here for the preliminary static testing and not for the actual model used in the simulations.

The governing differential equation for the displacement field in the radial direction of a thick-walled cylinder, neglecting any thermal effects and body loads, is given by:[23]

$$\frac{d^2u}{dr^2}+\frac{1}{r}\frac{du}{dr}-\frac{u}{r^2}=0 \tag{2.83}$$

where u is the displacement of a point in the radial direction, given by r. Equation (2.83) can be integrated to obtain a homogeneous solution for u, given by:

$$u=c_1r+\frac{c_2}{r} \tag{2.84}$$

where terms c_1 and c_2 are constants. The radial and tangential stress components for a plane strain case are found via:[23]

$$\sigma_r=\frac{Ec_1}{(1+\nu)(1-2\nu)}-\frac{Ec_2}{(1+\nu)r^2}. \tag{2.85}$$

$$\sigma_\theta=\frac{Ec_1}{(1+\nu)(1-2\nu)}+\frac{Ec_2}{(1+\nu)r^2} \tag{2.86}$$

The displacement given by Equation (2.84) is applicable to both the propellant and steel portions of the cylinder being tested. Thus, there are actually two equations and four constants to be solved as shown below. Refer to Figure 2-15 for radial locations a, b and c.

$$u_{steel}=c_1r+\frac{c_2}{r}, \text{ for } b\le r\le c \tag{2.87a}$$

$$u_{propellant}=c_3r+\frac{c_4}{r}, \text{ for } a\le r\le b \tag{2.87b}$$

Equations (2.85) and (2.86) can similarly be applied to both the steel and propellant materials, with the corresponding modulus and Poisson's ratio. In order to solve the four

constants, and thus the equations for radial displacement, the boundary conditions for the cylinder must be determined. When the radius is equal to a (i.e., $r = a$), the radial stress is equivalent to the applied pressure, $-p$. At radius $r = b$, the radial stress and displacement in the propellant is equal to the radial stress and displacement in the steel, respectively. At radius $r = c$, there is no applied pressure, thus the radial stress is equal to zero. Implementing these boundary conditions to the above equations yields the following expressions.

$$-p = \frac{E_{prop} c_1}{(1+\nu_{prop})(1-2\nu_{prop})} - \frac{E_{prop} c_2}{(1+\nu_{prop}) a^2} \tag{2.88a}$$

$$\frac{E_{prop} c_1}{(1+\nu_{prop})(1-2\nu_{prop})} - \frac{E_{prop} c_2}{(1+\nu_{prop}) b^2} = \frac{E_{st} c_3}{(1+\nu_{st})(1-2\nu_{st})} - \frac{E_{st} c_4}{(1+\nu_{st}) b^2} \tag{2.88b}$$

$$c_1 b + \frac{c_2}{b} = c_3 b + \frac{c_4}{b} \tag{2.88c}$$

$$0 = \frac{E_{st} c_1}{(1+\nu_{st})(1-2\nu_{st})} - \frac{E_{st} c_2}{(1+\nu_{st}) c^2} \tag{2.88d}$$

Thus, there are four equations and four unknowns (the constants c_1, c_2, c_3, and c_4) and the solution is straightforward. Now, Equation (2.87) can be solved for displacements at points a, b, and c knowing the applied pressure p and material properties.

The analytical results for the displacements at radial locations a and c are found, as are the displacements of the FE component found at the same corresponding radial locations. The 8-node hexahedral elements are used for this patch test, where results for various meshes refined in the radial direction are compared to the analytical results. All the results from the meshes tested are not included here, but some results to shown the effect of refining the element mesh are included in Table 2-5.

Analysis	u_1 (μm)	u_3 (μm)	% error (u_1)	% error (u_3)
Analytical	100.22	8.98	-----	-----
FE – 1300 element mesh	100.05	8.88	0.17 %	1.11 %
FE – 14400 element mesh	100.25	9.01	0.03 %	0.33 %
FE – 24000 element mesh	100.25	9.01	0.027 %	0.33 %

Table 2-5 Second static test results

Both sets of results are shown, with corresponding percent errors found for the FE component results, which are relative to the analytical solution results. As the mesh is refined, the error in the displacement values tends to decrease, up until a certain point. Beyond this point, refining the mesh will no longer be necessary for increasing the accuracy of the results. It should also be noted that refinement of the radial mesh does not affect the results significantly since the percent errors for the coarse mesh are somewhat low. However, the refinement of the mesh in the axial direction will affect the actual simulation because of the significant axial motion caused by the traveling shock wave. Effects of this will be shown from the simulation results in Chapter 5. The radial motion of the static test is not affected by refining the mesh axially. The patch test for the three dimensional hexahedral elements is successful, which validates the model accuracy with respect to the physical structure. Also, since refining the mesh in the radial direction does not significantly improve results, a coarse mesh in the radial direction may be warranted in order to reduce computation time significantly.

Next, the free vibration results of the FE component algorithm will be compared to those found using ANSYS. The free vibration analysis consists of extracting the eigenvalues of the FE system, where the eigenvectors are not of primary importance. The accuracy of the calculated natural frequencies is important since the natural frequencies are necessary for the formulation of the damping model used in the transient analysis. As for the first static analysis, the head end and nozzle are not incorporated in the mesh. For the purposes of this free vibration test, the same constraints and model used in the first static test are used here. An 882 node, 8-node hexahedral element mesh is used for the free vibration analysis. The governing equations and solution methodology are found in Section 2.5.2, where a lumped mass matrix is used for this particular analysis. The rigid body constraints on the SRM structure are set to prevent any tangential motion, and to prevent any axial motion of both motor ends. The eigenvalues calculated by the FE algorithm are compared to those extracted from ANSYS, where the first 10 natural frequencies are shown in Table 2-6. For the most part, the eigenvalues are similar but some deviate slightly from those found by ANSYS.

ANSYS - Modal		FE Algorithm	
Eigenvalue	Frequency (Hz)	Eigenvalue	Frequency (Hz)
124900778.9	1778.7	124901818.23	1778.71
136022036.7	1856.2	135982944.32	1855.93
147632797.2	1933.8	147446253.76	1932.58
500080727.6	3559.1	499070719.19	3555.50
764788616.3	4401.4	764704063.79	4401.16
966929130.5	4949.0	965816271.10	4946.15
1138265588.0	5369.6	1128911355.38	5347.49
1170457112.0	5445.0	1170320519.55	5444.68
1570183140.0	6306.6	1562311733.81	6290.77
1601760920.0	6369.7	1585384797.33	6337.05

Table 2-6 Free vibration results

The reason for this is that the numerical techniques used in ANSYS to solve for the eigenvalues differ from those of the FE algorithm, thus small variations in the eigenvalues are common with different numerical methods.[16] Also, the convergence criteria for the eigensolution may be different, which could account for the deviations. Nonetheless, the magnitudes of the eigenvalues are close to those found by ANSYS, and are accurate enough for the damping model. During the FE testing, various natural frequencies within a small range are used to formulate the damping model, and it is found that the transient results using the slightly different natural frequencies are almost identical to one another. Thus, since a small variation in the natural frequency does not alter the transient results a significant amount, the extracted eigenvalues of the FE algorithm are assumed to be accurate.

In order to test the transient solvers and solution of the FE component, the presented cylindrical grain motor is subjected to a 10.5-MPa step increase in chamber pressure, from zero initial displacement and velocity, applied to the inner propellant surface. The response of the structure is then allowed to freely decay to an equilibrium position with the 10.5-MPa pressure continuously applied. An 8-node hexahedral, 520 element mesh is used for the transient testing, with the same constraints and model used for the first static test. The governing equations and solution methodology are found in Section 2.5.3. The frequencies used for the Rayleigh damping model are 1780 Hz (~ 11180 rad/s) and 14325 Hz (~ 90000 rad/s), representing the first natural of the system and the maximum response frequency of the system, respectively. The damping ratios are both set to 0.1, in order to compare to the

transient results of the same motor found by using the commercial FE package CFD ACE+. The time integration method used here is the implicit Newmark method ($\beta = 0.25$), with second order accuracy maintained (i.e., $\gamma = 0.5$). Various time step sizes are tested, each producing identical results. A lumped mass matrix is also used in the analysis for the purpose of being consistent with the free vibration testing natural frequencies in use.

The motors radial response over a 0.7 ms time interval is shown below in Figure 2-16. From the figure, the damped oscillation frequency is approximately 14285 Hz, which should be close to the expected value of 14254 Hz, using the maximum response frequency, as defined by:

$$\omega_d = \omega_n \sqrt{1-\zeta^2} \tag{2.89}$$

The settling time is also approximately 0.45 ms, which corresponds to the literature very well.[22] The settling time for a second order under-damped mechanical system is given by:[24]

$$T_s = \frac{4}{\zeta \omega_n} \tag{2.90}$$

Thus, the value is expected to be 0.43 ms, which is shown by the structures response. The equilibrium displacement value reached by the motor after settling is equivalent to the static deflections under the same applied internal chamber pressure, as expected. Also, the peak time values corresponding to the maximum initial response for the propellant inner surface and steel sleeve outer surface are given by:[24]

$$T_p = \frac{\pi}{\omega_n \sqrt{1-\zeta^2}} \tag{2.91}$$

Peak time should be approximately 0.035 ms. Referring to Figure 2-16, the peak times are approximately 0.03 ms, which corresponds well to the expected values. Note that a damping ratio of 0.1 should reduce the amplitudes of the displacements off the equilibrium value by about 50% as discussed by Thomson and Dahleh.[21] This is evident in the transient solution displacement plots. Also consider the logarithmic decrement for a damped second order system with the same transient response as defined by:[21]

$$\delta = \ln\left(\frac{u_1}{u_2}\right) = \zeta \omega_n \tau_d = \frac{2\pi\zeta}{\sqrt{1-\zeta^2}} \tag{2.92}$$

Here, the two displacement terms u_1 and u_2 are defined as the values of the first and second displacement amplitudes of the transient response off the equilibrium value, where the oscillation period is given as τ_d. From the literature, the expected decrement value should be approximately 0.6315, and from the presented plot the actual value was found to be 0.62. The displacement amplitude values, as shown through the logarithmic decrement, are within the expected range defined in the literature, and are in compliance with vibration theory.

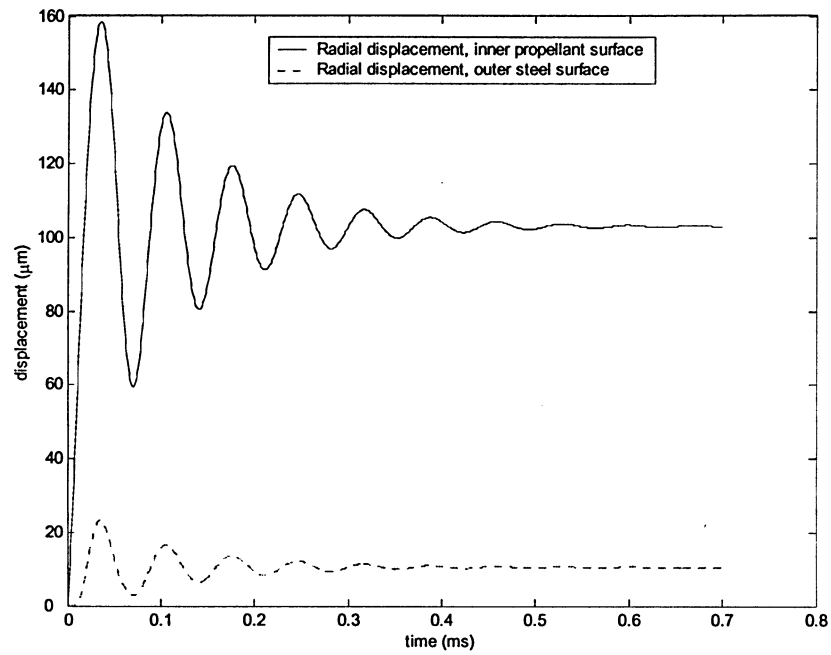

Figure 2-16 Transient testing: displacements

In order to verify the presented transient results, similar results found in the literature are reproduced to compare the FE component results. Greatrix and Kudriavtsev[22] completed the same transient analysis of the same motor, subjected to a 10.5-MPa step increase in pressure, using a structural model component of CFD ACE+ called FEMSTRESS. A damping ratio of 0.1 was also used, with a different time integration method. The CFD ACE+ inner propellant surface displacement results are superimposed on the same plot of the FE component results given in Figure 2-16, and are shown in Figure 2-17. From the plot, it is evident that the FE component results are almost identical to the results produced using CFD ACE+. The deviations of the two plots are always less than 0.1 %, when comparing the maximum and minimum points on the plots. The damped response frequencies and settling

times are also identical, which shows the excellent correlation. Any slight discrepancies in the plots can be attributed to the different time integration methods, damping models and elements used in the analyses. Also, the radial acceleration of the propellant surface is an important part of the overall simulation. Slight deviations and numerical noise in the radial acceleration developed over time can cause amplified effects in the simulation because of the acceleration effects in the burning rate algorithm. For this reason, the acceleration results of both the FE component and CFD ACE+ are added here for comparison, and are shown in Figure 2-18. The consistency in the acceleration profile is similar to the displacement plots, where the FE component closely matches the CFD ACE+ results. The only deviation of the two plots is the initial acceleration values at the start of both transient analyses. This can solely be attributed to the fact that different time integration methods are used. The CFD ACE+ results are found using an explicit time solver, while the FE component results are found using an implicit method. These two types of methods tend to produce slightly different results initially because of different starting procedures.[15] This does not affect the analysis later in simulation time, thus is not an issue to be concerned with. A plot of the propellant radial velocity profile not included here, also correlates well with the CFD ACE+ data, which is expected.

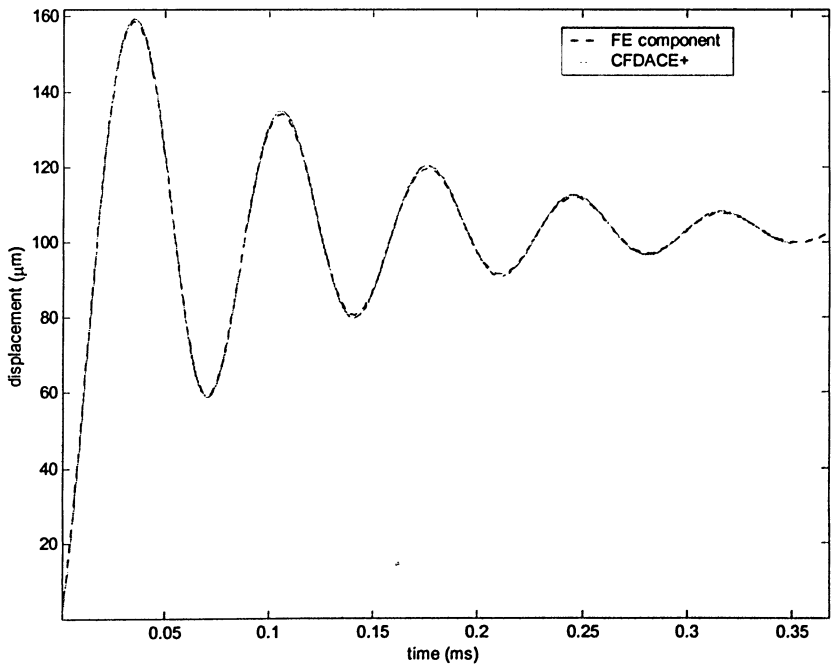

Figure 2-17 Transient results comparison: displacement

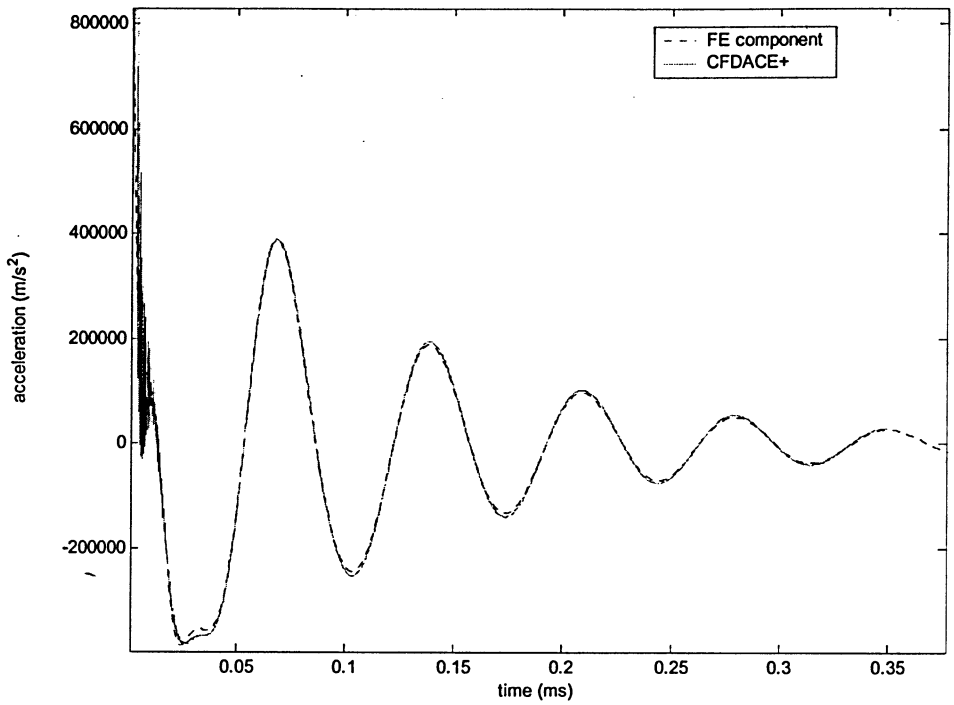

Figure 2-18 Transient results comparison: radial acceleration

The FE transient analysis as a whole is successful in that the results correlate well with other numerical data, and also with the linear vibration theory. The static and free vibration testing also produced exceptional results. Now that the FE component has been validated based on the produced structural results, a discussion of the natural frequencies and damping ratios used in the damping model follows. As mentioned, the accuracy of the natural frequencies to be used in the damping model is important. A free vibration analysis for a particular FE mesh and mass matrix results in the natural frequencies of the system. From this analysis, the first natural frequency of the system is simply used as ω_1 for the Rayleigh damping model. The difficulty is determining the maximum response frequency of the system (i.e., ω_2 for the Rayleigh damping model or ω_2 for the mass/stiffness proportional damping models). This is usually the frequency that is most dominant in the system; thus, it would produce a large response in the system when exposed to a periodic excitation. Typically, to find the most dominant frequency of a system, a harmonic analysis is performed using the natural frequencies of the system as the excitation frequencies. Damping is set to zero, and the equation of motion becomes:[21]

$$[M]\{\ddot{u}\}+[K]\{u\}=\{F_o\}\sin\omega t \tag{2.93}$$

Here, $\{F_o\}$ is a constant force vector of arbitrary amplitude, ω is the excitation frequency, and t is the corresponding time. This expression can be solved approximately using any of the aforementioned direct time integration methods, or solved accurately by doing a full harmonic solution. If a full harmonic solution is required, the response is approximated by $\{u\}=\{\bar{U}\}\sin\omega t$, and Equation (2.93) becomes:[21]

$$\left([K]-\omega^2[M]\right)\{\bar{U}\}=\{F_o\} \tag{2.94}$$

A solution for every natural frequency of the system is required to find which frequency is the most dominant in the system, using either Equation (2.93) or (2.94). If approximating the analysis using a transient solver, the displacement vector $\{u\}$ must be tracked over time for all natural frequencies. If using a steady-state harmonic solution, the amplitude vector $\{\bar{U}\}$ must be calculated for each natural frequency. The frequency that produces the largest displacement amplitude is the most dominant frequency of the system. In either case, the solution methodology is tedious for systems with many degrees-of-freedom. However, a simpler solution does exist, where a transient solution can be employed to approximate the system response frequency. Applying an impulse pressure to the system of arbitrary magnitude without damping, and recording its response will approximate the dominant natural frequency. Once this frequency is found, the few system natural frequencies in the vicinity of the approximated dominant natural frequency can be tested using the steady-state harmonic solution of Equation (2.94). The dominant frequency is then found based on the reduced harmonic solution, which requires far less computation time versus testing all system natural frequencies. Note that when doing harmonic testing, one degree-of-freedom in the system should be tested at different natural frequencies. The choice of this degree-of-freedom is arbitrary since under harmonic response, all degrees-of-freedom in a system respond with the same frequency.[21] This transient approximation along with a reduced harmonic analysis is necessary to determine the response frequency when using mass or stiffness proportional damping, since an accurate ω_2 value is desired. However, for a Rayleigh damping model, the approximate transient solution is good enough to determine ω_2 since the frequency is an upper limit and an approximate response frequency value is accurate enough as observed for this study.

For the different FE meshes used in this study, the calculated natural frequencies did not vary significantly from one mesh to the next unless the mesh is extremely unrefined (not the case here). Also, meshes with either the 8-node or 20-node hexahedral elements provide similar results, with respect to response frequency. Thus, the only factor that influences the natural frequency values is the mass matrix. Typically, a consistent mass matrix will overestimate the calculated natural frequencies, while a lumped mass matrix underestimates the calculated natural frequencies.[15] For the various meshes presented, the first natural frequency of the system is typically found to be approximately 1780 Hz when the mass matrix is lumped and 1790 Hz when a consistent mass matrix is used. For all meshes used in the simulations, the maximum response frequency is found to be approximately 14325 Hz for a lumped mass matrix and 15255 Hz for a consistent mass matrix. This corresponds well to the response frequency found in the literature, for the same SRM.[22] A plot of the inner propellant surface radial displacement at the motor head-end is shown in Figure 2-19, where the motor is subjected to a 10.5-MPa impulse pressure and damping is zero. This particular plot is for an 8-node hexahedral mesh of 520 elements, using a lumped mass matrix. Note that the smooth motion that is typical for a harmonic response is not the result of the transient analysis. As mentioned, a transient analysis will approximate the response frequency, where a series of harmonic analyses must follow for a precise calculation of the actual response frequency of the system. Also, note that for the SRM simulated firings the propellant is regressed over time, and thus the FE mesh will have a slightly higher response frequency. This is a typical characteristic of any motor.[1] The FE component is designed to calculate the response frequency for a mesh that is regressed, which is necessary for accuracy in the damping model. As an example consider a regressed propellant FE mesh of the cylindrical grain motor. The first natural frequency is determined to be 1820 Hz (versus 1780 Hz without regressing), and the maximum response frequency is determined to be 15915 Hz (versus 14325 Hz). There is a significant increase in the natural frequency, especially with the maximum response frequency value.

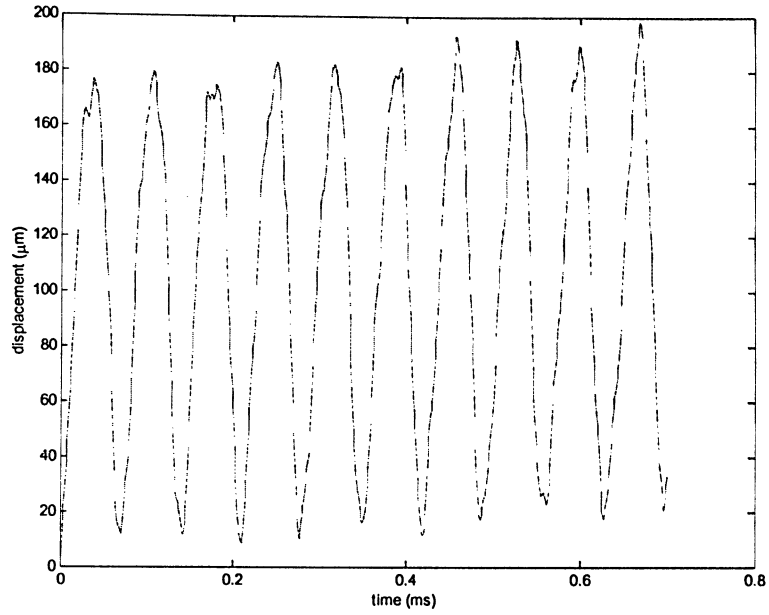

Figure 2-19 Transient response without damping

The damping ratios of the presented damping models are difficult to determine exactly, mainly because the exact damping properties of various materials and structures are not known. This typically leads to approximated damping ratios, followed by a trial-and-error approach to narrow down the range of values. If the relationship illustrated by Figure 2-14 is known for a given structure, the damping ratios could be extracted from the plot using the calculated response frequency values for the respective Rayleigh damping model. This is rarely the case, as the design spectrum shown in Figure 2-14 is difficult to establish. For this reason both damping ratios, in the case of Rayleigh damping, are set to equal values. This simplifies the analysis, and forces the structure to respond at frequencies that are near the desired design spectrum. For the case of mass or stiffness proportional damping, only one damping ratio is required, making the analysis even easier. Previous studies using the same cylindrical motor presented here have had success with a damping ratio in the vicinity of 0.35.[1, 10] All damping ratios to be used for motor simulated firings from here on are in the range of 0.1 to 0.65 (i.e., 10-65 % of critical damping).

2.6.2 Comparison of Various FE Results

In this section, some preliminary results of the FE component will be presented, in order to give insight on the modeling considerations and the FE parameter choices used in this study. These results are important in order to choose the correct parameters and elements for the simulated firings. A discussion on the element types, the mass matrix, the damping model, and the time integration method to be used will follow. In each case, the FE component is run through a transient analysis, similar to that for the transient testing presented in Section 2.6.1. A 10.5-MPa increase in pressure is applied to the structure, and the response of the structure is allowed to decay to its equilibrium position. For each case, a 520 element mesh is used with a damping ratio of 0.1, regardless of the damping model. The first case is presented to compare results between 8-node and 20-node hexahedral elements. Then, the comparison of using a lumped and consistent mass matrix will be presented. Next, the effects of using a Rayleigh damping model and mass proportional damping will be shown. Finally, effects of changing the time integration method will be discussed. In each case, all variables and parameters are held constant, except for the parameters being analyzed.

First, consider a transient analysis with a 20-node hexahedral element mesh. The mass matrix used is consistent and a Rayleigh damping model is used with natural frequencies of 1795 Hz and 15220 Hz, respectively. The implicit Newmark time integration method is employed here, without any artificial damping. The head-end radial displacement profile is shown in Figure 2-20, while the head-end radial acceleration profile is also included in Figure 2-21. The displacement profile is virtually identical to that produced using an 8-node hexahedral mesh (not shown), under the same transient analysis. However, the acceleration profile for the 20-node hexahedral mesh does not correlate well with the 8-node hexahedral mesh results. From Figure 2-21, it is evident that the acceleration profile exhibits a great deal of high frequency low level noise, shown in the inset plot. This is not accurate, and could be detrimental to the simulated firings since the coupled burning rate algorithm will experience a great deal of noise caused by the input acceleration values. The profile should be smooth, without any noise in the solution. Shown below in Figure 2-22 is

the acceleration profile of the last few wave cycles for both the 8-node and 20-node hexahedral element meshes. There is an absence of numerical noise in the acceleration profile for the 8-node hexahedral element mesh. As mentioned, this noise magnitude will affect the simulations due to the coupled FE, flow and burning rate components. The only way to reduce noise in the 20-node acceleration profile is to significantly increase the numerical damping (i.e., set $\gamma > 0.5$). The Newmark time integration constant is required to be increased over 2.0 in order to reduce the numerical noise significantly. This ultimately affects the response and acceleration profiles, thus is not acceptable. The response of the 8-node hexahedral element mesh is deemed to be more accurate because of the absence of numerical noise, which is desired. Typically, the higher order elements are more accurate for vibration analysis;[15] however, this is not the case here since both elements provide results that have the same accuracy. Also, if an explicit time integration method is used along with a lumped mass matrix higher order elements provide even more numerical noise. This should typically be avoided in any vibration analysis. Also as a note, the 8-node elements are much easier to implement into a regression scheme used in this analysis because there are no mid-side nodes. The higher order elements require more difficulty to regress the propellant mesh.

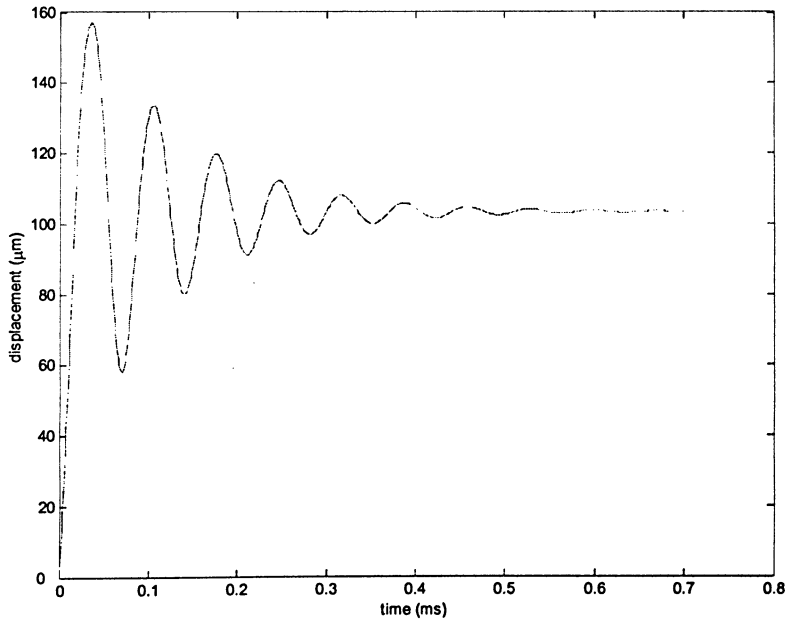

Figure 2-20 Transient response for 20-node hexahedral mesh

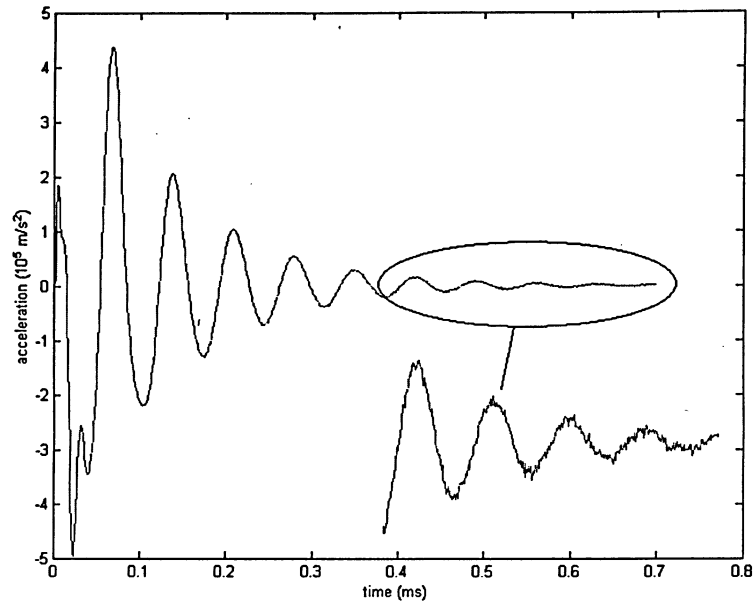

Figure 2-21 Transient acceleration for 20-node hexahedral mesh

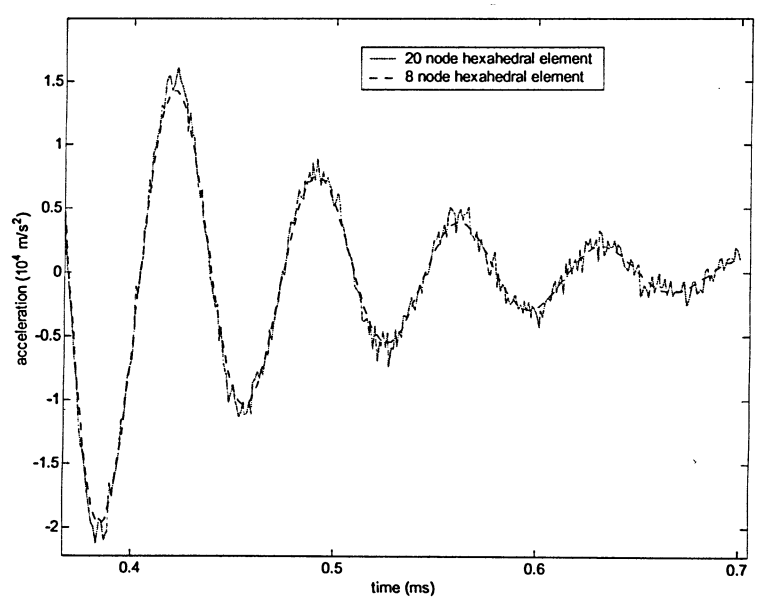

Figure 2-22 Comparison: 8- and 20-node hexahedral elements

Next, consider the same transient analysis using an 8-node hexahedral mesh with a lumped mass matrix in lieu of a consistent mass matrix. The radial acceleration of the propellant surface is shown in Figure 2-23, for both the lumped and consistent mass matrix

transient analysis. The results are virtually identical, with the largest deviation in the acceleration maximum and minimum points being less-than 0.1%. The same correlation exists with the displacement profile, with an even smaller deviation in the displacement maximum and minimum points. This small deviation may have a slight impact on the accuracy of the simulation, but since the difference in the FE component results is negligible, the use of either mass matrix is considered to be accurate. Generally, in a transient time-history analysis, a lumped mass matrix with a linear-displacement field element (i.e., 8-node hexahedral element) works better because of reduced spurious oscillations in the response.[15] Accuracy does not seem to be a large factor; thus, a lumped mass matrix will be used whenever possible to decrease computation time and to decrease physical storage during the simulated motor firings. Generally, for explicit time integration methods a lumped mass matrix is used for reasons of economy. For implicit methods either matrix can be used, as neither will be beneficial for economy.[15] The use of a lumped mass matrix is obviously beneficial for this study as shown.

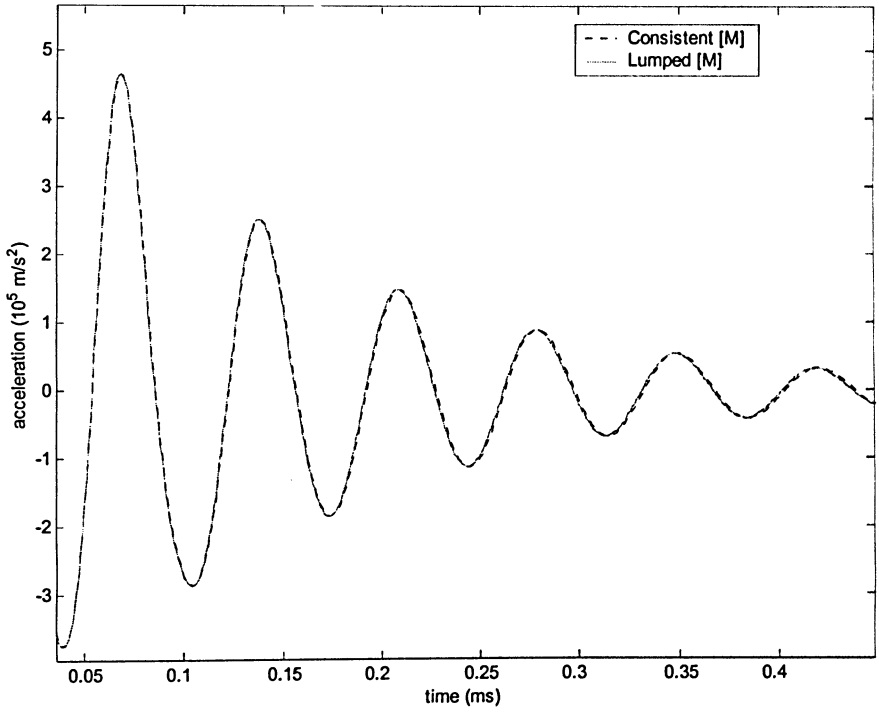

Figure 2-23 Comparison of mass matrices: acceleration

Now, consider the same transient analysis with an 8-node hexahedral element mesh, a lumped mass matrix, and mass proportional damping versus a Rayleigh damping model. The propellant radial displacement and acceleration profiles are included in Figure 2-24 and Figure 2-25, for both types of damping models. From the displacement plot, the noise associated with the mass proportional damping model is evident as it is superimposed on the lower frequency response profile. It is evident that the high frequency spurious oscillations of the mass proportional damping simulation affect the response profile, since the maximum and minimum peak values on the plot differ significantly. This numerical noise is then magnified as shown on the acceleration profile in Figure 2-25. The Rayleigh damping model provides adequate damping, where the mass proportional damping model fails to do so. The main reason that the mass proportional damping model does not damp out the structure is because the stiffness proportional term is ignored. Recall from Figure 2-14 that at higher response frequencies, the stiffness proportional term in the Rayleigh damping model is more significant, whereas the mass proportional term provides negligible damping.

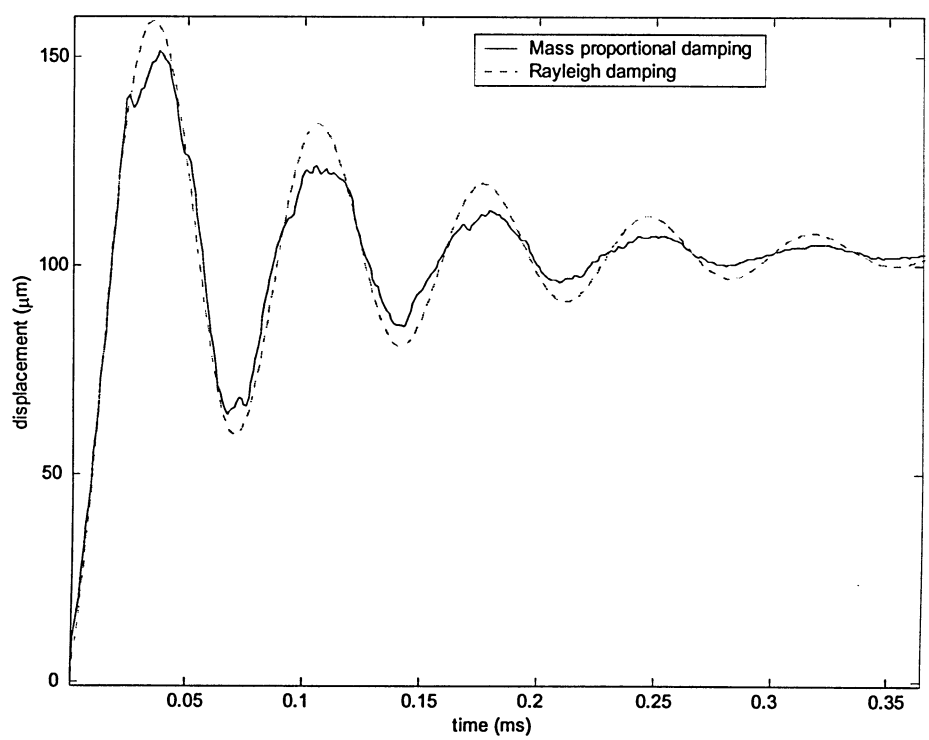

Figure 2-24 Comparison of damping models: displacement

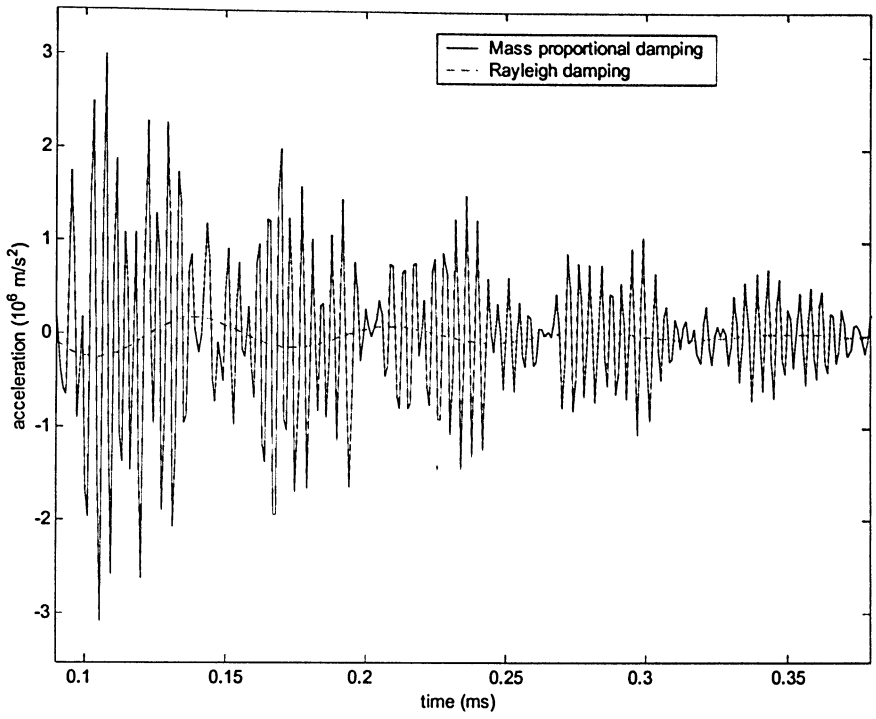

Figure 2-25 Comparison of damping models: acceleration

Since the maximum response frequency (ω_2) used here is in the vicinity of 15000 Hz, the stiffness term has a greater contribution to the overall damping versus the mass term. This is evident in the displacement and acceleration profiles shown above. To validate this point, the same analysis is completed with a stiffness proportional damping model using the same response frequency and damping ratio. The propellant radial displacement and acceleration profiles are not included but are almost identical to those for the Rayleigh damping model shown in Figure 2-24 and Figure 2-25. This result indicates that the mass term in the Rayleigh damping model is almost insignificant relative to the stiffness term. In a simulation case where use of mass proportional damping is necessary (i.e., explicit time integration method), numerical damping must be added to the analysis to damp out some of the numerical noise in the solution. As an example, propellant radial acceleration results from the same analysis with mass proportional damping and added artificial damping is shown in Figure 2-26. The numerical noise experienced in Figure 2-25 has significantly reduced. The maximum and minimum peak acceleration values are not identical, but the numerical problem has been eliminated. Now, to ensure accuracy, the numerical dissipation constant may need to be changed in order to match the peak acceleration values. This

solution provides some accuracy and allows for the simulated firings to be analyzed without numerical errors, however, with the penalty of reduced first order accuracy in the solution.

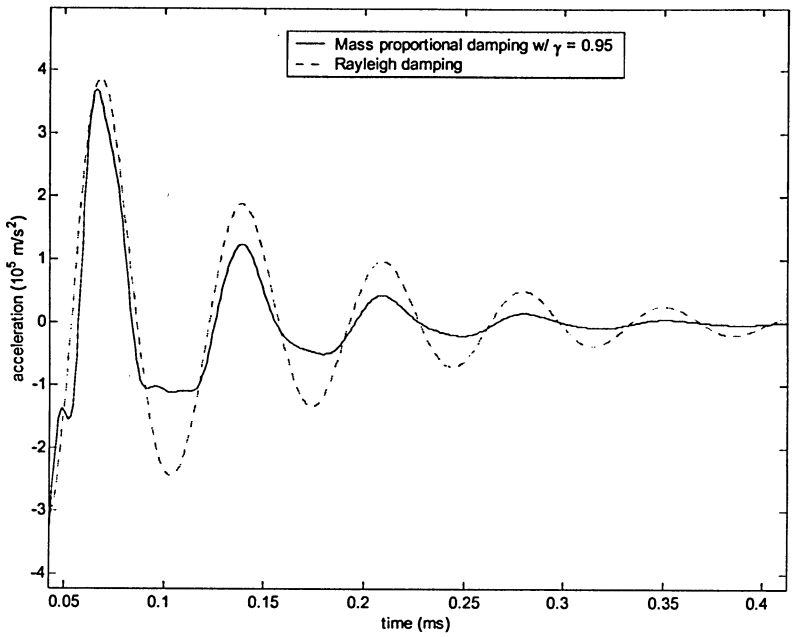

Figure 2-26 Comparison of damping models: acceleration, with artificial damping

Finally, consider the same transient analysis with an 8-node hexahedral element mesh, a lumped mass matrix, a Rayleigh damping model, and different time integration schemes instead of the implicit Newmark method used until now. The theory and solution methodology of each method is found in Section 2.5.3, where the effects that each method has on the FE component results will be shown here. Acceleration results from an analysis using the Houbolt method are shown in Figure 2-27, and are on the same plot as the implicit Newmark results. Also, acceleration results using the central difference method are shown in Figure 2-28, with the implicit Newmark results included for comparison. There is little difference between the results of either method presented; thus, the accuracy of each method is the same. Confidence in each method is found here, where the choice in the method will depend mainly on computationally economical reasons. A similar acceleration profile is found for a transient analysis using the explicit Newmark method, which is not included. The explicit methods are better suited for reduced computation time and storage however, the explicit Newmark method is preferred over the central difference method because the option

of adding numerical damping may be required as mentioned. When using an explicit method mass proportional damping may be used, and as shown numerical damping is required. The main benefit of the implicit methods is the ability to use a larger time step. This may not be beneficial in this particular study because of the explicit flow solver time step limit in the internal ballistic flow component of the simulation. Also, when using the implicit methods a Rayleigh damping model can be used without increasing the computation time of the simulation. This has been shown to provide more accurate results since artificial damping is not required. There is evidently a trade-off between implicit and explicit methods, where the implicit and explicit Newmark methods will be used primarily in the simulated motor firings.

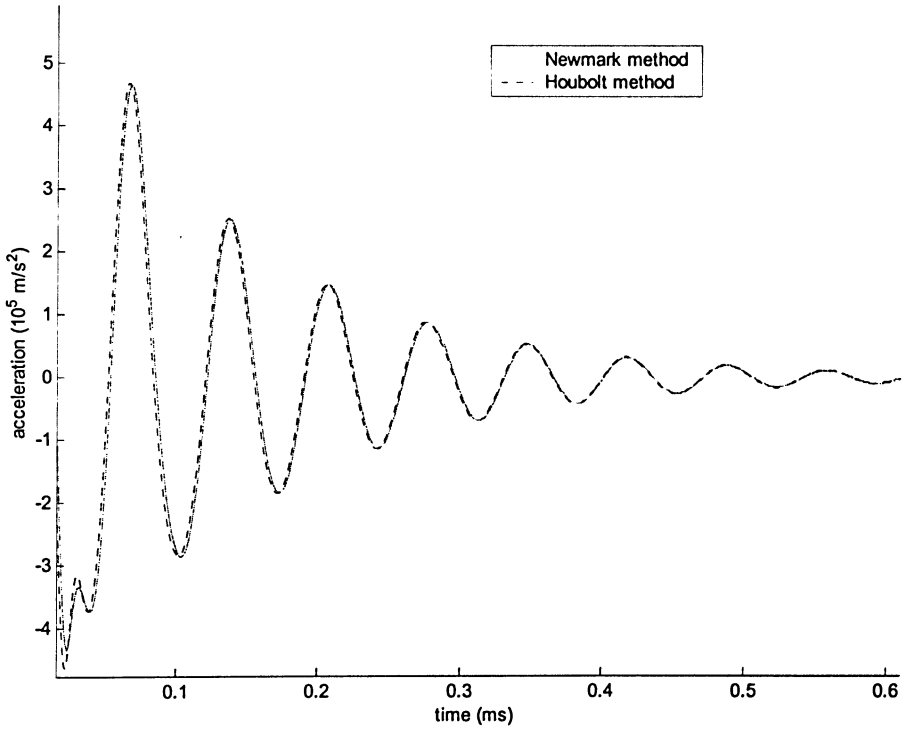

Figure 2-27 Comparison of Newmark method with Houbolt method: acceleration

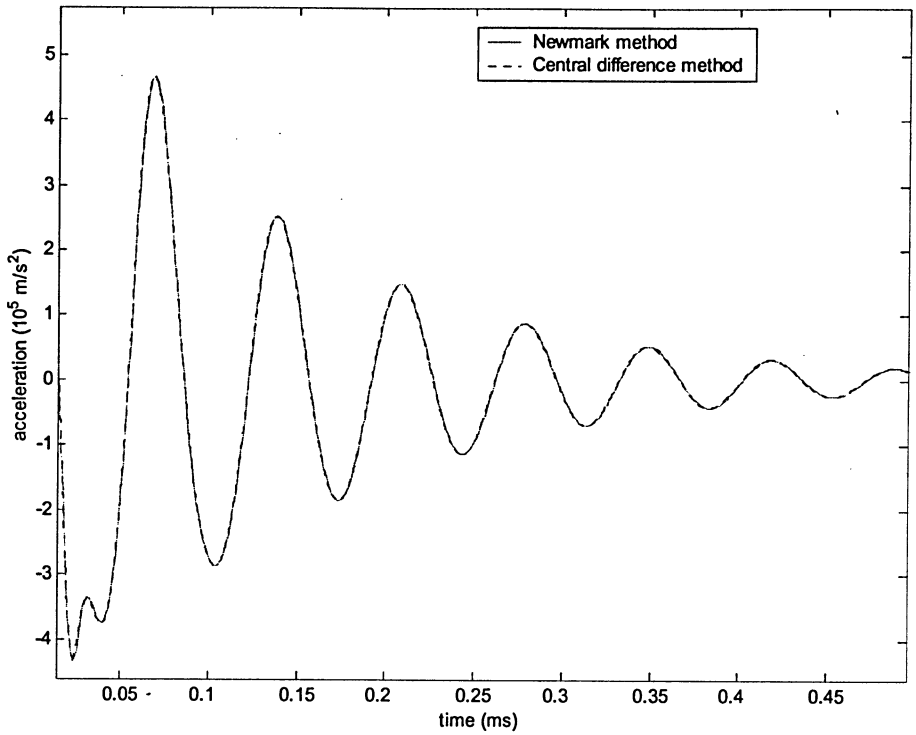

Figure 2-28 Comparison with central difference method: acceleration

2.6.3 FE Component Simulation Choices

Based on the presented FE component results in the previous section, choices are made as to whether certain parameters or time integration methods are chosen over others. It seems obvious that the 8-node hexahedral element is better suited for this analysis than the 20-node hexahedral element, due to the reduced noise in the acceleration profile. It should be noted that if the 20-node element mesh is refined further, the structure will respond more actively because of the reduced stiffness caused by the refined mesh. Also, the lumped mass matrix is better suited than a consistent mass matrix due to reduced computation time and storage requirements. The accuracy in both types of mass matrices is the same; thus, this choice is not detrimental to the motor simulation.

The difficult choices include the time integration method and type of damping model to be used in the simulated motor firings. The mesh refinement is limited when using an implicit time integration method due to the increase in solution computation time at every

iteration for a mesh containing more elements. The obvious solution to this problem is to use an explicit time integration method with mass proportional damping, which is much faster versus any implicit method. This allows for a refined mesh to be used without increasing the computation time to unreasonable limits. The main drawback with this problem solution is the use of mass proportional damping, which in the case of this study is not very accurate, as mentioned. Thus, an obvious trade-off exists between using the implicit methods versus the explicit methods. For the simulated motor firings both methods are analyzed and discussed, and a comparison between the results is made. As an example, consider the plot in Figure 2-29, which illustrates the time required to perform a factorization for various global matrix sizes, *n*. As the total degrees-of-freedom increases, the time required for the factorization increases exponentially. Granted that the factorization is only performed once at the beginning of the FE solution process, the forward and back substitution to solve for the current displacement vector (for example Equation (2.67)) must be performed at every iteration. The relationship between the forward and back substitution time requirements and the total degrees-of-freedom is also exponential, as in Figure 2-29. This is the reason why mesh refinement is limited to a couple of thousand elements when using an implicit method. (Simulations require hundreds of thousands of iterations, thus the mesh cannot be refined greatly.) The required matrix-vector multiplications for each time integration method does not require a great deal of computation time because the multiplications are performed at the element level, which is typically done for transient FE analysis in the literature and in all commercial FE packages.[15]

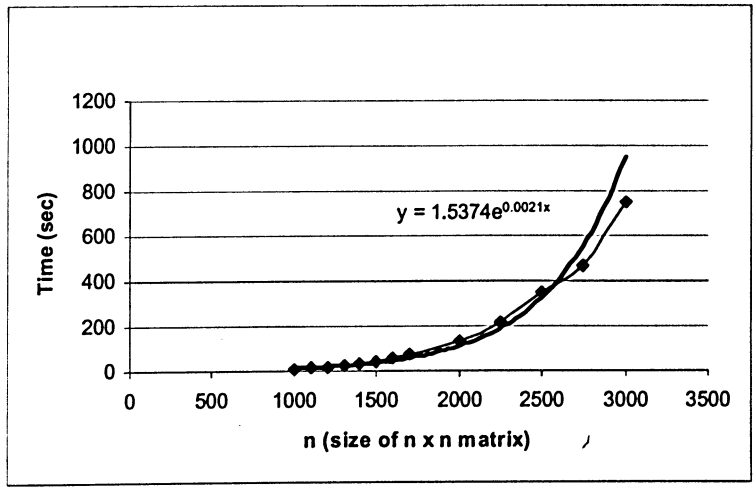

Figure 2-29 Timing of Cholesky Factorization: exponential trend

Finally, consider the axial mesh and the radial response of the FE structure to a simple shock wave introduced suddenly to the inner propellant surface. The radial acceleration at the motor head-end for both the inner propellant surface and the outer steel sleeve are shown in Figure 2-30 and Figure 2-31, respectively. The typical acceleration response to a suddenly applied shock wave (i.e., increase in pressure) would be similar to the profile shown in Figure 2-31, where the negative acceleration peak is slightly less than the positive acceleration peak. The profile in Figure 2-30 is not consistent with the expected profile, where the negative acceleration peak is far too low. There are two potential reasons: the mesh in the axial direction is too coarse, and the propellant is assumed to be linearly elastic. This is critical for the simulated firings since the shock wave introduced in the system is traveling axially, and the accuracy of the radial acceleration peaks is necessary for the burning rate component. Refining the mesh in the axial direction will provide a more accurate propellant acceleration profile, but will not necessarily change the steel acceleration profile drastically. The steel material is modeled as being linearly elastic, which is probably why the acceleration profile is the same as what is expected. Modeling the propellant as a nonlinear material may provide a more accurate acceleration profile, but for this study only the axial mesh refinement is considered.

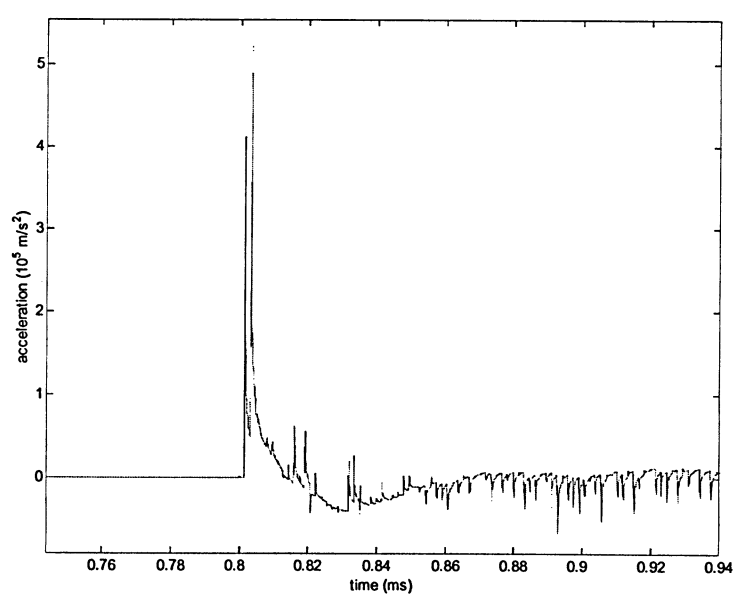

Figure 2-30 Applied shock wave: radial acceleration of propellant surface

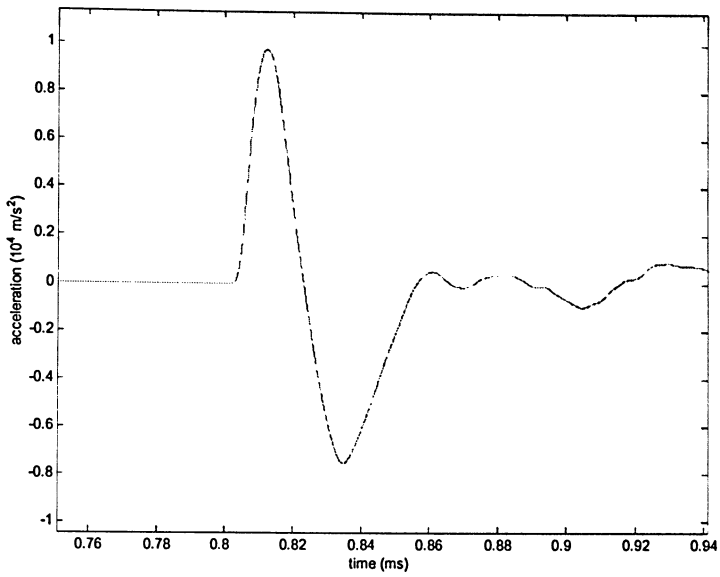

Figure 2-31 Applied shock wave: radial acceleration of steel sleeve surface

2.7 Propellant Regression Considerations

During an SRM firing, the propellant burns away or regresses over time due to the combustion process. This evidently changes the propellant structure, which in turn affects its mass, stiffness and damping properties, as well as affecting the port geometry required for the IBF component. As mentioned, it is assumed that the propellant only regresses during the quasi-steady portion of the simulation, while during the unsteady portion the structure does not change, but the regression is continued to keep the port area of the core flow accurate. As the propellant is regressing, the FE mesh is changed to adapt to the new structure geometry, which occurs by changing the node positions on the propellant inner boundary. This boundary is very significant because it is a common boundary to all three components of this study: structure, fluid and burning rate. The propellant regression algorithm will now be discussed in brief.

The local burn rate at any given location in the combustion chamber of the SRM and the time step size determines the amount of regression the propellant undergoes. Since in

this study only cylindrical grain motors are considered, the regression of the propellant is somewhat trivial. The algorithm, however, does have an option to regress general grain geometries (i.e., star-, wagon-wheel-, dog-bone-grain), but this discussion will be limited to cylindrical grain motors only. The IBF and burning rate components are one-dimensional in nature, thus the burn rate is given at various axial locations and is assumed constant around the periphery of any given axial location. The structured FE mesh simplifies this task, since nodes on the burning surface at the element edges all have the same axial position. This enables the axial variation of the burn rate to be applied to the FE mesh nodes on the burning surface with ease. An illustration of the FE burning surface mesh alignment with the IBF nodes is shown in Figure 2-32, where the x-direction is towards the nozzle-end, the IBF nodes are denoted by i-1, i, i+1, etc, and the propellant burning surface is shaded. The algorithm uses a linear interpolation technique to approximate the axial burn rate distribution from the IBF nodes to the FE axial locations. Note that for a cylindrical grain motor, all nodes along the periphery of one axial location have the same burn rate value.

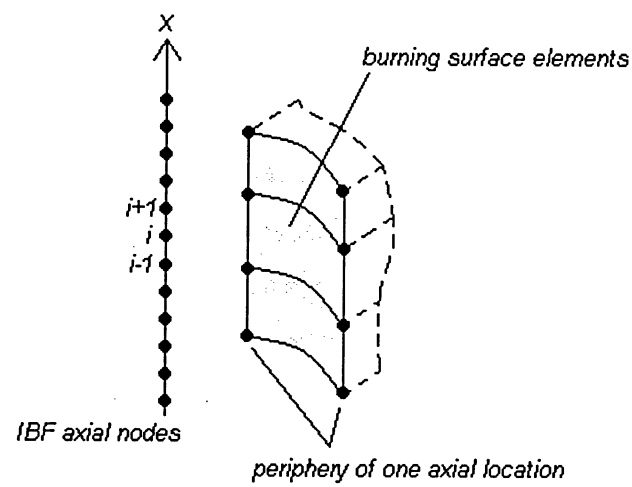

Figure 2-32 Burning surface elements and IBF nodes

The burn distance magnitude is then approximated by multiplying the corresponding axial location burn rate value with the time step size. The burn direction for a cylindrical grain motor is simply in the radial direction, which is normal to the burning surface. This gets complicated when analyzing general grain geometries, since the burn direction must be

normal to the burning surface. The mathematical relationship for the burn vector is given by the expression:

$$\vec{B} = r_b \Delta t \hat{n} \tag{2.95}$$

where $\hat{n}$ is the normal directional vector, r_b is the burn rate and Δt is the time step size. The burn vector is then applied to each FE node on the burning surface, and the elements in the FE mesh are physically regressed. As mentioned for a cylindrical grain, the nodes regress in the radial direction only, as shown in the two-dimensional schematic of Figure 2-33. This propellant burning algorithm is applied to all the FE mesh nodes on the burning surface, each time step. Thus, when the unsteady calculations begin, the propellant geometry is accurate and the FE component initial procedures are started with the current grain geometry.

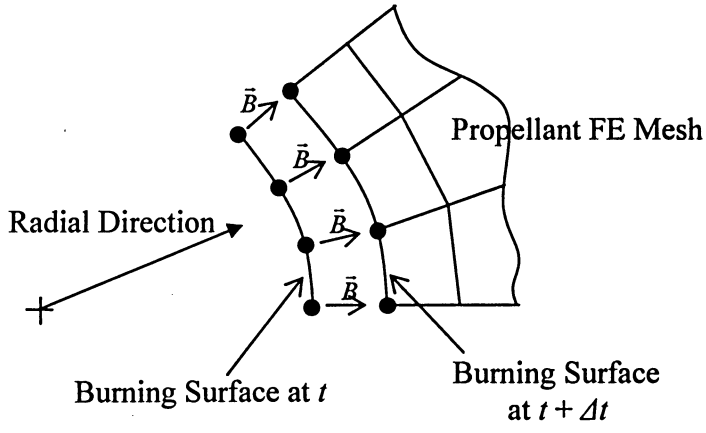

Figure 2-33 Propellant regression schematic

It seems evident that, at some point, the nodes on the burning surface may regress beyond the length of the elements, causing severe distortion or 'negative' element volumes. When this occurs, the algorithm has a node collapsing capability in which elements can be eliminated from the original mesh. This is a necessary step because having an element with 'zero' or 'negative' volume in the mesh will cause the Jacobian of Equation (2.27) to produce a determinant of zero or negative value, which will yield numerical errors in the solution.[15] Thus, the size of a mesh (i.e., number of elements and nodes) may reduce slightly due to regression, depending on how fine the original mesh is. Since only cylindrical grain motors

are the focus of the present study, any details are omitted because collapsing nodes is trivial in the radial direction. Note that using 8-node hexahedral elements are more attractive when it comes to regressing the FE mesh. This is due to the fact that the higher order 20-node hexahedral element has mid-side nodes, and when regressing the mesh, the position of the mid-side nodes must be respected. However, the algorithm is designed to regress both types of elements presented here. In either case caution must be taken in order to keep the FE mesh stable (i.e., the FE mesh solution must not contain any numerical errors), and to keep the structure geometry as close to the physical structure as possible.

Moreover, it was mentioned that the regression of the FE mesh is terminated at the end of the quasi-steady calculations. However, the regression of the propellant surface is continued throughout the remainder of the simulated motor firing. This is done to ensure that the control volume (i.e., motor chamber port area) of the flow domain is accurate throughout the simulation. The same algorithm described above is used for regression of the propellant surface, but the FE mesh is not altered any further. Details of the actual flow port area calculations are presented in Chapter 4.

As a final note on the FE structural component, the overall schematic of the structural FE component algorithm is included in Appendix A. Discussion of all the input and output data files required for the simulation are also discussed in Appendix A, with appropriate references to the flow chart schematic. The subsequent chapter discusses both the fluid (IBF) and combustion (burning rate) components of the simulation algorithm.

3 IBF and Burning Rate Components

3.1 Introduction

This chapter gives an overview of the IBF and burning rate components of the simulation model. The two components were previously employed by Greatrix and Harris[1] and later by Loncaric, Greatrix and Fawaz[10] in order to model the internal flow of an SRM. The IBF component is the computational fluid dynamics (CFD) portion which models the internal flow, while the burning rate component models the regression of the propellant due to pyrolysis via the combustion process. The governing equations for the flow portion will be presented, as well as the solution strategy used to solve the equations. The equations used in the burning rate algorithm and their solution will also be presented in this chapter, as they are vital to the IBF component. Finally, an overview of the IBF component and its typical operation will be discussed, as well as some key points regarding the analysis and simulation.

3.2 Flow Governing Equations

The flow equations employed by the IBF component are those typically used for a one-dimensional duct flow analysis, with some additional terms added to account for any mass, energy or momentum addition due to the burning of the propellant. The equations also include terms that represent a possible second particulate phase within the main flow, although the present study's results do not involve the use of a second particulate phase. These equations can be used for both steady and non-steady operation of SRMs. Also, since the studied SRMs all have large length-to-diameter (L/D) ratios, a one-dimensional analysis provides reasonable results.[25] The governing quasi-one-dimensional hydrodynamic continuity, momentum and energy equations for the flow are given by[1]

$$\frac{\partial \rho}{\partial t} + \frac{\partial (\rho u)}{\partial x} = -\frac{1}{A}\frac{\partial A}{\partial x}\rho u + (1-\alpha_p)\rho_s \frac{4r_b}{d} - \left(\frac{4r_b}{d} + \kappa\right)\rho \tag{3.1}$$

$$\frac{\partial (\rho u)}{\partial t} + \frac{\partial}{\partial x}(\rho u^2 + p) = -\frac{1}{A}\frac{\partial A}{\partial x}\rho u^2 - \left(\frac{4r_b}{d} + \kappa\right)\rho u - \rho a_l - \frac{\rho_p}{m_p} D \tag{3.2}$$

$$\frac{\partial(\rho E)}{\partial t}+\frac{\partial}{\partial x}(\rho uE+up)=-\frac{1}{A}\frac{\partial A}{\partial x}(\rho uE+up)-(\frac{4r_b}{d}+\kappa)\rho E$$

$$+(1-\alpha_p)\rho_s\frac{4r_b}{d}(C_pT_f+\frac{v_w^2}{2})-\rho ua_l-\frac{\rho_p}{m_p}(u_pD+Q) \tag{3.3}$$

General flow parameters include the gas phase density (ρ), axial flow velocity (u), pressure (p), local duct area (A) and hydraulic diameter (d) of the internal boundary, and total specific energy (E) which is given by $E=\frac{p}{(\gamma-1)\rho}+\frac{u^2}{2}$. There are also some particulate phase parameters in the equations such as mass fraction α_p, particulate density ρ_p, mass m_p, flow velocity u_p, drag force D and heat transfer Q. As mentioned, the particulate phase is not accounted for in this study, but the terms are left in the equations for completeness. Additional variables in the above three equations include the propellant density (ρ_s), local burn rate (r_b), longitudinal acceleration of the gas (a_l), gas heat capacity (C_p), flame temperature (T_f), mass injection velocity (v_w), and the port radial dilatation (κ). Radial dilatation caused by factors other than the propellant regression (i.e., structural vibrations) is assigned to $\kappa=\frac{1}{A}\frac{\partial A}{\partial t}$. The derivatives with respect to time (t) and axial spatial increment (x) are approximated using various techniques, which will be discussed subsequently. In this study, the spatial increments axial direction is from the head-end of the motor to the nozzle-end, as depicted in Figure 3-1.

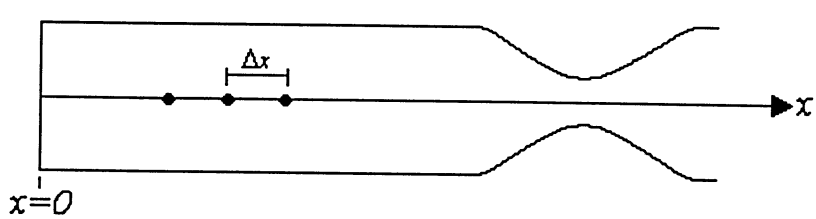

Figure 3-1 IBF component physical discretization

The port area, hydraulic diameter, radial dilatation, and longitudinal acceleration are all directly coupled to the structural FE algorithm. The calculation of these parameters is discussed in Chapter 4. Also, the local burn rate is directly coupled with the governing flow

equations and must be solved in conjunction with these equations, as will be discussed subsequently.

3.3 Flow Solver

Consider the present high speed compressible SRM internal flow, which is quasi-one-dimensional in nature. The solution algorithm utilizes a set of hydrodynamic conservation equations, as shown above, that govern the gas flow in the port of the SRM.[5] The algorithm uses a random choice method (RCM) to solve the conservation equations, which is an explicit finite-volume method of integrating hyperbolic sets of partial differential equations.[26] A typical characteristic of the RCM, differentiating it from other conventional finite-volume methods, is the use of a pseudo-random sampling of flow properties at given positions within the flow, in lieu of flow-averaging across an elemental section typically found in other methods. The purpose of this sampling is to reduce any numerical background noise during solution, which is prominent in this application due to the various inhomogeneous terms in the conservation equations, and due to the highly non-linear nature of the flow. From the three conservation expressions given by Equations (3.1) – (3.3), the inhomogeneous terms are those found on the right hand side of the equations, where the left hand side consists of the homogeneous terms typically seen in constant area duct flow problems.

The RCM essentially marches in space at a given time step, starting from the head-end of the motor to the nozzle exit, solving the flow equations and determining the local flow parameters in conjunction with the local burn rate. A random position is selected in between two neighbouring nodes at the beginning of a time step, where flow property gradients ($d\rho$, du, dp) are established from the two nodes at the random position using quasi-steady flow equations (i.e., Equations (3.1)-(3.3) with time derivatives set to zero). Under the non-steady transient conditions encountered in this study, this will likely produce a discontinuity in the flow at the random position. This will in turn produce wave motion causing the quasi-steady equations to produce a choked flow condition before reaching the random position.

At this time, a higher-order planar Riemann approach[1] is used to solve any wave motion resulting from the discontinuity, and the flow properties are found at the mid-point between the neighbouring nodes at the end of the first half-time step. Since the flow properties are found at mid-point positions between the nodes (i.e., $\Delta x/2$), caution is needed to maintain accuracy with the flow properties to minimize any numerical noise in the solution. The node spacing is depicted below in Figure 3-2.

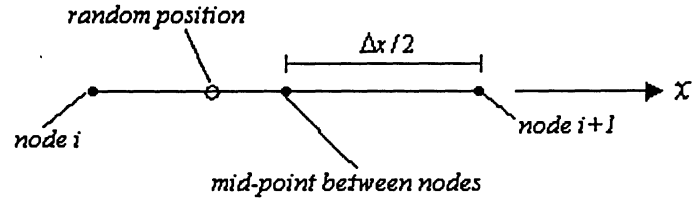

Figure 3-2 IBF solver node spacing considerations

Next, the inhomogeneous source terms of the conservation equations are implemented into the planar wave solution using a second-order method described by Ben-Artzi and Falcovitz.[27] This method causes the wave solution to reach second-order accuracy as the time step becomes small. The inhomogeneous source terms (due to grain and nozzle area transition and propellant gas influx) that contribute substantially to artificial noise development are implemented using this method. The remaining inhomogeneous terms due to factors such as axial acceleration and radial dilatation (i.e., structural oscillations) do not contribute substantially to noise development, and are incorporated into the Riemann solution through an operator time-splitting technique.[28] Details of these presented numerical methods have been omitted from the report; they can be obtained from the literature.

The time derivatives in the conservation equations are calculated using a weak-wave Eulerian scheme. This simplifies the solution since dealing with left and right-running characteristic waves is simpler than dealing with the rarefaction wave and shock wave used in the Riemann solution.[29] Thus, with the inclusion of inhomogeneous terms, flow conditions are matched through the weak waves from left to right and a contact surface allows for the calculation of the time derivatives arising from the random position of the RCM, found at the beginning of the time step. The influence of time derivatives within the

inhomogeneous terms will occur over a shorter time span (Δt_{eff}), rather than the full time step (Δt). Thus, the corrected flow properties are found using the expression

$$\lambda^* = \lambda_0^* + \Delta t_{eff}(\frac{\partial \lambda}{\partial t})_0 \tag{3.4}$$

where λ is a flow property, λ_o^* is the solution to the Riemann problem at the mid-point, the time derivative is evaluated at the random position at the beginning of the time step, and λ^* is the corrected value for the flow property. Now, λ^* must be modified for the background quasi-steady flow changes from the random position to the mid-node position as done initially. The corrected flow properties at the axial mid-node positions at the end of the first half-time step are now solved.

This same process is repeated for a second half-time step, which will then reposition the axial nodes to their original positions, and determine the corrected flow properties at the end of the second half-time step. The FE module must run in-between each half-time step in order to provide the necessary structural input to the IBF solver. Also, the burn rate calculations are run each half-time step in order to provide the local burn rate values at the axial nodes, which are required within the flow solution algorithm. This is discussed in the subsequent section.

3.4 Burning Rate Equations

The burn rate algorithm for the SRM propellant is an implicit part of the flow calculations. In this study, a quasi-steady rapid kinetic rate burning model is employed, which does as a result ignore transient combustion effects.[1] The burn rate algorithm consists of three components that influence the overall propellant surface burn rate (r_b): pressure-induced burning, velocity-induced (or erosive) burning and acceleration-induced burning. The main equations for the three components are presented, along with the non-linear solution approach.

Pressure-induced burning follows the empirical law of de St. Robert, which is:[4]

$$r_p = Cp^n \tag{3.5}$$

where r_p is the pressure-induced burn rate, p is the local pressure (in kPa), n is the empirical pressure exponent, and C is the burn rate coefficient. This coefficient can be found experimentally, and is a function of the propellant's initial temperature (T_i), as shown in the formulation

$$C = C_0 \exp\left(\sigma_p \left(T_i - T_{io}\right)\right) \tag{3.6}$$

where C_o and T_{io} are found at reference conditions, and σ_p is the pressure-dependent burn rate temperature sensitivity. Both C_o and n can be found through experimental SRM firings at various pressures.

Erosive burning in this study is mainly governed by local convective heat transfer at the propellant burning surface. When the heat flux into the propellant surface is increased, there is a corresponding increase in the local burn rate. The following model is used in this study and has proven to be reasonably good for various composite and homogeneous propellants.[1] The equations used in the algorithm for erosive burning are

$$r_b = r_0 + \frac{h\left(T_f - T_s\right)}{\rho_s\left[C_s\left(T_s - T_i\right) - \Delta H_s\right]} \tag{3.7}$$

where r_o is the base burning rate component including any pressure and acceleration effects, r_b is the overall burn rate, T_s is the propellant surface temperature, C_s is the propellant specific heat capacity, ΔH_s is the propellant surface heat of reaction, and the convective heat transfer coefficient (h) is given by

$$h = \frac{\rho_s r_b C_p}{\exp\left(\dfrac{\rho_s r_b C_p}{h^*}\right) - 1} \tag{3.8}$$

Here, C_p is the core flow gas specific heat and the zero-transpiration heat transfer coefficient (h^*) is found via

$$h^* = \frac{k}{d} \mathrm{Re}_d \, \mathrm{Pr}^{1/3} \frac{f}{8} \tag{3.9}$$

where the Reynolds number based on the hydraulic diameter and flow properties is given by $\mathrm{Re}_d = \rho u d / \mu$, the Prandtl number is given by $\mathrm{Pr} = \mu C_p / k$, k is the gas thermal conductivity, and the Darcy-Weisbach friction factor (f) is given by

$$f^{-1/2} = -2\log_{10}\left(\frac{2.51}{\sqrt{f}\,\mathrm{Re}_d} + \frac{\varepsilon/d}{3.7}\right) \tag{3.10}$$

The effective propellant surface roughness (ε) is estimated for a particular propellant. This erosive burning model proves to work well with large L/D SRMs, where the flow becomes fully developed, as one moves to the aft end of the motor.[25]

Acceleration-induced burning can be a significant factor in the augmentation of local burning rates. This is of primary importance for the current study since structural oscillations and accelerations will contribute to the overall burn rate during simulated motor firings. As discussed by Sutton and Biblarz,[4] propellant surface acceleration can be appreciable in augmenting the local burn rate if the resultant acceleration vector is within about 20° from the normal direction. This is depicted in Figure 3-3, which shows two views of the acceleration vectors.

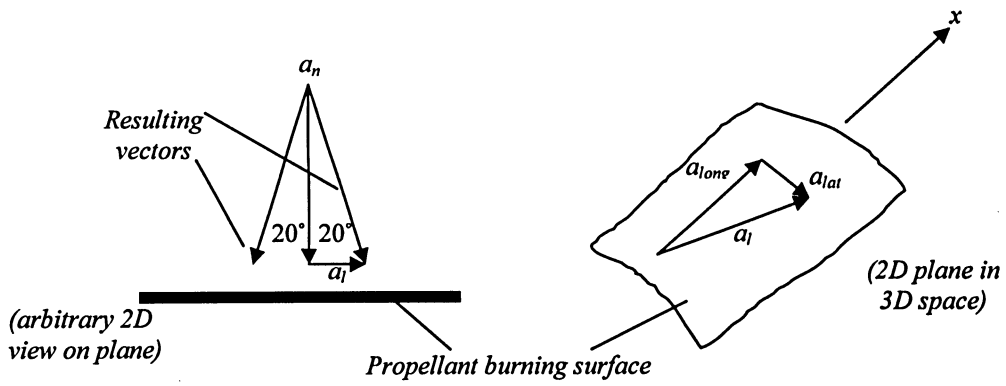

Figure 3-3 Acceleration vectors on propellant burning surface (2-D and 3-D)

For this study, the acceleration-induced burn rate is based on a phenomenological model, which combines normal, lateral, and longitudinal acceleration effects.[8] The acceleration-induced burning model is defined by

$$r_b = \frac{C_p\left(T_f - T_s\right)}{C_s\left(T_s - T_i\right) - \Delta H_s} \frac{r_b + G_a/\rho_s}{\exp\left[\dfrac{C_p\delta_0\left(\rho_s r_b + G_a\right)}{k}\right] - 1} \tag{3.11}$$

where δ_o is the reference energy film thickness and G_a is the accelerative mass flux, both given by

$$\delta_0 = \frac{k}{\rho_s r_0 C_p} \ln\left(1 + \frac{C_p\left(T_f - T_s\right)}{C_s\left(T_s - T_i\right) - \Delta H_s}\right) \tag{3.12}$$

$$G_a = \left(\frac{a_n p}{r_b}\frac{\delta_0}{RT_f}\frac{r_0}{r_b}\right)\cos^2\phi_d \tag{3.13}$$

Here, r_o is the base burning rate component including any pressure and erosive burning effects, and a_n is the normal acceleration acting at the propellant surface. The accelerative mass flux given above is general for combined normal, lateral and longitudinal acceleration effects, however if the displacement angle (ϕ_d) is set to zero, G_a would only account for normal acceleration effects. The displacement angle is given by

$$\phi_d = \tan^{-1}\left[K\left(\frac{r_0}{r_b}\right)^3 \frac{a_l}{a_n}\right] \tag{3.14}$$

where a_l is the vector sum of the lateral and longitudinal acceleration components, and K is an empirical orientation correction factor equal to 8 for this study.[8] The displacement angle is essentially an augmented orientation angle used in the burning model, but the normal orientation angle (ϕ) is given by

$$\phi = \tan^{-1}\left(\frac{a_l}{a_n}\right) \tag{3.15}$$

This can be seen in Figure 3-4, where the resultant acceleration vector and the normal direction produce the orientation angle.

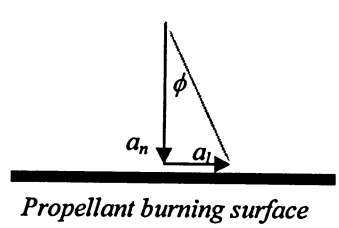

Figure 3-4 Acceleration orientation angle

Note that the normal acceleration of the propellant surface structure a_n is assumed negative in value when directed into the core flow, and, from experimental data,[1] it is set to zero when the acceleration is positive or directed away from the core flow. In other words, normal acceleration augments the burning rate only when the combustion layer is being compressed, and normal acceleration of the propellant structure away from the combustion zone has negligible effects on the burning rate. Lateral and longitudinal acceleration are sign independent and generally reduce the amount of burning augmentation caused by the normal acceleration, since the orientation angle increases with increasing a_l.

Based on the presented burn rate model, it is evident that there exists a non-linearity between the erosive burning and acceleration-induced burning equations. This is evident from the base burning rate variable (r_o) present in both the erosive burning and acceleration-induced burning equations. Recall that the base burning is a combination of the other two component burning effects in the burn model, thus a unique non-linear solution is required to converge to the overall burn rate (r_b) by solving Equations (3.7) - (3.14) iteratively. The solution methodology is detailed in the subsequent section.

3.5 Burning Rate Solution Methodology

The first step in the burn rate solution is to determine the pressure-induced burn rate from Equation (3.5), as it has no dependence on velocity or acceleration effects. Using the pressure dependent burn rate as the base burn rate with zero acceleration effects, the erosive calculations are then performed (Equations (3.7)-(3.10)). These equations are non-linear; thus, a Newton-Raphson numerical method is used to solve for r_b. Details of the Newton-Raphson non-linear solution method can be found in the literature.[30]

Once the erosive solution has converged to some specified degree of accuracy, the normal acceleration component of the burn rate is solved. This is only done if the normal acceleration component is negative (i.e., propellant structure moving into the core flow). Here, Equations (3.11)-(3.14) are solved for r_b also using the Newton-Raphson non-linear method. At this point, the displacement angle is set to zero in Equation (3.13), and the base

burn rate includes the pressure and erosive burning rate components. The solution is iterated until a specified degree of accuracy is reached. It is possible that the solution will not converge because the base burn rate in the erosive burn rate solution did not include any acceleration effects. Thus, if the solution does not converge, the erosive burning calculations are re-entered using the sum of the pressure-induced burn rate and the current acceleration-induced burn rate value as the base burn rate. This iteration through the erosive burn rate and acceleration-induced burn rate is repeated until overall convergence is reached.

At this point, the burn rate due to pressure, erosive burning, and normal acceleration is known and the effects of the lateral and longitudinal components of acceleration can be added. Adding these factors in from the beginning of the solution can cause severe convergence difficulties, which is the reason they are added at this point. Also, since the lateral and longitudinal acceleration components only correct for geometry, they are easily implemented hereafter. The acceleration-induced burn rate equations are reiterated with the displacement angle included using the Newton-Raphson method, until convergence is met. This is the final burn rate r_b value, which is then used within the flow calculations.

An overall schematic of the burn rate algorithm is shown in Figure 3-5. This process is repeated for every section along the axial direction of the motor, and may be repeated around the periphery at one specific section if there exists a variation in acceleration components along the boundary of the propellant surface. Note that the assumption of a rapid, quasi-steady response for the local burn rate is necessary (versus a transient burning rate model) to isolate the effects of the motor structural vibrations as an instability driving mechanism. The inclusion of a transient burning rate model would render unclear the effects of the structural acceleration field.[1]

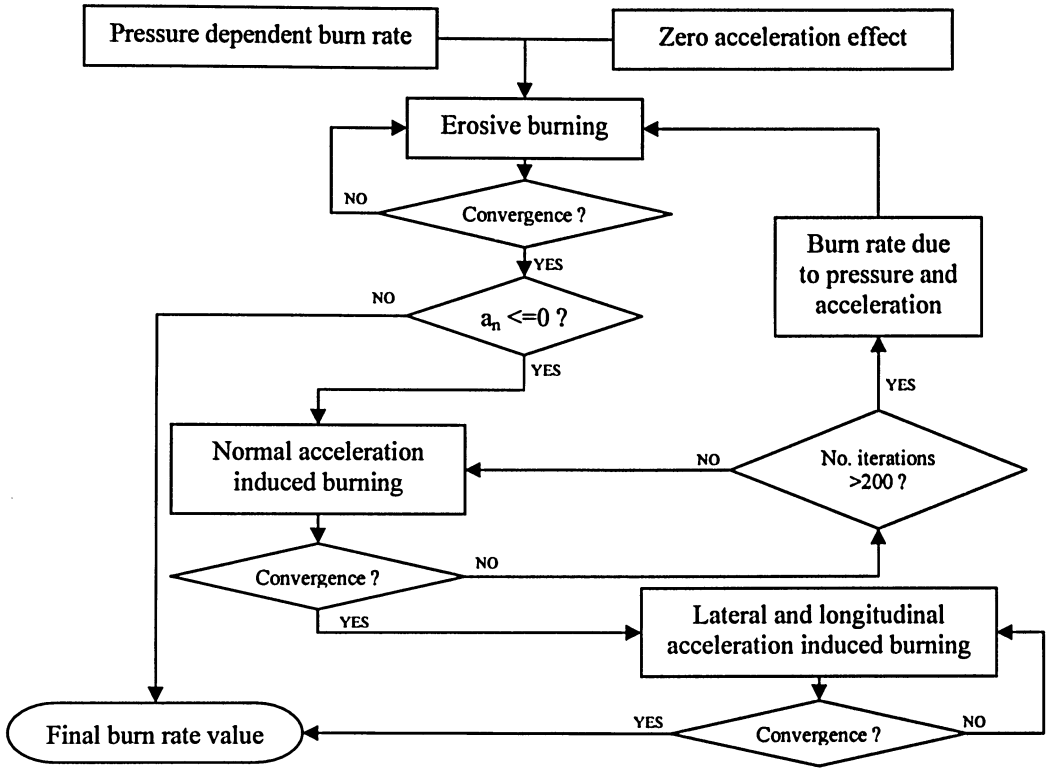

Figure 3-5 Burning rate algorithm solution schematic

3.6 IBF Component Simulation Overview and Considerations

Both the flow and burn rate equations and solution methods were presented; thus, the IBF simulation will now be discussed with emphasis on factors that influence the FE component of the overall SRM firing simulation. Characteristics of the algorithm such as the time step calculation, steady-state and unsteady calculations will be presented in the subsequent paragraphs.

The overall IBF algorithm discussed is designed to function in both quasi-steady and unsteady motor operation. A typical simulation for this study consists of quasi-steady calculations up to a predetermined time, then a switch to the unsteady calculations from that time on. Quasi-steady calculations consist of modeling the internal flow using Equations (3.1) - (3.3) with time derivatives set to zero, and using the presented burn rate calculations without any acceleration effects. Conversely, the unsteady calculations consist of using

Equations (3.1) – (3.3) as presented above with the RCM as the flow solver, and the full burn rate calculations also presented above. The idea is to run the quasi-steady calculations up to a time before the disturbance is introduced and begin the unsteady calculations, giving the necessary time for the unsteady flow to settle to an equilibrium position before the time the disturbance is introduced. This potentially minimizes any numerical noise before the disturbance is introduced, allowing for increased accuracy for the duration of the simulated firing. The intention is also to reduce the computation time by using the quasi-steady calculations up to a certain point. This switch from quasi-steady to unsteady flow is shown in the flow chart of Figure 3-6. With respect to the FE component, during the quasi-steady calculations there is no structural motion because any time derivatives are set to zero. Thus, the FE component is initialized upon commencement of the unsteady flow calculations, where the structural transients are needed.

Another key factor in the IBF algorithm is the calculation and use of the time step. For the initial quasi-steady calculations the time step size does not affect the solution; thus, a predetermined time step is used for all quasi-steady iterations. For the unsteady calculations, this is not the case, as there is a conditional stability requirement for the time step due to the explicit solver used for the solution of the flow equations. The maximum allowable time step for the unsteady IBF solution is based on the speed at which information travels through the medium. For general fluid mechanics, and for this study, this is based on the wave speed (c) defined as $c = a + u$, where a is the speed of sound and u is the velocity of the fluid. Thus, based on the wave speed, the CFL condition (as discussed in Section 2.5.3) can be used to estimate the full time step (Δt) constraint as follows[15]

$$\Delta t \leq C_n \frac{\Delta l}{c} \tag{3.16}$$

where $C_n \leq 1$. This calculated time step is actually divided in half, due to the two half-time steps required for the RCM solution (see Section 3.3). Here, C_n is the Courant number, which is a numerical constant used to scale down the time step below the maximum allowable limit in order to assure numerical stability, and Δl is the grid spacing or the distance between nodes in this one-dimensional flow study. Thus, using the equal sign in Equation (3.16) would suggest the maximum allowable time step be used, and this time step

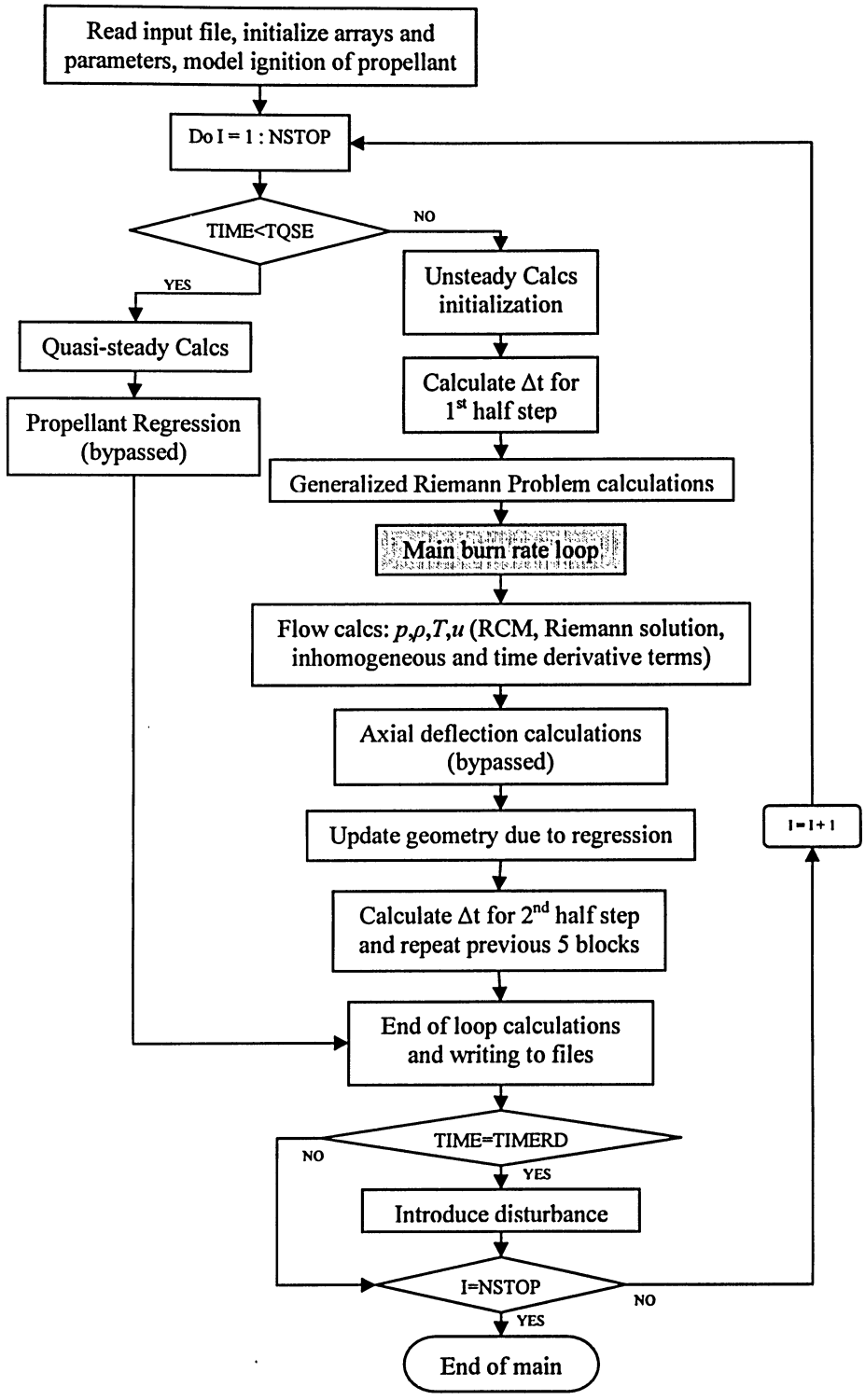

Figure 3-6 IBF and burning rate algorithm solution schematic

would represent the time it takes a wave with speed (c) to propagate a distance Δl. The physical interpretation of the CFL condition is that the time step must be small enough so that information does not travel through more than one element or grid spacing (Δl) in one time step (Δt).[15] This insures that the flow transients are captured accurately over time and that numerical stability is maintained during the entire simulation. For the current study, the wave speed is taken at the node with the highest velocity (u) and the IBF Courant number is set to 0.5 (for each half-time step) for all simulations. This calculated time step, based on fluid mechanics, will have an influence on the accuracy of the FE component of the simulation.

Other important characteristics of the IBF algorithm include the original analytical structural vibrations routines (both radial and axial) and the propellant regression routines that are intrinsic to the algorithm. For the purposes of this study, these routines are all bypassed during the simulations because the new three-dimensional FE component accounts for all applicable structural vibrations. The propellant regression routines are also bypassed since the regression is monitored by the fluid-structure interaction subroutines running 'in-between' the two main components. This is further discussed subsequently in Chapter 4. It should be noted that the IBF algorithm is capable of simulating any propellant geometry, for example cylindrical-, star-, and wagon-wheel-grain. This enables compatibility between the IBF algorithm and the general three-dimensional FE algorithm, regardless of the grain geometry used.

Of final note regarding the IBF component is the disturbance routine, which is also intrinsic to the algorithm. As mentioned before, during a typical SRM combustion instability simulation, a disturbance is introduced at a predetermined time within the motor port in order to investigate the effects of this disturbance on the local flow and burn rate. The IBF algorithm has the capability of introducing two main types of disturbances, the first being a traveling shock wave with a compression front and an expansion tail, and the second a step overpressure disturbance in the main chamber. For the purposes of this study, the first disturbance is used during simulated firings. The implementation of the disturbance routine within the overall IBF algorithm is shown schematically in Figure 3-6. Note the main burn

rate loop previously introduced is the shaded block in Figure 3-6. The travelling axial shock wave in the chamber of a cylindrical grain motor is shown schematically in Figure 3-7.

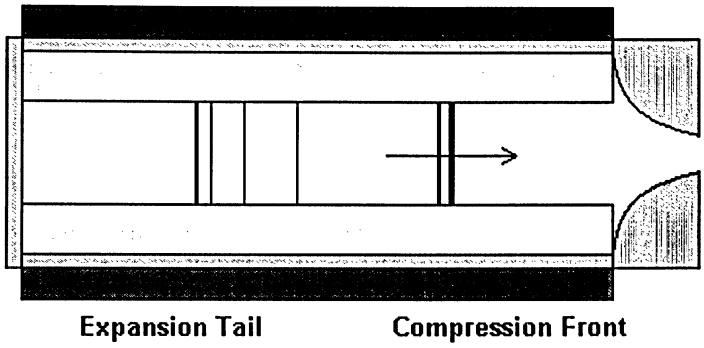

Figure 3-7 Travelling axial shock wave schematic

The travelling disturbance routine in the IBF algorithm is designed to simply apply a variation of pressure, velocity and temperature in the motor chamber at the specific locations of the compression front and the expansion tail of the disturbance. Three types of traveling axial disturbances are available and will be presented here. Consider the original traveling disturbance pressure profile shown in Figure 3-8, where the shock strength is denoted as Δp (i.e., the total pressure of the disturbance is $p + \Delta p$, where p is the local chamber pressure before the disturbance is introduced). The chamber pressure variation in the axial direction before the disturbance is introduced is illustrated by the linear plot before the expansion tail and after the compression front, and the dashed line in between. The expansion tail and compression front regions are quite short in the axial direction, where the local pressure values are ramped from the local pressure before the disturbance is introduced to the new pressure ($p + \Delta p$). The local velocity and thus the temperature are also ramped as is the pressure. In the region between the compression front and expansion tail, the local pressures are all greater than the local flow values before the disturbance is introduced by the shock strength Δp. The local velocity and temperature values in this region are analogous to the local pressure values. The other two types of axial traveling disturbances are a gradual isentropic wave and a shock-fronted wave, both of which are modifications to the presented original disturbance. For both modifications, the algorithm is updated to have an interpolated pressure and velocity from the local chamber pressure, p to $p + \Delta p$ in the expansion tail and

compression front, and a constant velocity wave center with characteristic pressure to match in the region between the expansion tail and compression front. The strength of the disturbance is maintained, but the location of the regions in the disturbance is changed in order to reduce any artificial motion on the structure typically caused when the disturbance is first introduced into the flow. The gradual isentropic wave has a much larger expansion tail and compression front region, with a smaller region in between. The shock-fronted wave has a similar expansion tail region to the isentropic wave and a similar compression front region to the original wave, with a slightly smaller region in between. Results for different disturbances are presented in Chapter 5, while the next chapter details the coupling of the simulation components.

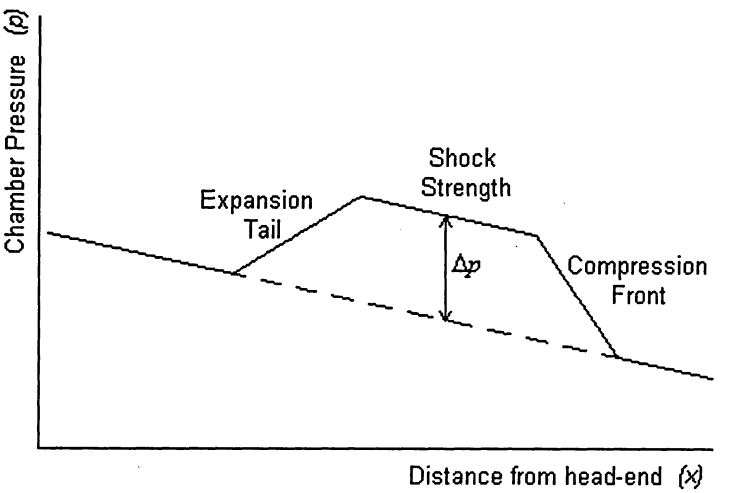

Figure 3-8 Disturbance routine schematic

4 Fluid-Structure Theory and Component Integration

4.1 Introduction

The different simulation components relevant to this study have been presented, where the integration of these components in a fluid-structure context will now be discussed. Generally, FSI simulations can be modeled using frequency domain techniques where linearized equations are used, and a linear relationship between the flow properties and structural deformations are assumed. Once nonlinear effects such as flow vibration shocks (as in this study) or structural property nonlinearities exist, time domain methods are necessary for the simulation.[31] Typically, for this case, the fluid and structural equations are solved separately, since nonlinearities in either the flow or structural components can cause serious convergence issues otherwise. There are two ways to solve a fluid-structure interaction type problem, via a monolithical or coupled field approach.[31] The monolithical approach is used when the fluid and structural components are integrated as a single system, and are solved simultaneously. The coupled field approach couples separate structural and fluid solvers through various algorithms, as modeled in the time domain discussed above. The components presented here are solved individually, and thus the simulation is modeled in the time domain. Thus, the interface between the fluid and the structure is where the influence from each separate component and the coupling takes place. Essentially, the fluid flow is modeled as a load boundary condition for the structure, and the structure deformation and/or transient response is accounted for in the fluid model, as is the case in this study. Also, the numerical techniques used in the structural and fluid components are typically not the same, thus when coupling the two algorithms, it must be ensured that proper information is passed, simulation time is consistent, and accuracy is maintained in order to yield a feasible simulation.

Since accuracy is a top priority for the simulation, the coupling of the structural and fluid components must be accompanied by an adaptive mesh algorithm, as discussed in various literature.[10, 31] The adaptive mesh algorithm is necessary in order to update the

discretized fluid and/or structure domain. The time dependence of the adaptive mesh is the same as that for the simulation; thus, the mesh must be updated every iteration. For an application such as an SRM, both the structural and fluid domains change at every time step. Due to the propellant regression the structure mesh changes as the simulation proceeds in time, also since the structure is vibrating the port area for the fluid changes over time. This requires an algorithm to account for the change in port area for the CFD code, and for the change in the structural mesh for the FE code. Moreover, the kinematical compatibility at the fluid-structure boundary must be maintained while the geometry of the domains is updated. This is ensured by respecting mass conservation laws of the coupled system, which acts as a continuous medium sticking together due to the kinematical compatibility constraint.[31]

In conclusion, the coupling procedure for the CFD and FE components of a simulation sets wall boundary conditions for the flow and right hand side force terms for the FE equations, while maintaining time accuracy and numerical stability. Again, conservation of energy must be ensured over time to avoid any numerical problems and in order to run an accurate simulation.

4.2 Present Simulation Components

Coupled structural and fluid components having an interfacing boundary is typical for all FSI applications. The SRM in this study slightly differs from a typical fluid-structure interaction problem, since a third component, the burning rate algorithm, is added to the simulation. This component directly affects the fluid-structure interface, imposing two main additional considerations: the structure (i.e., the propellant) regresses with time, and the acceleration of the structural boundary directly impacts the burning rate. Thus, the simulation consists of three main components, including the IBF algorithm, the burning rate algorithm, and the structural algorithm. An algorithm that controls the overall simulation itself, as well as the information passed between the three components in the simulation is also included. For this study, the IBF algorithm and the burning rate algorithm are

incorporated together, which was discussed in Chapter 3 and previously utilized by Greatrix.[1,5] The structural algorithm was created using the FE numerical method as discussed in Chapter 2, and is independent of the IBF code. Finally, for lack of a better term, the algorithm purposed to control the simulation will be named the FSI interface. The FSI interface algorithm controls the variables passed between the IBF, burning rate and FE components, ensures proper time increments for the simulation, governs the adaptive mesh for the FE component, and controls any simulation data output necessary. This ensures an accurate simulation as discussed above; a typical simulation procedure will be described in Section 4.3.

The typical data transferred between the IBF and FE components is the pressure distribution from the fluid component to the structure component, and an update of the dynamic fluid-structure boundary common to the two components from the structural component to the fluid component. In addition for this study, the fluid-structure boundary acceleration values are required for the burning rate component, and the calculated burn rate values are required for both the IBF and FE components. The complete coupled components and the FSI interface are schematically shown in Figure 4-1.

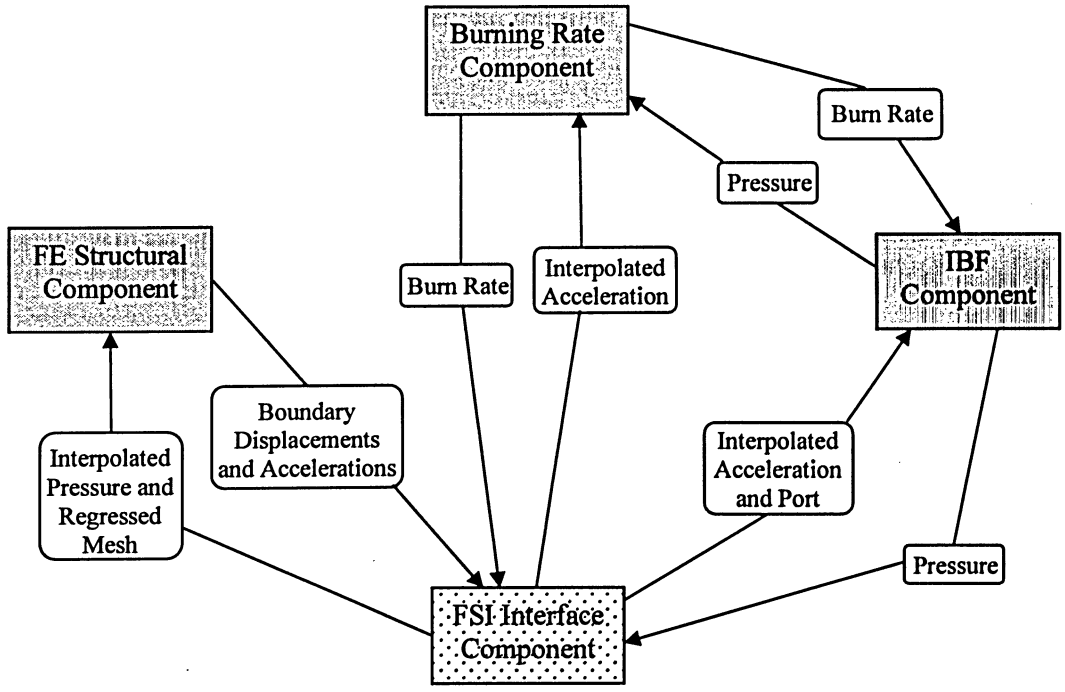

Figure 4-1 Coupled component schematic

Note that the three components interact with one another indirectly through the FSI interface component, except for the IBF and burning rate components. Typically, these two components would also interact through the FSI interface; however, due to the identical spatial increments used in both components, the variables between the two are passed directly. As illustrated, the FSI interface component couples all three simulation components. The propellant inner surface is the physical interface boundary between the three components, and all parameters being passed in Figure 4-1 are affected by or located on the propellant inner surface. The accuracy of the parameters on this surface is important for accuracy in the highly coupled simulation, thus significant attention is dedicated to the interpolation and application of parameters from one component to the next. This is discussed subsequently, along with the overall simulation schematic.

4.3 Simulation Schematic and Considerations

The detail of the parameters passed between each component, and the calculation of these parameters will now be discussed. The overall time domain modeled simulation schematic will also be shown, with the inclusion of all three simulation components mentioned previously. As mentioned, the parameters affecting the three components are all located on or influenced by the inner propellant surface boundary. Thus, the spatial discretization of each component along the common boundary must be considered. The IBF and burning rate components share the same one-dimensional nodal discretization in the axial direction of the cylindrical SRM, while the three-dimensional FE component mesh evidently differs from the other two components. Shown in Figure 4-2 is a two-dimensional schematic of the typical IBF/burning rate and FE mesh alignments. Since the IBF component is one-dimensional, the axial mesh direction of the FE component only needs to be considered for passing any appropriate variables. Generally, for this study, the FE mesh discretization in the motor axial direction is not as fine as the IBF axial mesh, due to the economical limitations on the refinement of the FE mesh. The nodes for each component are spaced by even intervals in the motor axial direction, and are denoted by Δx_{IBF} and Δx_{FE} for the IBF and FE

components, respectively. The IBF and burning rate component nodes are denoted by $i-1$, i, $i+1$, while the FE component nodes are denoted by $j-1$, j, $j+1$, as shown in Figure 4-2.

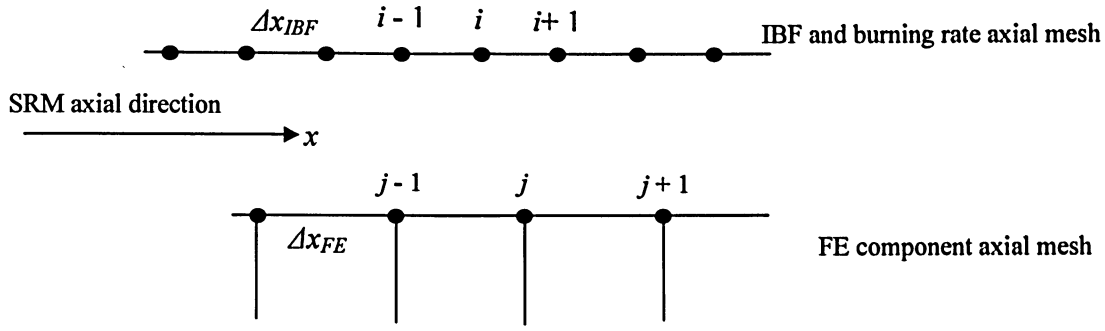

Figure 4-2 Simulation components mesh alignment

In this study, a linear interpolation in the motor axial direction between the corresponding component nodes is used to pass the appropriate parameters from one component to the next. For example, if FE structural properties at nodes $j-1$, j, and $j+1$ are known and need to be passed to the IBF component for its solution, then the structural properties at the IBF nodes $i-2$, $i-1$, i, $i+1$, $i+2$, $i+3$ will be influenced by these structural nodes. Thus, to find the arbitrary structural property (χ) at IBF node i, the structural property at nodes $j-1$ and j must be used to linearly interpolate the value for node i. Furthermore, to find the arbitrary flow property (λ) at FE axial node j, the flow property at nodes i and $i+1$ must be used for linear interpolation. These examples are represented mathematically in the following two expressions, with the distance x measured from the motor head-end.

$$\chi_i = \chi_{j-1} - \frac{x_i - x_{j-1}}{\Delta x_{FE}}\left(\chi_{j-1} - \chi_j\right) \tag{4.1a}$$

$$\lambda_j = \lambda_i - \frac{x_j - x_i}{\Delta x_{IBF}}\left(\lambda_i - \lambda_{i+1}\right) \tag{4.1b}$$

Note that if the grain geometry is not cylindrical (i.e., star grain or wagon wheel grain), the interpolation presented must also be applied in the tangential direction, around the periphery of each axial node location. The current study focuses on cylindrical grain motors only, thus any detail for non-cylindrical grain motors is omitted here. Equations (4.1a) and (4.1b) are

used by the FSI interface component to interpolate any input values from one component to the necessary output values used for another component, as was shown in Figure 4-1.

Specifically, Equation (4.1a) is used when the structural radial displacements, radial accelerations and longitudinal accelerations of the propellant inner surface are passed to the IBF and burning rate components. The radial and longitudinal acceleration values are needed to calculate the overall local burn rate values in the burning rate component, as discussed in Section 3.4. The FE mesh acceleration output is given in the global Cartesian coordinate system, but for the case of a cylindrical-grain motor the radial acceleration is needed. This is easily obtained by using the x and y acceleration components, which are both normal to the motor axis (z axis for the FE mesh, or x axis for the IBF mesh). The longitudinal acceleration is already given in the axial direction of the motor, thus no special treatment is required. The longitudinal acceleration is also needed by the IBF component to solve Equations (3.2) and (3.3), which is denoted by a_l. The radial displacements of the propellant inner surface are needed to calculate the port hydraulic diameter, port area and radial dilatation in the IBF equations. The radial displacements can be found in a similar manner to the radial acceleration mentioned above. The propellant burn rate is also required to determine the three aforementioned parameters in the IBF equations. Thus, the sum of twice the burn vector magnitude given by Equation (2.95) and twice the change in radial displacement yields the updated local port diameter change for a cylindrical grain motor. This is given mathematically by Equation (4.2), where the updated local port diameter is given by $d_{t+\Delta t} = d_t + \Delta d$.

$$\Delta d = 2\left(\Delta t r_b + \Delta u_r\right) \tag{4.2}$$

The time step used is the simulation time step, and Δu_r is the local radial displacement change over a given time step (note, the previous time step diameter is given by d_t). The port area is easily found using the port diameter, and the port radial dilatation κ is then found using the change in port area over time, as discussed in Section 3.2.

Also, Equation (4.1b) is used when the pressure from the IBF component is passed to the FE component and the burn rate values from the burning rate component are required for the FE mesh regression. As mentioned, the IBF pressure values are applied as external loads

on the FE structure propellant inner surface. It should be noted that the flow solution presented in Section 3.3 divides the simulation time step into two half steps, where the IBF nodes are shifted the first half-step. This shifting of nodes is accounted for when the pressure interpolation is calculated; thus, the alignment of the IBF grid shown in Figure 4-2 is shifted towards the nozzle-end of the motor by $\Delta x_{IBF}/2$. Once the IBF pressure values are interpolated to the FE axial mesh nodes, the pressure loads are not directly applied to the FE structure mesh. The reason for this is that the solution to the local flow pressure values by the explicit finite-volumé RCM discussed in Section 3.3 is split into two half-time steps as already mentioned. What this does is cause some minor oscillations in the pressure values at any one axial location over time, which may cause some numerical noise in the flow solution and be amplified in the structural solution. The pressure interpolation yields the pressure at the FE mesh axial nodes (i.e., interpolates in space), but the interpolation of pressure at any axial location over time is also necessary to smooth out the pressure oscillations over time. If this time interpolation is ignored, the FE structure will produce large amounts of numerical noise, causing the simulation to diverge. Note that the spatial interpolated pressure values (p_{FE}) are interpolated over time, not the actual pressure values (p) calculated by the IBF component.

One way to reduce the effects of these oscillations on the FE structure is to average the current interpolated pressure value with the interpolated value from the previous time step, such that

$$p_{FE_{avg}} = \frac{p_{FE}^{t} + p_{FE}^{t-\Delta t}}{2} \tag{4.3}$$

The superscripts on the interpolated pressure values denote the current (t) and previous (t-Δt) time steps. The affect this has on the interpolated pressure values at any axial location is shown in Figure 4-3, where the interpolated pressure values at the head-end of the motor are plotted along with the averaged values using Equation (4.3). The bold plot is the averaged pressure values over time, which evidently smoothes out the oscillations in the pressure. The oscillations produced by the pressure (p) in the IBF code are similar to the oscillations shown in Figure 4-3 for the interpolated pressure (p_{FE}). Although the averaged pressure values do reduce the pressure oscillations significantly, the plot reveals that every few iterations, the

pressure suddenly increases or decreases like a step function. This has no affect on the IBF or burn rate components as it is intrinsic to the solver; however, this will definitely affect the FE solver causing numerical noise in the solution. In order to reduce this noise, an attempt is made to smooth out the averaged pressure values of Equation (4.3). An algorithm is introduced to lag the pressure from the beginning of the step to the end and entails a linear interpolation of the pressure between the IBF half-time steps. The equation used to lag the pressure is given by:

$$p^{t}_{FE_{lag}} = p^{t-\Delta t}_{FE_{lag}} + \frac{p_{FE_{avg}} - p^{t-\Delta t}_{FE_{lag}}}{C_{lag}} \tag{4.4}$$

where the superscripts for the lagged pressure denote the current (t) and previous (t-Δt) time steps, and C_{lag} is a lag factor. The lag factor controls the amount of pressure lag desired, which should not be excessive in order to maintain the correct pressure profile.

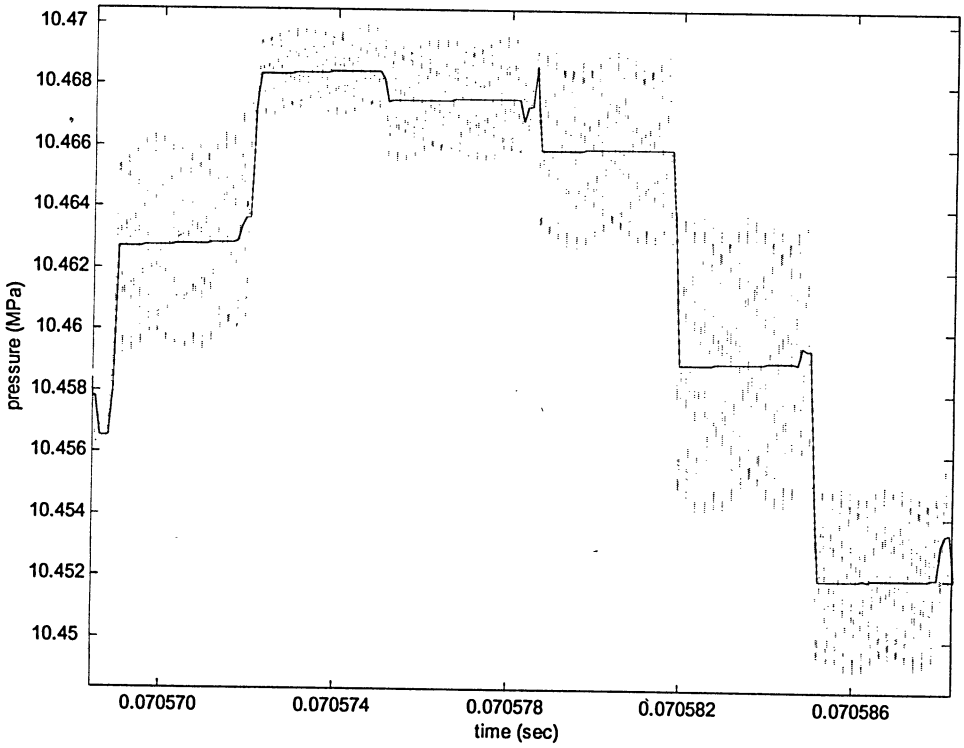

Figure 4-3 Averaged pressure values

For the purposes of this study, a lag factor of 6 is found to produce satisfactory results and is chosen for the simulated firings. The effects of lagging the pressure are shown in Figure 4-4,

with the average pressure values included. The bold plot is the lagged pressure profile at the motor head-end using a lag factor of 6. These lagged pressure values are then applied to the FE structure as external loads, as mentioned previously in Section 2.4.1.

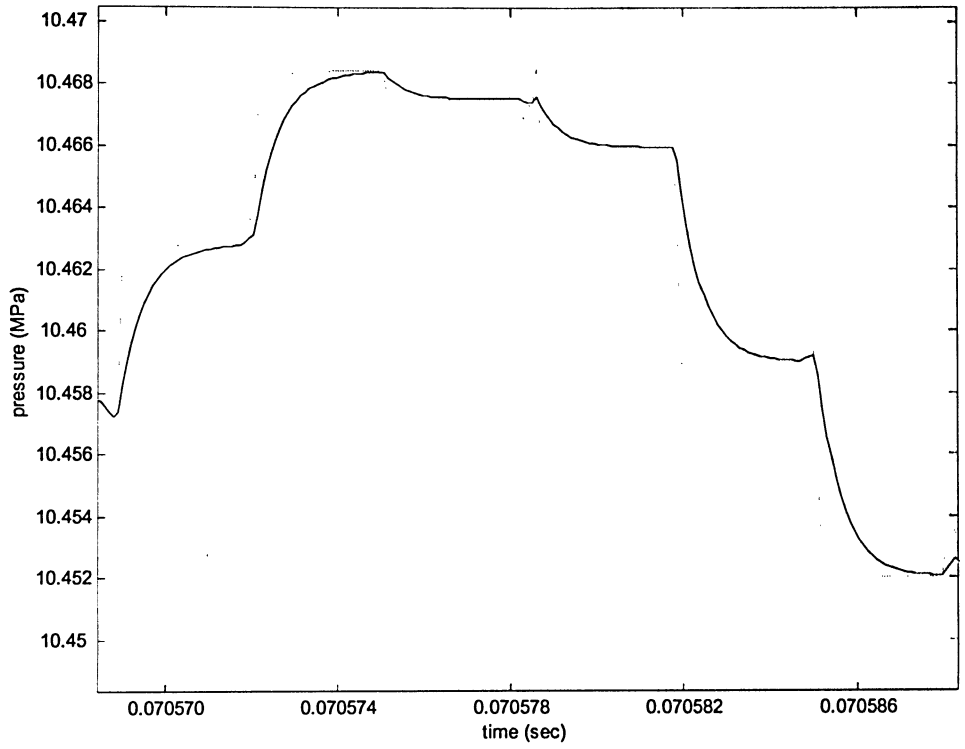

Figure 4-4 Lagged pressure values

The local burn rate values output from the burning rate component are required in order for the FE structural mesh to be regressed. These values are also interpolated using Equation (4.1b) and then applied to the mesh using the methodology detailed in Section 2.7. The FSI interface component ensures that the burn rate is applied to the structure, and that the regression is performed accurately over time. The regression only occurs during the quasi-steady portion of the IBF solution, before the FE structural component is initiated. As mentioned, it would be extremely difficult to regress the propellant during the unsteady portion of the simulation. This would require a large increase in computation time, and could potentially introduce numerical problems, restricting the simulation from reaching a converged solution. The final regressed mesh after completion of the quasi-steady flow

calculations is then passed to the FE component for calculation of the system mass, damping and stiffness matrices, which are used for the remainder of the simulated firing.

Time step size was discussed for both the FE and IBF components separately. Now, a discussion on the overall simulation time step size will be addressed. Time steps are critical when coupling both the fluid and structural components, and the type of numerical techniques used (either implicit or explicit time integration methods) can influence the time steps chosen. For example, if the structural algorithm uses an implicit solver and the fluid algorithm employs an explicit solver, there may be problems with maintaining consistent time (generally, implicit solvers require data from only the previous time step, while explicit solvers may require data from the previous few time steps). The structural solver can also use a larger time step compared to the fluid solver. This is known as a staggered algorithm approach, where there exists a time lag between the fluid and structural solvers. Here, non-physical energy dissipation is introduced into the system, which can pose a problem in data transfer and continuity between the two components.[31] A small simulation time step can remedy this quite easily, where in this study the simulation time step is simply set to the explicit flow time step given by Equation (3.16). Conversely, if both the structure and fluid algorithms use implicit solvers, this problem cannot exist because they are solved simultaneously. This is known as a fully coupled simulation, where there is no time lag between the structural and fluid components and continuity between the two components in definite. The later example is preferable, but the former can be just as effective if small time steps are used for both the fluid and structural algorithms as mentioned. The case of an implicit structural solver and the explicit flow solver is used for various simulations in this study. The time step used in this case is in fact the half-time step of the simulation. Recall that the IBF solver divides the simulation time step into two half-time steps, thus the FE component time step is actually equal to the half-time step of the IBF component, given by Equation (3.16).

In some simulations, when both the structural and fluid components use explicit methods, both time steps are limited; thus, the choice of the time step can get complicated. Generally, the time step used for the simulation (i.e., half-time step) is usually the minimum

of the two, which are both restricted by stability requirements. In other words, the half-time step is given by Equation (4.5), where both the FE and IBF components use this time step.

$$\Delta t = min(\Delta t_{IBF}, \Delta t_{FE}) \tag{4.5}$$

In the case of this study, the explicit FE time step is always smaller than the explicit IBF time step. Since the flow solver uses two half steps, the simulation time step is set to the IBF time step. This is a drawback for simulation in the time domain, where sub-time steps are necessary for the FE component before the simulation time step can proceed. This does increase computational time for the overall simulation, which is the case here when an explicit structural method is used. Sub-step coupling routines are usually needed to ensure time is consistent between the two components, and that continuity is maintained. Thus, depending on the size of the FE time step, many FE iterations are run in between the IBF half-time steps to ensure both components are in time synchronization and that continuity is maintained. To determine the number of FE time steps run for every IBF time step, first both the FE and IBF time steps are calculated using Equations (2.77) and (3.16), respectively. Then, the following trivial relationship is used to determine the sub-step number T_{sub}.

$$T_{sub} = \left(\frac{\Delta t_{IBF}}{\Delta t_{FE}} \right) + 1 \tag{4.6}$$

The ratio of the IBF and FE time steps is rounded down to the nearest integer number, which will always produce a sub-step number of 2 or greater, since $\Delta t_{FE} < \Delta t_{IBF}$. The simulation half-time step is then set equal to the IBF time step, while the FE time step is given by

$$\Delta t_{FE} = \frac{\Delta t_{IBF}}{T_{sub}} \tag{4.7}$$

This equation ensures that the fluid and structural components are time synchronized, while accuracy is maintained throughout the simulated motor firings.

In summary, if the FE transient solver is implicit, the FE time step is set to the IBF time step and the simulation half-time step is also set to the IBF time step (i.e., $\Delta t = \Delta t_{FE} = \Delta t_{IBF}$). There are no sub-steps required in this case since the FE solver is unconditionally stable. However, when the FE solver is explicit and the FE time step is smaller than the IBF time step, the simulation half-time step is set equal to the IBF time step, while the FE time step is given by Equation (4.7). There are T_{sub} sub-steps with this formulation. Finally, if the

FE solver is explicit and the FE time step is larger than the IBF time step, the FE time step and simulation half-time step are set equal to the IBF time step, without use of sub-steps. Typically for this study, the IBF time step is calculated to be in the order of 10^{-7}, while the explicit FE limiting time step is of the order 10^{-8}.

The purpose here is to show how all the components discussed thus far are incorporated in the simulation. The overall simulation schematic is given in the flow chart of Figure 4-5, which illustrates the specific portions of the simulation with respect to the various components and subroutines mentioned. The simulations begin with the initialization of the FE component parameters. Here, the FE structural mesh is input into the algorithm via the text files created by ANSYS, and the FE arrays are sized depending on the number of elements and nodes in the structural mesh. The FE parameter input file is also read into the algorithm, where various integer values determine the type of mass matrix, the type of damping model, the damping ratio, the FE Courant number, the FE numerical constants, the time integration method and other FE component options intrinsic to the algorithm. The FE mesh is also scanned at this point in order to determine the elements and nodes on the boundaries to apply any loading, physical constraints and for regression of the FE mesh. The element mass and stiffness matrices are also determined, where an option for a static, free vibration and transient analysis of the FE component is completed. Note that any desired harmonic analysis and natural frequency calculations are done at this point. This is not part of the simulation itself, but is necessary for a new structural geometry. The calculated frequency values are then included into the FE input text file, and the program is restarted without the harmonic analysis option. If an explicit FE integration method is desired, the FE time step is also calculated here. The simulation then proceeds with the reading of the IBF component input text file, and the initialization of the flow and burning rate component arrays.

The main simulation loop is then entered, which is denoted by the 'do-loop' in the flow chart and governed by the iteration variable I. At the beginning of every iteration, the simulation time is checked to determine whether the flow component requires quasi-steady or unsteady calculations. If the simulation time is less than TQSE, the quasi-steady portion of

the simulation is entered. However, if time is greater than TQSE, the unsteady portion of the simulation is entered and continued for the remaining duration of the simulation. The quasi-steady portion consists of solving the flow parameters via Equations (3.1), (3.2) and (3.3) with the time derivatives set to zero, and the local burning rate of the propellant. The FE mesh is regressed during this portion of the simulation, while the FE transient calculations are not performed. The port area required for the IBF component is calculated based on the regressed propellant only. All quasi-steady iterations are identical, using a predetermined time step input from the IBF input text file. Data output is done for each quasi-steady iteration, as indicated in the flow chart. Once the preset time of TQSE is passed, the unsteady portion of the simulation begins.

As mentioned, solution of the unsteady flow equations using the explicit finite-volume RCM requires the use of two half-time steps each iteration. Each half-time step is identical in the simulation (except for the fact that the IBF spatial nodes are shifted during the first half-time step), as is each complete unsteady iteration. Each half-time step begins with the calculation of the IBF time step and the synchronization of the simulation half-time step with both the calculated FE and IBF time steps. The number of sub-steps required is also determined, if applicable. The burning rate component is then entered, and the local burn rate values are determined by the algorithm previously shown in Figure 3-5. The unsteady flow parameters are then calculated using the burn rate values and applicable structural acceleration values. Once the local flow pressure values are known, the spatial and time interpolation of these values is performed and the FE load vector $\{F\}$ is calculated to be used for the FE transient calculations. The calculation of the structural displacement, velocity and acceleration vectors follows. If an explicit FE solver is used, the parameters for each FE sub-step are calculated here, and the FE solution is brought to the point in time of the IBF solution. Note that use of the previous half-time step FE values such as displacement and acceleration for the current time step IBF calculations is a good assumption here, since small simulation time steps are used throughout the analysis. Next, the interpolation of the FE acceleration and displacement values is completed for use in the next half-time step. The displacement and burn rate values are now used for regression of the propellant, and to determine the updated port area for the next flow calculations.

Once the entire unsteady iteration is complete, motor thrust calculations and IBF mesh corrections are performed before data is output to corresponding files. At this point, the time is checked to determine whether or not to introduce the disturbance (i.e., traveling shock wave). Once the disturbance is introduced, this check is no longer performed. The unsteady simulation iterations are repeated until a predetermined iteration number is reached, denoted by NSTOP in the flow chart. For most simulations in this study, the required number of iterations is in the vicinity of 300,000 (i.e., 600,000 half-time steps).

All simulations of this study consist of quasi-steady calculations up to the time denoted by TQSE, where the FE mesh is regressed and the FE calculations are not performed. At time TQSE, the unsteady flow and FE calculations begin and the FE mesh is no longer regressed. The structure and fluid components are allowed to stabilize for a short period of simulation time, before the disturbance is introduced into the flow. This is done to significantly reduce computation time and to allow a fairly smooth parameter profile before the shock wave is introduced. The flow and structural characteristics after the shock wave is introduced into the flow is the primary focus; thus, this solution approach will not deter the main objective of this study. Once the disturbance is introduced, the simulation is allowed to run for approximately 20 – 40 ms in simulation time. The data collected during the simulated firings includes the pressure and burn rate at various axial locations in the motor, as well as the longitudinal and radial acceleration of the propellant inner surface at various motor axial locations. The steel sleeve outer surface radial displacement and acceleration at various axial locations is also output, as well as the propellant radial displacement. All parameters are output at the end of every iteration to text files, the time profile of which can be plotted in any graphing program.

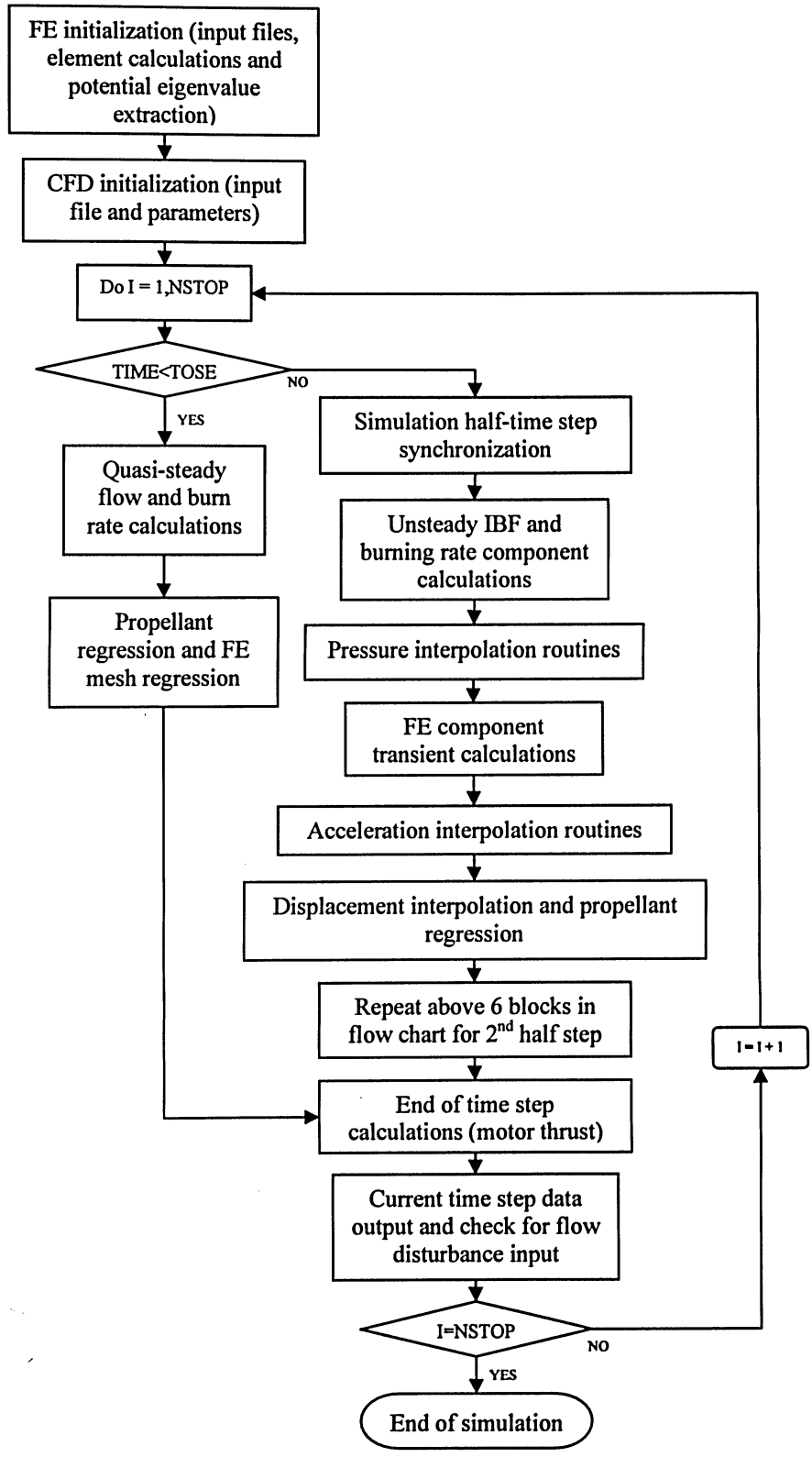

Figure 4-5 Simulation flow chart

5 Results and Discussion

5.1 Early Simulation Results

In Section 2.6, some preliminary results for the FE component of this simulation were presented. In this section, preliminary simulation results will be presented and discussed with the purpose of yielding some insight with the modeling involved in this study. These results are not presented in full, but are analyzed in a qualitative sense to show how each component affects the others and to show how the overall simulated firings are affected by changing various simulation and component parameters. The results to be presented in this section include the motor head-end pressure, and the propellant inner surface radial and axial acceleration values.

The cylindrical-grain motor characteristics used in this study are similar to those found in Reference 1, with the exception of some different structural parameters such as the system damping ratio and response frequency. The structural material properties and geometry were presented in Table 2-1, where the combustion chamber gas flow and burning rate parameters are included in Table 5-1. (Note that the shaded parameters refer to the structural model and are altered for some simulations to be presented here.) For each simulated firing, the motor is pulse-triggered into instability with a 1.2-MPa traveling shock wave (original disturbance as discussed in Section 3.6). The pulse is introduced when time is equal to 90.5 ms, after the unsteady calculations are run and settled for 10 ms, and the simulation is left to run further for approximately 20 ms. The propellant web thickness when the shock wave is introduced is similar to that used in the experimental runs of Reference 1. The propellant characteristics are typical for the nonaluminized ammonium perchlorate/hydroxyl-terminated polybutadiene (AP/HTPB) propellant used in this study. The pressure-dependent burning rate parameters (C and n) from Equation (3.5) are combined in Table 5-1.

Various FE meshes are used in this preliminary simulation analysis, which are clearly stated for each set of results. For all simulations the IBF grid is set to have 260 axial nodes,

120 on the propellant grain and 140 through the nozzle convergence to the nozzle exit plane. For all simulations, both the FE and IBF Courant numbers are set to 0.5. The structural damping ratio and response frequency used in each simulation is also stated, and depend on the mass matrix used for the simulation. For most simulations, a lumped mass matrix with an 8-node hexahedral element is used, as discussed in Section 2.6.3. Also for each simulation, the specific time integration method, damping model, boundary constraints, and disturbance type will be mentioned as applicable.

Initial grain port diameter (d_i)	3.6	cm
Nozzle throat diameter (d_t)	1.6	cm
Grain/nozzle convergence length ratio (L_p/L_c)	16	--
Pressure-dependent burn rate (r_p)	$0.05[p(\text{kPa})]^{0.35}$	cm/s
Propellant specific heat (C_s)	1500	J/kg-K
Propellant flame temperature (T_f)	3000	K
Propellant surface temperature (T_s)	1000	K
Initial propellant temperature (T_i)	294	K
Propellant surface roughness (ε)	400	μm
Gas specific heat (C_p)	2000	J/kg-K
Gas Prandtl number (Pr)	0.828	--
Specific gas constant (R)	320	J/kg-K
Gas thermal conductivity (k)	0.195	W/m-K
Gas absolute viscosity (μ)	$8.07\text{x}10^{-5}$	kg/m-s
Gas specific heat ratio (γ)	1.2	--
Particle mass fraction (α_p)	0%	--
Structural damping ratio (ζ)	0.35	--
Structural fundamental frequency (ω_1)	1790	Hz
Structural response frequency (ω_2)	15950	Hz

Table 5-1 SRM motor characteristics

5.1.1 Element Type Comparison

The first two simulations to be presented are done with the purpose of comparing the results between the 8-node and 20-node hexahedral elements. The simulations are identical, except for the fact that the element type is different. The mesh used here is the 520 element mesh from Table 2-2, where the response frequency and damping ratio are given in Table 5-1 for a consistent mass matrix. Note this frequency is slightly higher than that stated in Section 2.6.1 due to the regressed propellant mesh, which increases the response frequency of the structure. The Newmark time integration method is used, with a Rayleigh damping model. The first few cycles of the disturbance for the 20-node element mesh are shown in the motor head-end pressure-time and propellant surface mid-grain radial acceleration-time profiles of Figure 5-1 and Figure 5-2, respectively. The same results for the 8-node element mesh are included in Figure 5-3 and Figure 5-4.

The head-end pressure profiles are similar in both simulations, with respect to base pressure increase and shock peak amplitudes. However, the acoustic oscillations between the shock cycles are much smoother and lower in level in Figure 5-1. The reason for this is the fact that the numerical time integration constant γ used in the implicit Newmark time integration solver is set to a value of 10.0 (i.e., high artificial damping) for the 20-node element mesh simulation, versus a value of 0.5 (i.e., no artificial damping) for the 8-node mesh. Increasing the numerical constant was necessary when using the 20-node hexahedral elements because of the excessive numerical noise in the solution. Without increasing γ the shock-front does not develop properly, which is clear through the radial acceleration and pressure profiles (not included). This consequently affects the propellant radial acceleration peaks, since the system is far too over-damped, versus the 8-node element mesh simulation, which exhibits only structural damping. The firsts few positive acceleration peaks are slightly lower in Figure 5-2 than in Figure 5-4. Also, the acceleration fluctuations before the disturbance is introduced are much higher in magnitude during the 20-node element simulation. This is undesirable due to the negative affects on the shock-front, which could potentially dissipate enough acoustic energy to 'kill' the wave system. This is not seen in the experimental runs for the same motor.[1] Note that the low magnitude of the negative

acceleration peaks (which affects the burning rate) is a problem with both simulations, and can potentially be increased with refinement of the FE structural mesh and by decreasing the structural damping ratio. The propellant mid-grain axial acceleration profiles (not included) for both simulations are analogous to the radial acceleration profiles. The axial acceleration peak magnitudes for the 20-node element mesh simulation are approximately half of the peak magnitudes for the 8-node element mesh simulation, again due to the significant increase in the Newmark artificial damping constant.

The purpose of the next simulation is to improve the results obtained for the 8-node element mesh simulation. In this case, only the damping ratio is decreased with the intention of increasing the negative propellant radial acceleration peaks, which will increase the local burning rate, potentially adding enough energy into the flow to sustain the wave system. The damping ratio is set to 0.10, versus 0.35 previously. The head-end pressure time profile and mid-grain propellant radial acceleration-time profile are shown in Figure 5-5 and Figure 5-6, respectively. The radial acceleration positive peaks are higher in magnitude, as is the first negative peak, in comparison with the simulation with a higher damping ratio. This is a typical result when the damping ratio is decreased; however, notice that there is an increase in magnitude with the acceleration oscillations between the peaks. This illustrates an important aspect with the structural modeling involved in this particular study. When the damping ratio is relatively high, the acceleration peaks are too low, but the post-shock oscillations are reduced in magnitude. When the damping ratio is relatively low, the acceleration peaks are higher, but the post-shock oscillations increase in magnitude. This is the trade-off with the system damping ratio, and since the damping properties of the structure are not fully understood, there is a trial-and-error approach to find the most accurate damping ratio. The acoustic post-shock oscillations are also evident in the head-end pressure-time profile of Figure 5-5. The shock-front is unable to be sustained, which is similar to the previous simulation with a higher damping ratio.

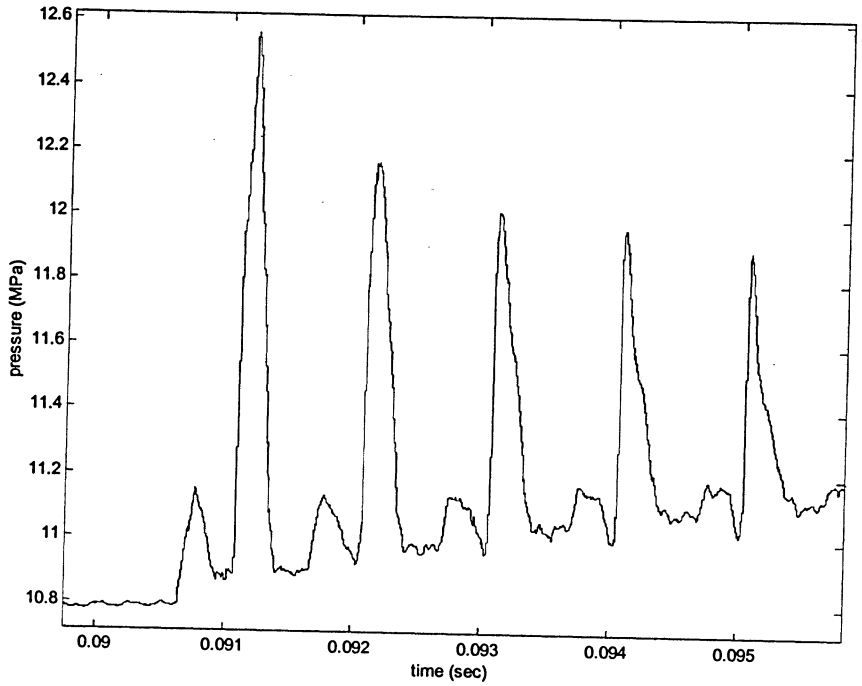

Figure 5-1 Head-end pressure (20-node element mesh)

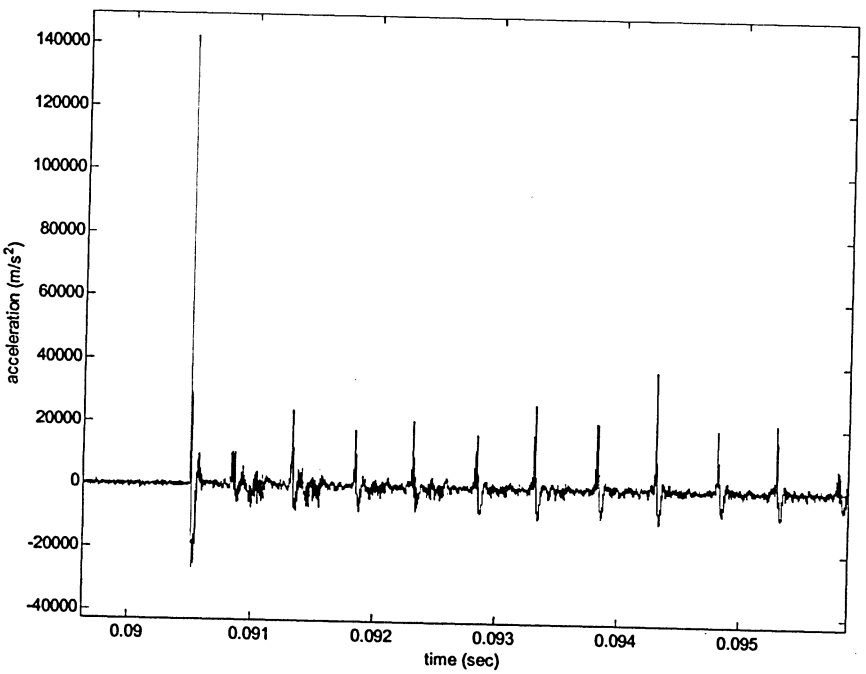

Figure 5-2 Propellant mid-grain radial acceleration (20-node element)

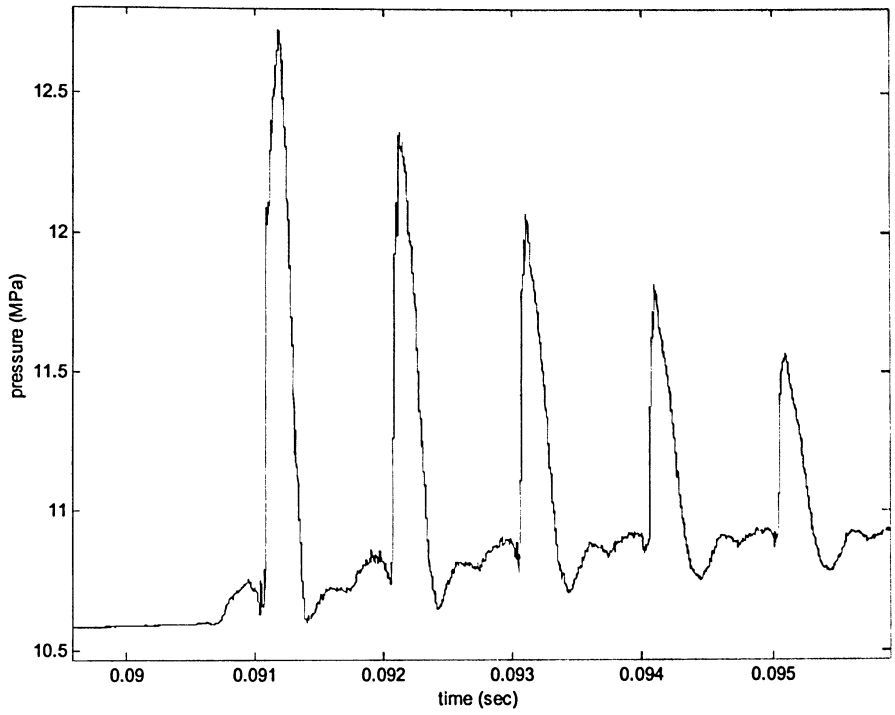

Figure 5-3 Head-end pressure (8-node element mesh)

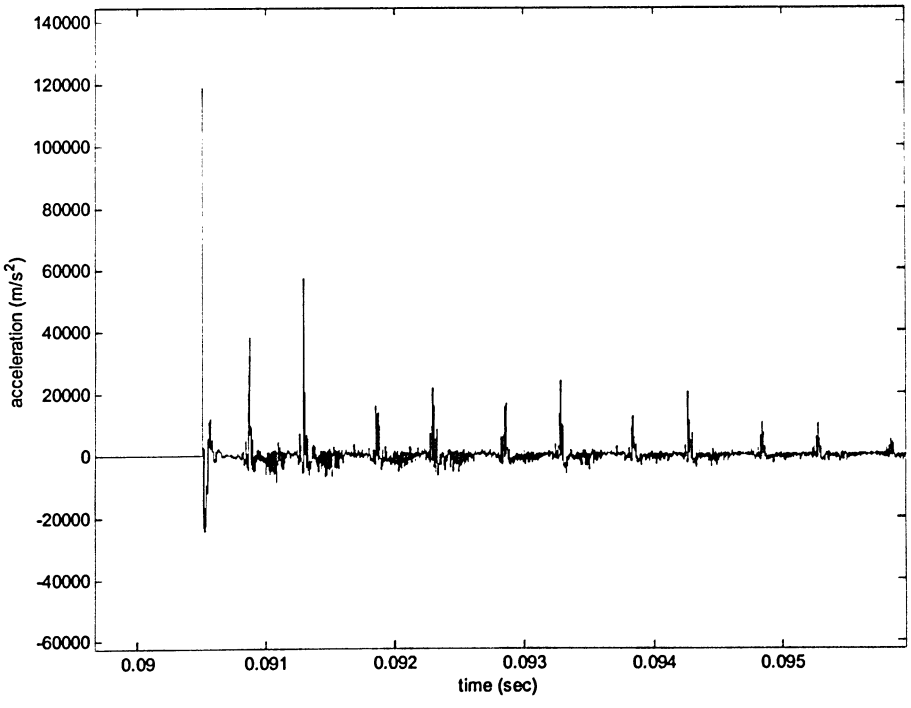

Figure 5-4 Propellant mid-grain radial acceleration (8-node element)

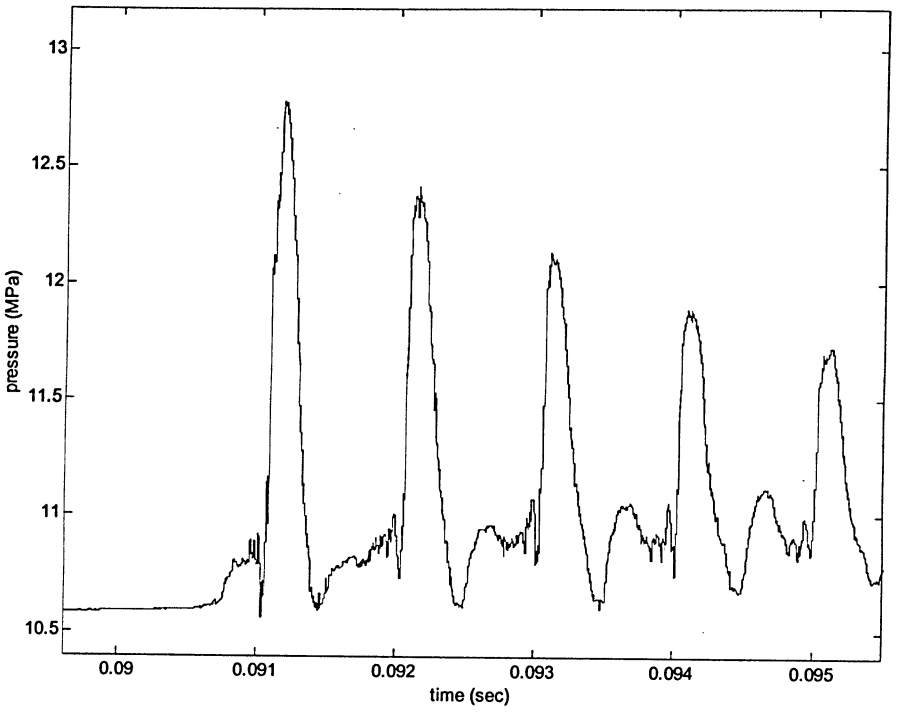

Figure 5-5 Head-end pressure (8-node element, ζ=0.1)

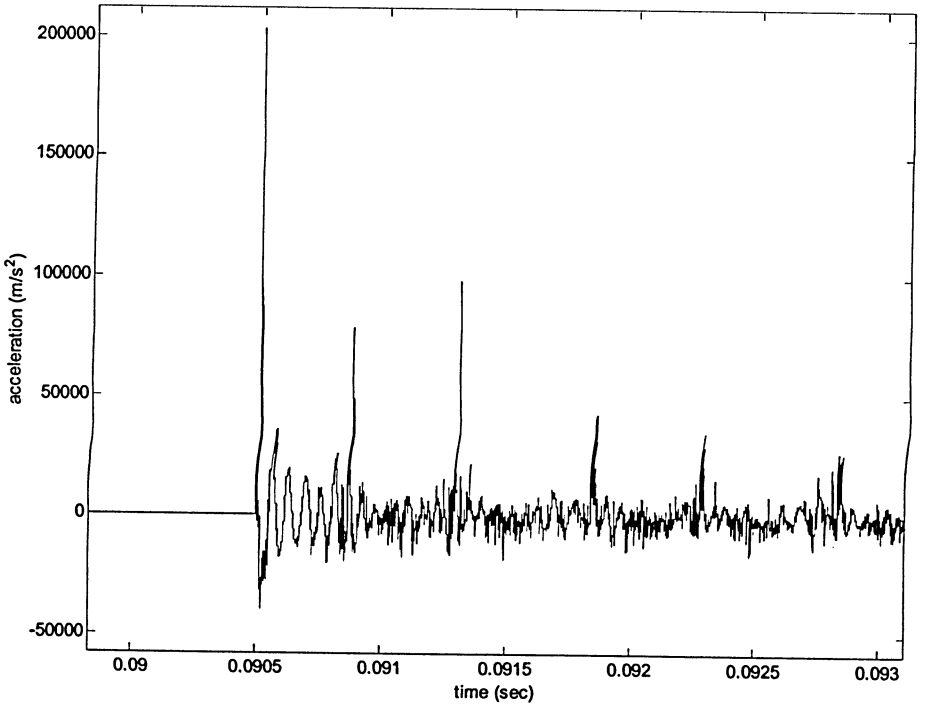

Figure 5-6 Propellant mid-grain radial acceleration (8-node element, ζ=0.1)

Other simulations are run with damping ratios varying between 0.1 and 0.75, with results similar to those shown in Figure 5-5 and Figure 5-6. The need to refine the FE structural mesh becomes evident, and will be discussed subsequently. Moreover, the propellant mid-grain axial acceleration-time profile is illustrated in Figure 5-7. The movement of the shock-front in the axial direction is unclear through the plot, suggesting that artificial (or numerical) motion may also be influencing the shock wave development. A similar result is found for varying damping ratios, where the positive and negative peak magnitudes for the axial acceleration are greatest when the damping ratio is decreased. Considerations for refining the FE mesh and use of an explicit time integration solver are now discussed.

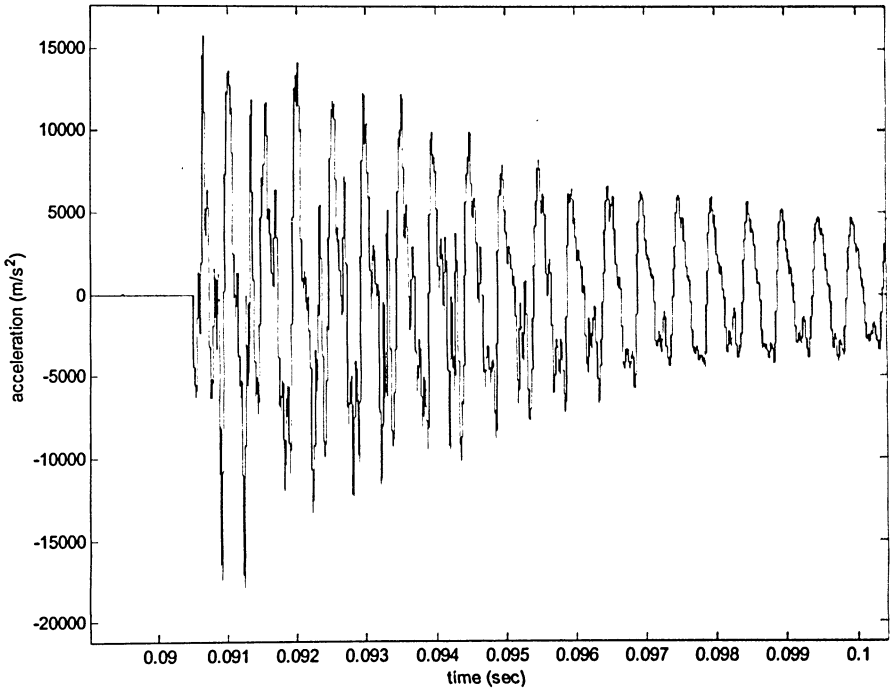

Figure 5-7 Propellant mid-grain axial acceleration (8-node element, ζ=0.1)

5.1.2 Mesh Refinement

Refinement of the FE structural mesh requires an increase in both the simulation time and computational storage requirements. With respect to storage requirements numerical

techniques have been adopted in the algorithm for efficiency; thus, a significantly refined mesh will not pose any major difficulties. However, mesh refinement will significantly increase the computation time, as shown in Figure 2-29. Attempts can be made to refine the mesh with the use of an implicit method, but the amount of refinement is limited because of the time restriction. For example, it would not be feasible to refine the mesh to say 10,000 elements and have a simulation running for 60 days. In order to show the effects of refining the mesh in both the axial and radial directions, refinement in these directions is done separately to isolate the results. Only structural acceleration results will be shown with the refined mesh simulations, since the pressure profiles are similar to those found in Figure 5-3 and Figure 5-5.

The same simulation using an 8-node element mesh with a damping ratio of 0.35 is run, with the mesh refined in the axial direction only. The 1300, 8-node element mesh listed in Table 2-2 is used for the simulation. The steel-sleeve head-end outer surface radial acceleration-time profile is shown for the 520 and 1300 element meshes in Figure 5-8 and Figure 5-9, respectively. The positive and negative peak magnitudes are similar in both plots since the radial mesh is the same, but the oscillations after each shock-front cycle drastically reduce with the refined mesh in the axial direction. As a shock wave passes a particular axial location in the combustion chamber, the sudden increase in pressure will cause a sudden spike in radial acceleration in the outward (positive) direction, followed by an inward (negative) spike, followed by small amplitude oscillations. The refined mesh better resembles the expected physical structural response to the passing shock wave. This is also evident when analyzing the propellant mid-grain axial acceleration-time profile shown in Figure 5-10, for the 1300 element mesh. The acceleration peak magnitudes are higher than in the case of the 520 element mesh, due to the increased flexibility of the FE mesh. The increase in the axial acceleration peak magnitudes was desired, since the axial acceleration was found by Greatrix[13] to be closer in magnitude to the radial acceleration peaks. It becomes evident that the axial motor response significantly affects the radial response of the motor structure. This will be considered with the simulated firings discussed in Section 5.2.

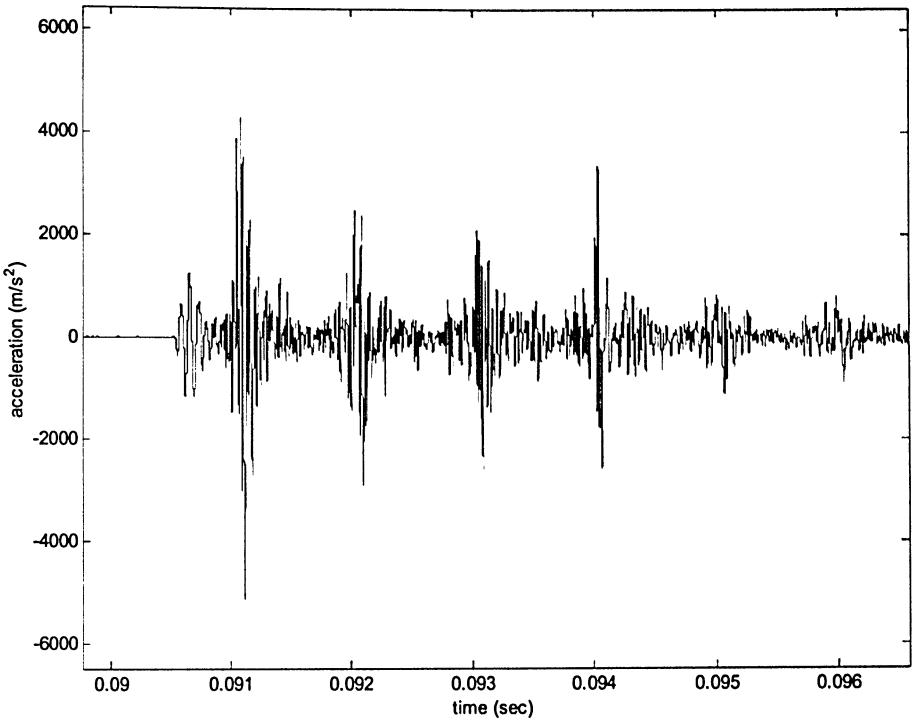

Figure 5-8 Head-end steel radial acceleration (520 element mesh)

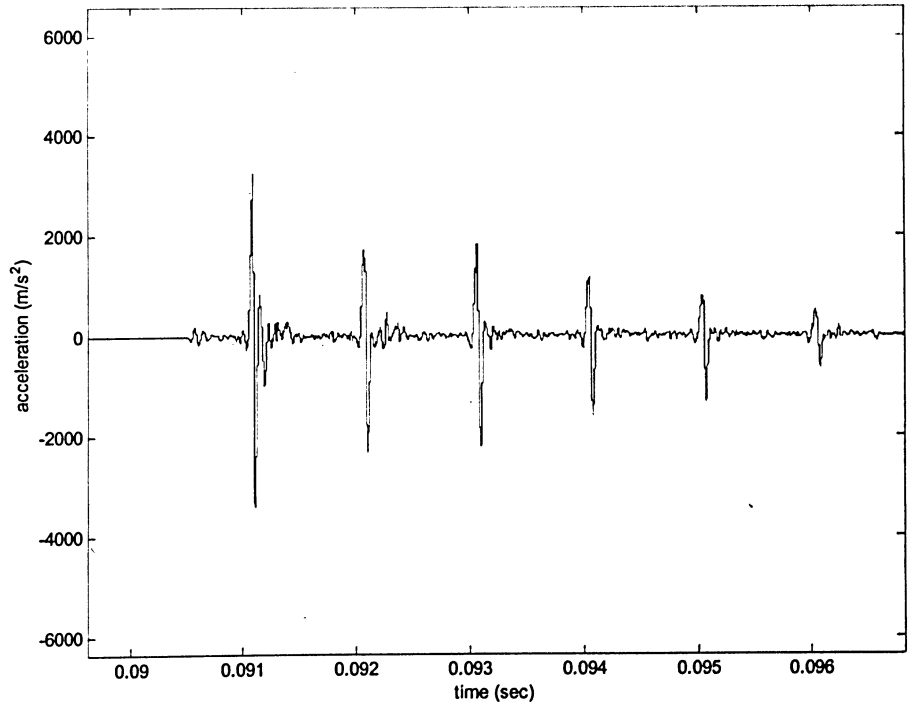

Figure 5-9 Head-end steel radial acceleration (1300 element mesh)

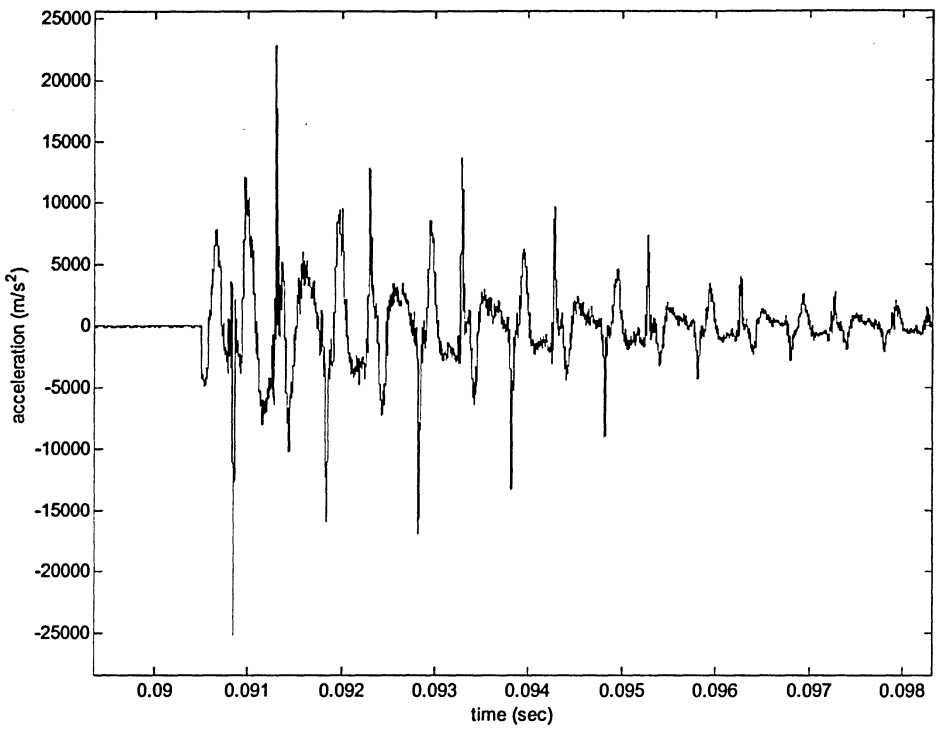

Figure 5-10 Propellant mid-grain axial acceleration (1300 element mesh)

Now, consider refinement of the FE mesh in the radial direction only, using the 1160 element mesh of Table 2-2 (in lieu of the 520 element mesh). The simulated motor head-end steel-sleeve outer radial acceleration-time profile is included in Figure 5-11. The oscillations between each shock cycle have reduced drastically, and are comparable to the axially refined mesh results of Figure 5-9. Note that the acceleration peak magnitudes are similar to those shown in Figure 5-9. Refinement of the mesh in both the axial and radial directions has a significant impact on the simulation results as shown. However, due to the restriction of the implicit time integration methods, refining the mesh in both directions is not economical. The obvious choice is to switch to an explicit time integration method, which is much quicker and allows for a refined mesh to be simulated in a reasonable time frame. In order for this to work, a mass-proportional damping model must be employed in the simulation. As shown in Section 2.6.2, this comes with a penalty of having to introduce artificial damping in the solution due to the increased structural response.

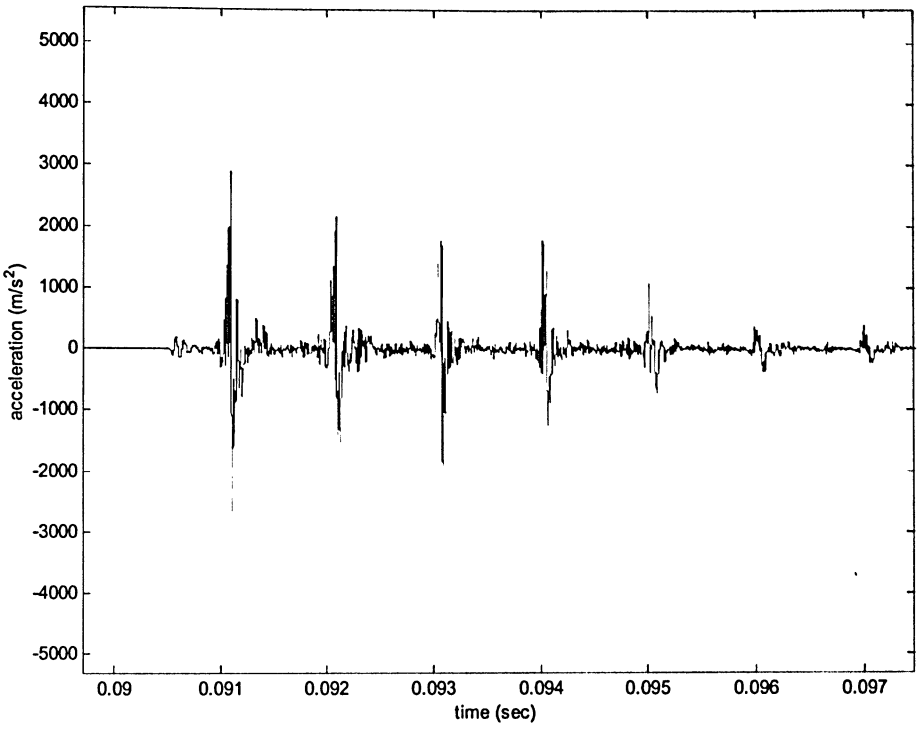

Figure 5-11 Steel head-end radial acceleration (1160 element mesh)

Now, consider the use of the explicit Newmark time integration method with mass-proportional damping and a lumped mass matrix (versus the implicit Newmark method with Rayleigh damping and a consistent mass matrix used previously). The response frequency is found to be 14950 Hz for the lumped mass matrix, and the Newmark integration constant γ is set to 1.20 to reduce the numerical solution noise. The 520 element mesh is used to show the effects of changing the damping model. The head-end pressure-time profile and propellant mid-grain radial acceleration-time profile are shown in Figure 5-12 and Figure 5-13, respectively. There is a much larger dc rise versus the simulation pressure-time profile shown in Figure 5-3, with corresponding higher peak magnitudes. The main shock-front does, however, eventually dissipate, similar to all previous simulated firings. The propellant radial acceleration peak magnitudes are much higher than the results in Figure 5-4. The post-shock oscillations are also higher in magnitude, due to the insufficient damping on the structure. The oscillations may be overwhelming for the shock-front, potentially restricting the shock wave from sustaining itself. Also, the added numerical damping may be controlling the simulation noise, but may also be a factor in restricting a sustained shock

wave. Similar trends are found with the steel radial acceleration-time profile and propellant axial acceleration-time profile, results of which are not included here.

Note that the simulations involving the use of explicit time integration methods with Rayleigh damping models (results not included) yielded the same results versus implicit time integration methods. The main difference in results here is due to the change in damping model. Also, implicit time integration methods with mass-proportional damping yield the same results as those shown in Figure 5-12 and Figure 5-13. The significance here is that a refined mesh can now be implemented into the simulation. For example, the simulations involving an explicit time integration method required on average 3 hours to be completed, while the same simulation using an implicit time integration method required approximately 17 hours to terminate (both on a PC with a 3.2 GHz Intel Pentium 4 processor).

The previous simulation is now conducted with a refined mesh in both the axial and radial directions in order to improve the previously presented results. The 14,400 element mesh of Table 2-2 is employed here, with the Newmark numerical constant γ set to 0.95.

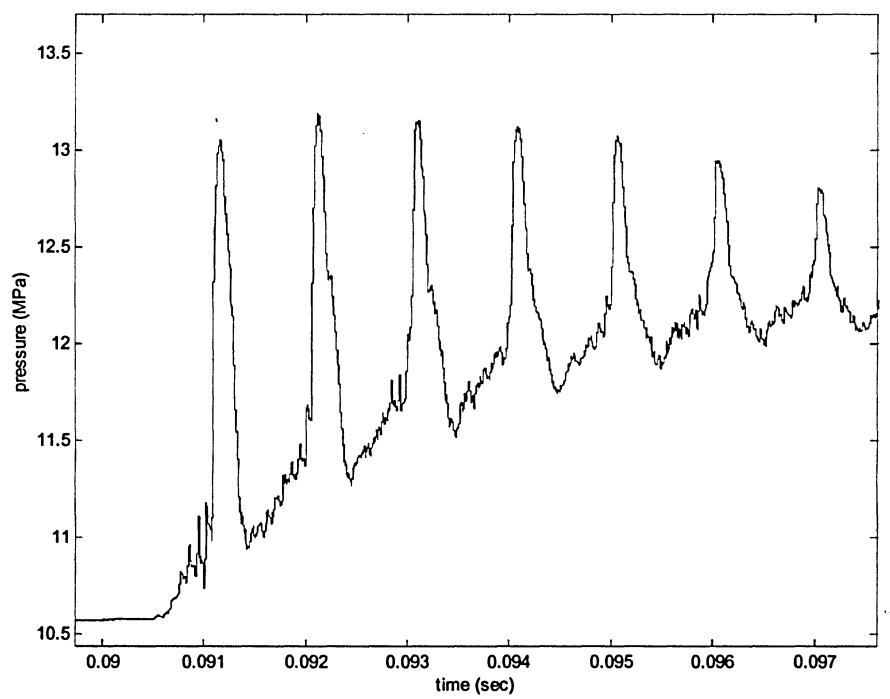

Figure 5-12 Head-end pressure (explicit, 520 element mesh)

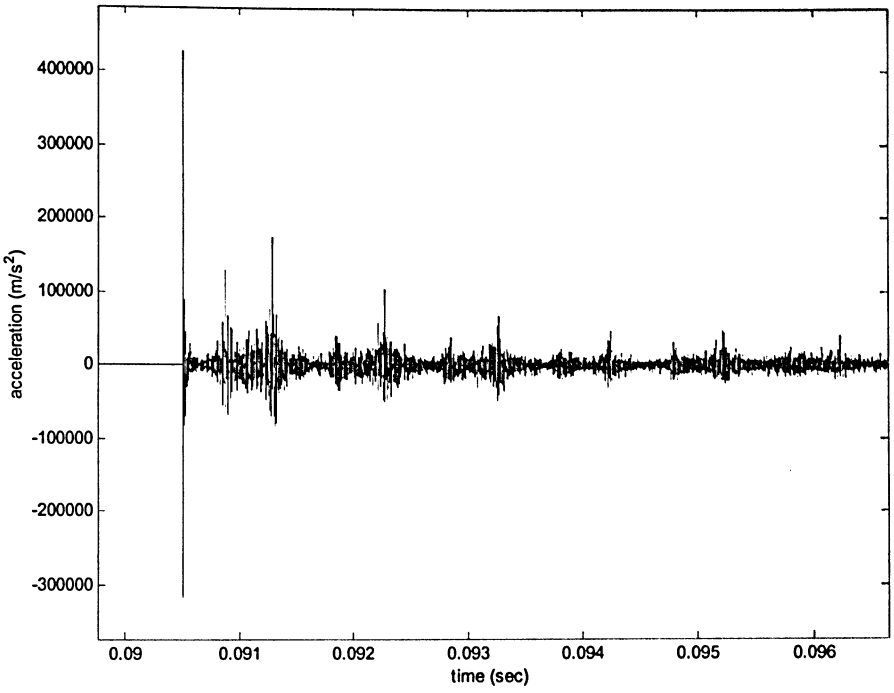

Figure 5-13 Propellant mid-grain radial acceleration (explicit, 520 element)

For this particular simulation, the system damping ratio is changed to 0.25. The head-end pressure-time profile and propellant mid-grain radial acceleration-time profile are shown in Figure 5-14 and Figure 5-15, respectively. The pressure peak magnitudes are higher versus all previous simulations, with a comparable dc rise to the thin-sleeve experimental results for the same motor configuration.[1] The shock-front does eventually dissipate after a few more cycles, but the overall improvement in the results is evident. The pressure plot reveals that the shock wave is initially sustained at a peak magnitude of approximately 2.5-MPa, but eventually dissipates after a few more cycles. Simulations with the damping ratio and Newmark numerical constant γ increased or decreased slightly failed to yield a sustained wave, results of which are similar to the pressure-time profile of Figure 5-14.

The acceleration plot of Figure 5-15 reveals the improvement in the propellant acceleration field, with an increase in the negative acceleration peak magnitude versus all previous simulations. The post-shock oscillations have significantly reduced in magnitude versus the 520 element mesh, explicit time integration method simulations. The propellant mid-grain axial acceleration-time profile is shown in Figure 5-16, with the propellant mid-

grain burning rate-time profile included in Figure 5-17. The axial response and acceleration have also improved due to the refined FE mesh. Notice the distinct positive and negative peaks in the plot, which is not evident in previous simulations (for example, see Figure 5-7 and Figure 5-10). This better represents the physical movement of the shock-front, back and forth in the axial direction of the motor chamber. The axial acceleration peak magnitudes are also higher versus the simulations involving the unrefined meshes. The burning rate peaks over the base burning rate of Figure 5-17 all correspond to the negative propellant acceleration peaks in Figure 5-15. Recall that only the negative normal (radial for cylindrical-grain motors) acceleration augments the burning rate. The propellant mid-grain radial acceleration and burning rate peaks correspond well to the levels predicted in the literature,[1] for the same motor configuration. Also, the steel-sleeve outer surface mid-grain radial acceleration-time profile (not included here) corresponds well to the experimental results.[1] The positive and negative peak magnitudes are approximately ±6000 m/s^2, which are higher in magnitude than all previous runs (for example, see Figure 5-9).

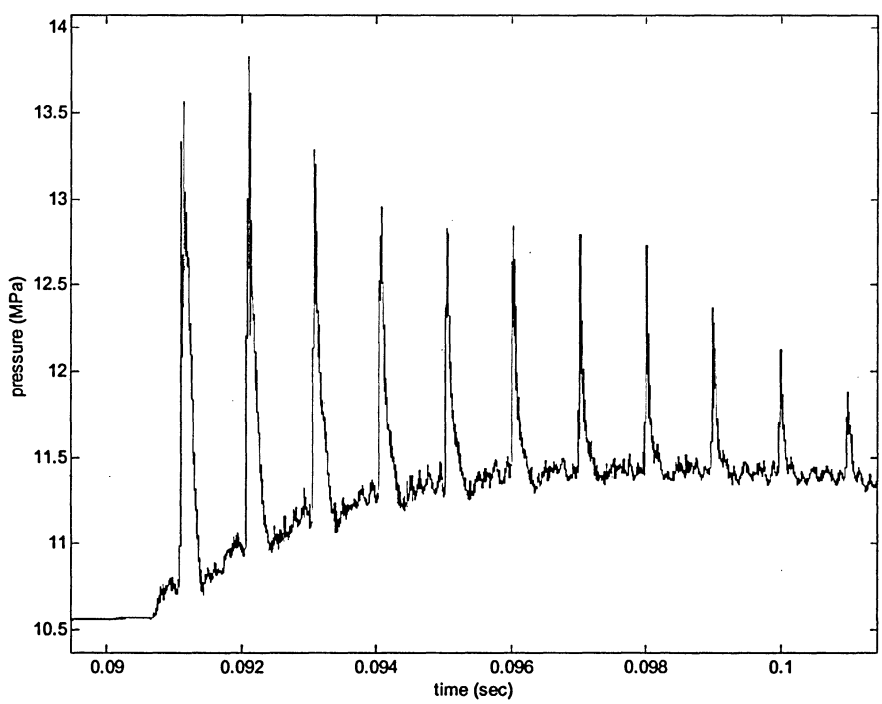

Figure 5-14 Head-end pressure (14,400 element mesh)

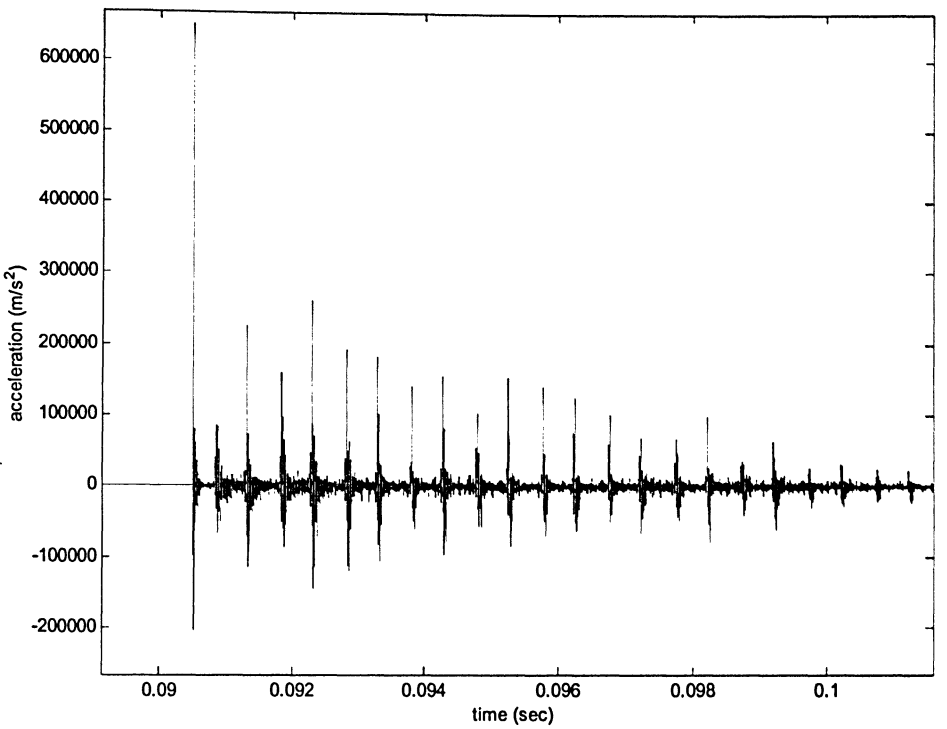

Figure 5-15 Propellant mid-grain radial acceleration (14,400 element mesh)

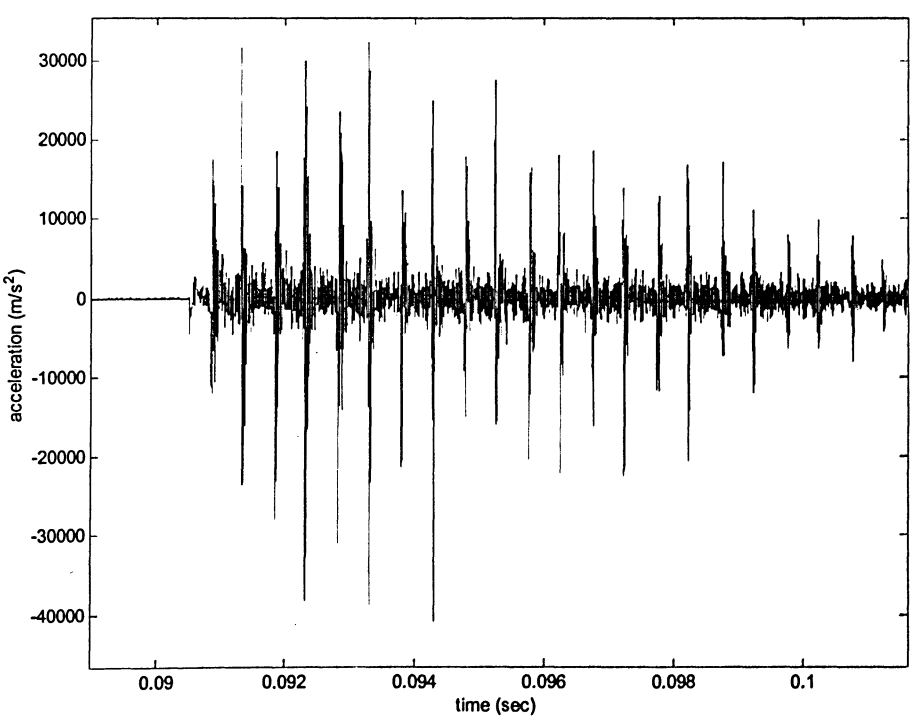

Figure 5-16 Propellant mid-grain axial acceleration (14,400 element mesh)

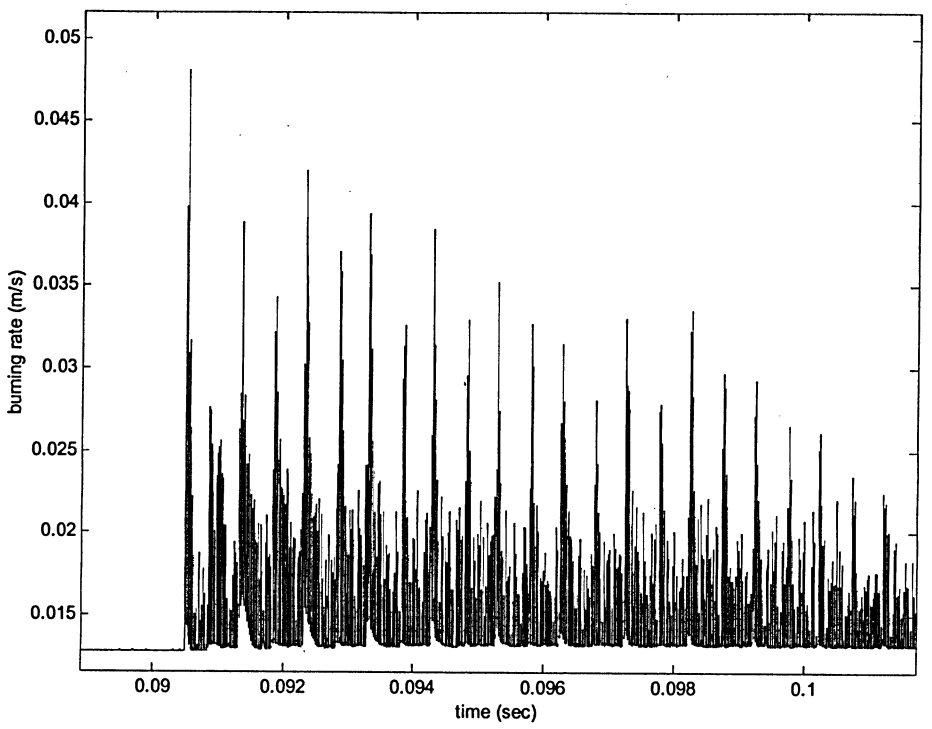

Figure 5-17 Propellant mid-grain burning rate (14,400 element mesh)

The 14,400 element simulation proves that the mesh refinement has a significant impact on the overall results. Although the traveling axial shock wave is not yet fully sustainable, the results illustrate important modeling concepts for this particular type of FSI problem and for this particular application. Moreover, an obvious trade-off exists between using an implicit time integration method with a Rayleigh damping model, and an explicit time integration method with mass-proportional damping. An implicit FE time integration method with Rayleigh damping would better represent the physical structural dissipation of the motor. Conversely, refining the FE mesh with use of an implicit method would not be economical, due to the significant increase in computation time (recall, a simulation is typically allowed to run for approximately 600,000 IBF half-time steps). Also, the choice of the structural damping ratio is a significant factor in the overall simulation results. The final choice of simulation parameters is discussed in the next section, where various simulated firings are performed to illustrate the effects of the disturbance strength, the damping ratio, and the type of disturbance on the simulation results.

5.2 Final Simulation Results

The results included in this section are in full, where the overall simulated firing profiles are shown in order to compare with experimental results involving the same motor and to see the trends of the SRM simulated firings. The discussion will focus on SRM combustion instability, rather than the modeling considerations discussed in the previous section. The choice of the modeling parameters used in these simulated motor firings is based in part on the results presented in the previous section.

These simulations are conducted with the same cylindrical-grain reference motor characteristics given in Table 2-1 and Table 5-1. The IBF grid, respective component Courant numbers and the disturbance time remains the same as the simulated firings presented in the previous section. Parameters such as the disturbance strength, disturbance type, number of elements in the FE mesh, damping ratio, Newmark numerical constant γ, the time integration method and damping model may change for various simulations. The corresponding parameter choices are indicated for each simulated motor firing. However, for all simulations an 8-node hexahedral element mesh is used, with corresponding natural and response frequencies for a lumped mass matrix.

5.2.1 Damping Considerations

It was noted that a Rayleigh damping model would provide a more accurate damping response versus the mass-proportional damping model. For this reason, a simulation is performed with use of the implicit Newmark time integration method and a Rayleigh damping model, where the propellant is restricted from moving in the axial direction. This causes the structural response to be analogous with previous two-dimensional models developed by Greatrix and Harris[1] and Loncaric, Greatrix and Fawaz,[10] with the difference of three-dimensional radial capabilities. This is done to provide use of a Rayleigh damping model, without having to use a refined FE mesh. Here, the 520 element mesh of Table 2-2 is used with a damping ratio of 0.25 and no artificial damping (γ=0.5). The motor is pulse-

triggered into instability using a 1.2-MPa shock-fronted disturbance (see Section 3.6 for details of disturbance types). The motor head-end pressure-time profile is shown in Figure 5-18, where the propellant mid-grain radial acceleration-time profile is included in Figure 5-19. Unlike the simulation results from Section 5.1, the shock wave is sustained throughout the simulation. The dc shift is comparable to that of the experimental results presented for the thin-sleeved motor in Reference 1, with a similar limit-cycle wave amplitude of approximately 3.5-MPa. The post-shock pressure oscillations have a frequency similar to the structural response frequency (~16 kHz), which was also seen with the experimental results. The propellant mid-grain acceleration peaks are similar to those obtained numerically by Loncaric,[32] with positive peaks reaching over 250,000 m/s^2 and negative peak magnitudes limited to approximately 100,000 m/s^2. The oscillations in the radial acceleration-time profile between shock cycles (Figure 5-19) clearly affect the acoustic oscillations shown in Figure 5-18, mainly due to the augmented burning rate caused by the acceleration field. Also, the mid-grain outer sleeve radial acceleration peaks are ~ ±8000 m/s^2 (not shown here), which are slightly lower than those found experimentally.

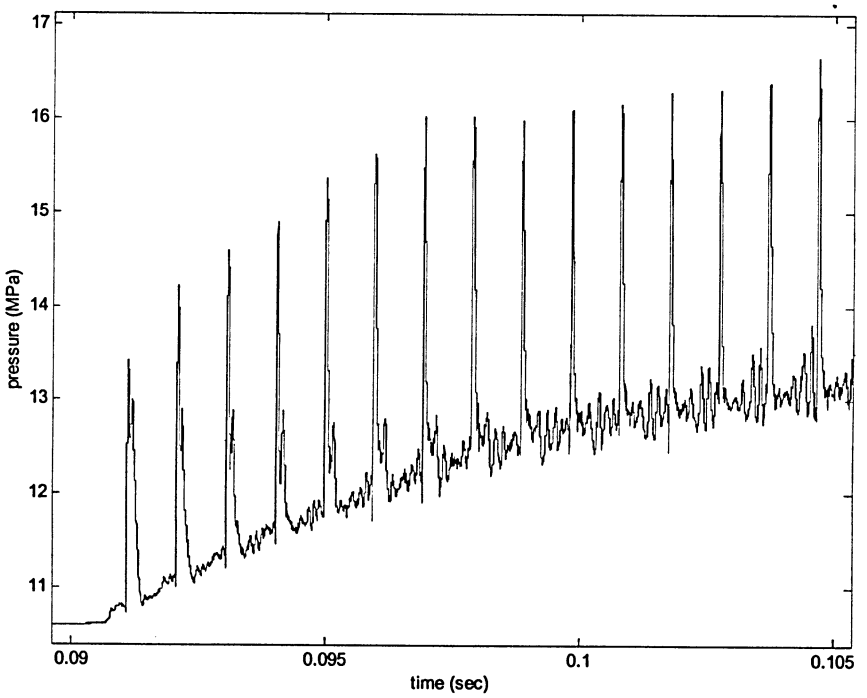

Figure 5-18 Head-end pressure (axially fixed): ζ=0.25, 1.2-MPa pulse

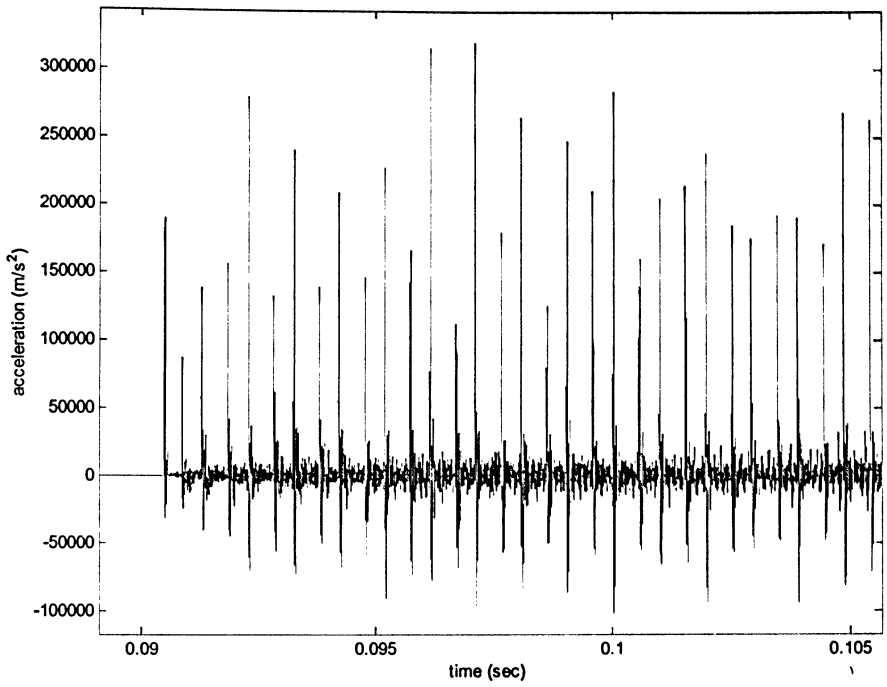

Figure 5-19 Mid-grain radial acceleration (axially fixed): ζ=0.25, 1.2-MPa pulse

The purpose of the next few simulations is to alter the damping ratio slightly, and observe its effects when compared to the previous simulation results. The damping ratio for most structural systems is not known and is typically found through empirical or trial-and-error approaches. This will directly illustrate how the damping ratio of the presented viscous damping model will affect the simulation, analogous to a trial-and-error approach. Three similar simulations are completed with damping ratios of 0.35, 0.45 and 0.65. Other damping ratios are tested, but are not included in this report. The head-end pressure-time and the propellant mid-grain radial acceleration-time profiles for each simulation are included in Figure 5-20 to Figure 5-25. From the three pressure plots, it becomes evident that, as the damping ratio is increased, the dc pressure rise decreases slightly, as one would typically expect. Also notice that as the damping ratio is increased, the magnitude of the post-shock oscillations decreased. This is a desired result, since excessive post-shock activity could be a resisting factor in the development of the sustained limit-amplitude shock wave. The limited sustained pressure peak-magnitude is not greatly affected by a change in the damping ratio. For all simulations the peak magnitude is between 2.5 MPa and 3 MPa.

By observing the three simulation acceleration plots, it is evident that the positive and negative peak-magnitudes decrease as the damping ratio is increased. In Figure 5-19 and Figure 5-21, the negative peaks reach values near -90,000 m/s^2, whereas in Figure 5-25 the negative peaks reach values of approximately -50,000 m/s^2. This decrease in acceleration peak-magnitude consequently reduces the burning rate augmentation and the energy transferred into the flow, thus affecting the wave development. Also as one would expect, the post-shock acceleration oscillations are lower in magnitude as the damping ratio is increased. This correlates well to the decrease in the magnitude of the post-shock pressure oscillation values. The steel outer-surface mid-grain radial acceleration results (not included) follow similar trends as do the propellant radial acceleration-time profiles. These results clearly indicate that the structural damping ratio affects the acoustic wave development in the SRM combustion chamber. Other factors such as the strength of the disturbance, the type of disturbance and the density of the FE mesh also influence the development of the wave activity. The following paragraphs will show this to a certain extent, with focus on the head-end pressure-time results for each simulation.

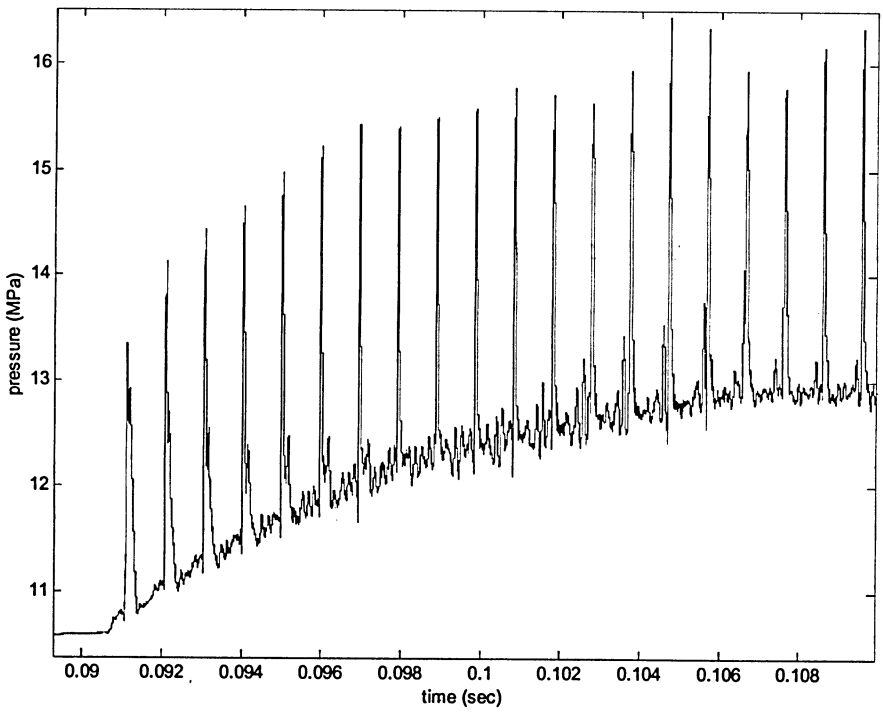

Figure 5-20 Head-end pressure (axially fixed): ζ=0.35

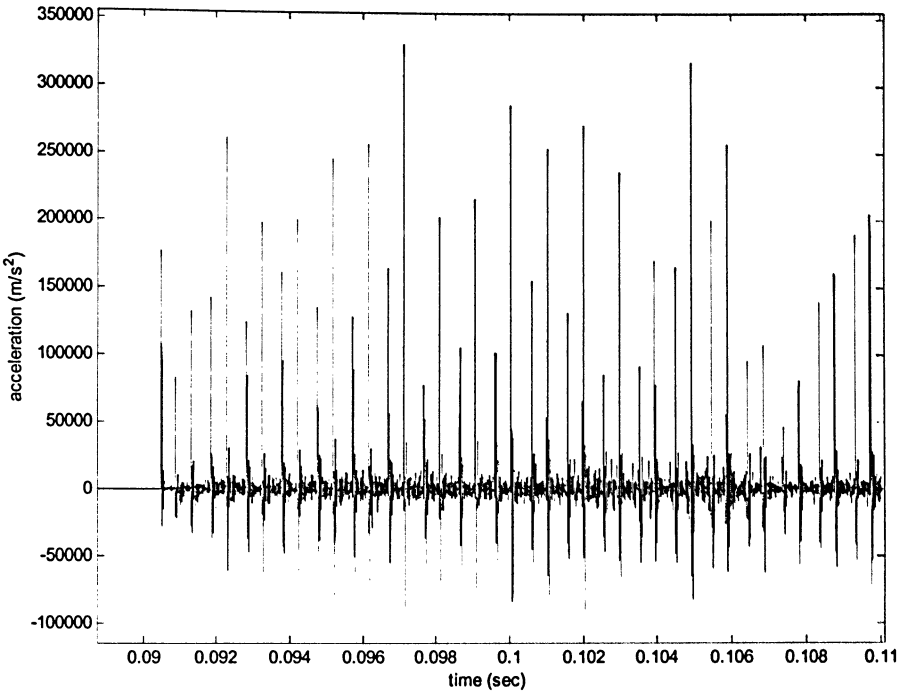

Figure 5-21 Mid-grain radial acceleration (axially fixed): ζ=0.35

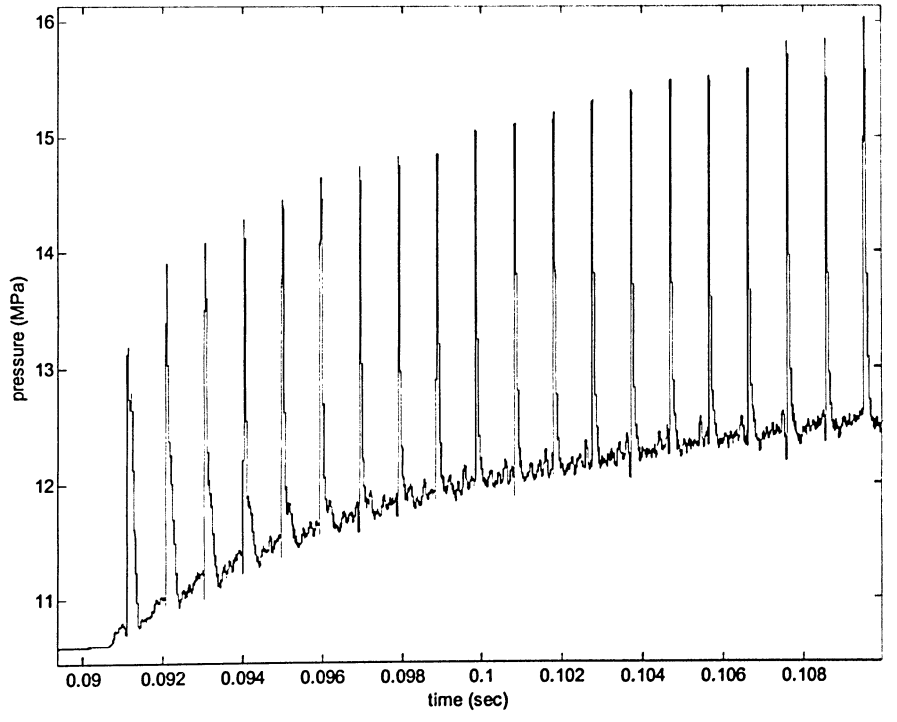

Figure 5-22 Head-end pressure (axially fixed): ζ=0.45

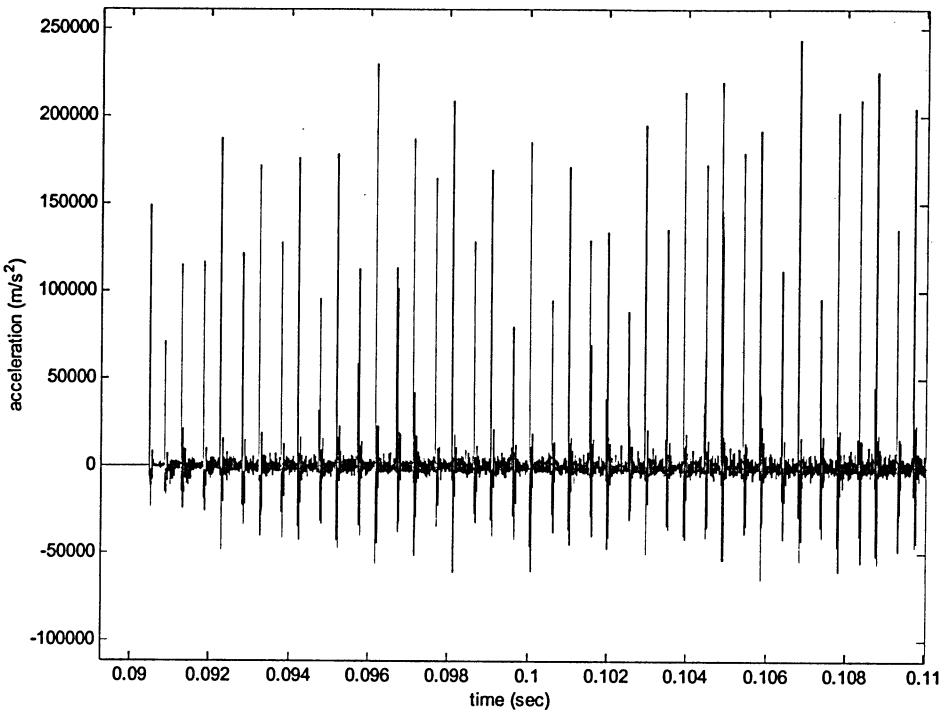

Figure 5-23 Mid-grain radial acceleration (axially fixed): ζ=0.45

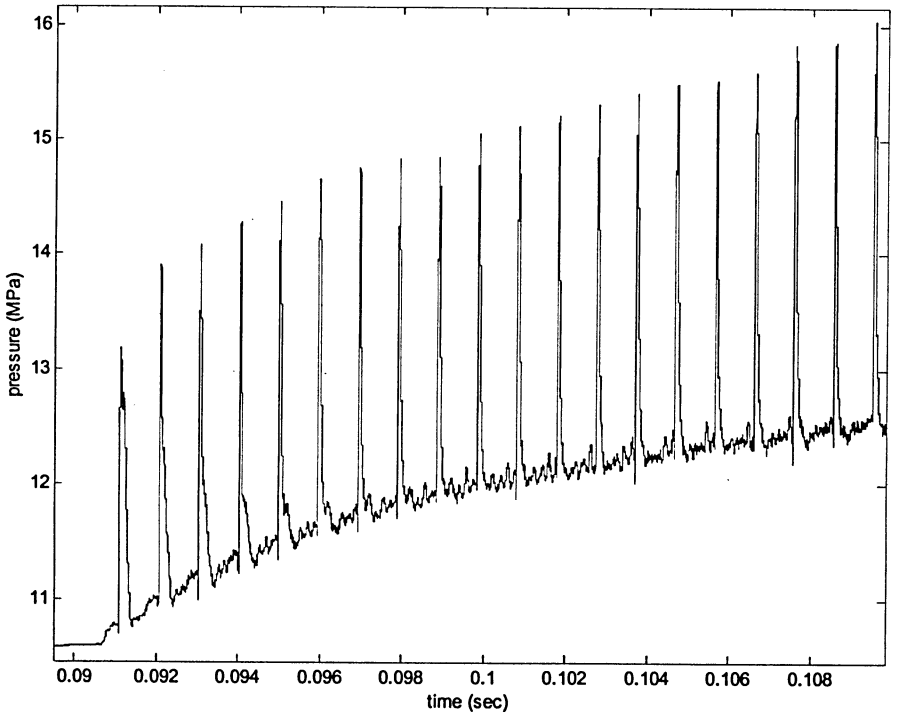

Figure 5-24 Head-end pressure (axially fixed): ζ=0.65

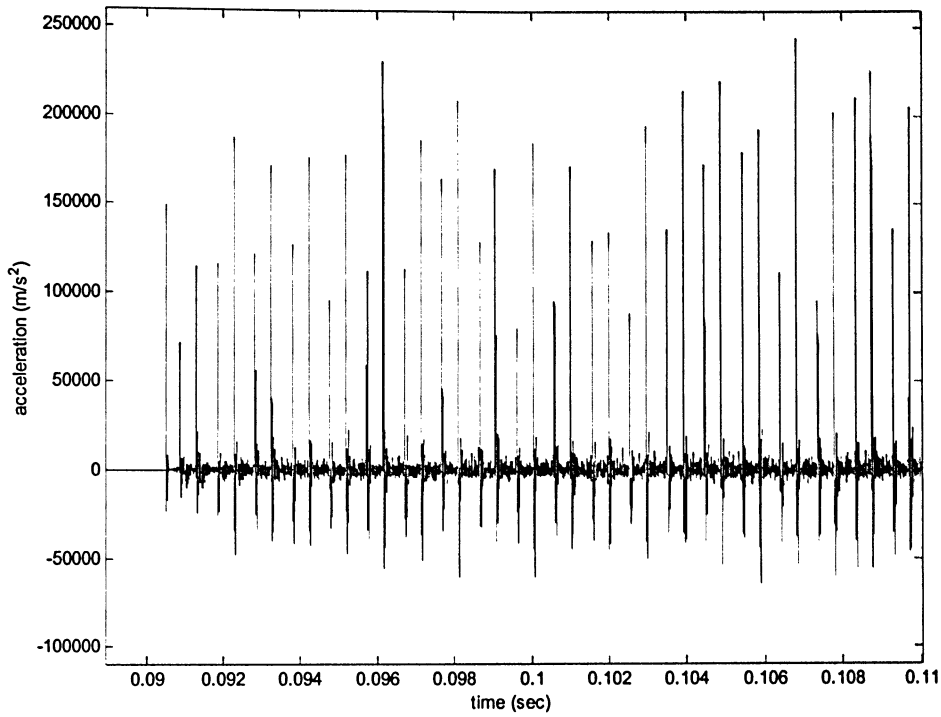

Figure 5-25 Mid-grain radial acceleration (axially fixed): ζ=0.65

5.2.2 Considerations for Disturbance Strength and Type

The next set of simulations involves changing of the disturbance or pulse strength. The disturbance used in the experimental results had a lower strength magnitude than that in the previously predicted results for the same motor. The reason for increasing the magnitude of the initial disturbance during the simulated firings is to have a similar wave system to the experimental runs, which is not feasible at very low pulse strengths. All completed simulations up to now have used pulse strengths of 1.2 MPa (~ 11% of the local base chamber pressure). These simulations involve pulse strengths set to 1.4 MPa, 1.0 MPa, 0.8 MPa and 0.6 MPa, below and above the previous value. The same simulation parameters are used as in the previous set of simulations, with the damping ratio set to 0.35.

Results of the motor head-end pressure-time profiles are included in Figure 5-26 to Figure 5-29. It becomes evident from observing the plots that no matter what the initial disturbance is development into the same sustained limited-wave system occurs in every

case. Note that for pulse strengths below 0.4 MPa, a sustained limited-wave system did not result and is not included here. For each pulse-strength, the dc shift is similar at 2.5 MPa, and the limited peak magnitude is approximately 3 MPa, which is comparable to the 1.2-MPa pulse results in Figure 5-20. Notice, however, that as the strength of the pulse decreases, the increase in base pressure occurs at a more gradual rate. Also, as the pulse strength is reduced, the initial peak magnitudes are lower and the increase in wave amplitude is also more gradual. The results using lower pulse strengths are more consistent with the experimental data in Reference 1; the experimental firings were pulse-triggered into instability using a pulse-strength of approximately 5% of the base pressure (about 0.55 MPa). It is clear with the current simulation model that a limited amplitude sustained wave can result with lower pulse strengths. This was not the case with previous numerical simulations involving the same motor configuration,[1, 32] where a larger pulse strength was necessary to sustain a wave system. This is seen as an improvement in the development of the simulation model.

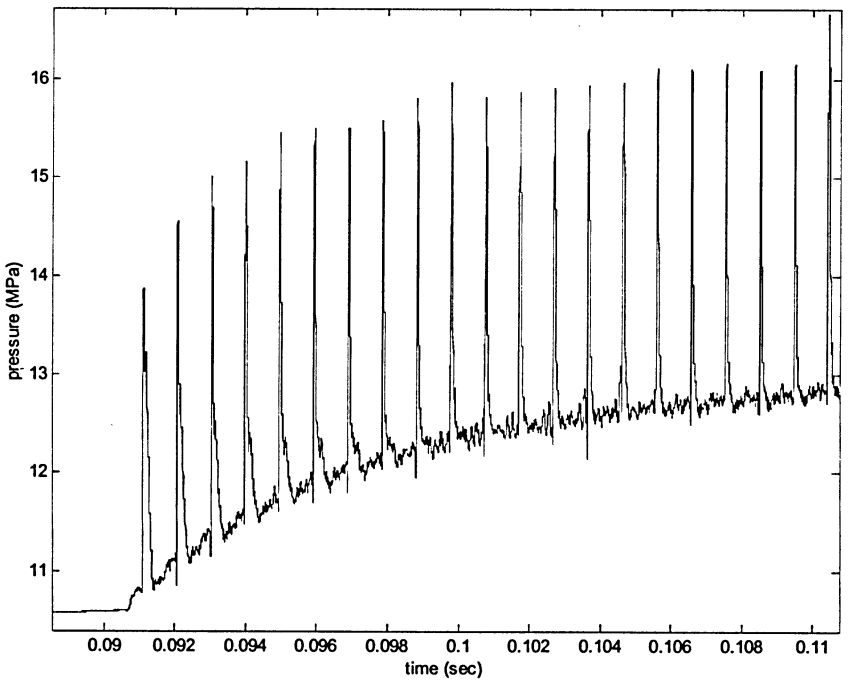

Figure 5-26 Head-end pressure: 1.4-MPa pulse

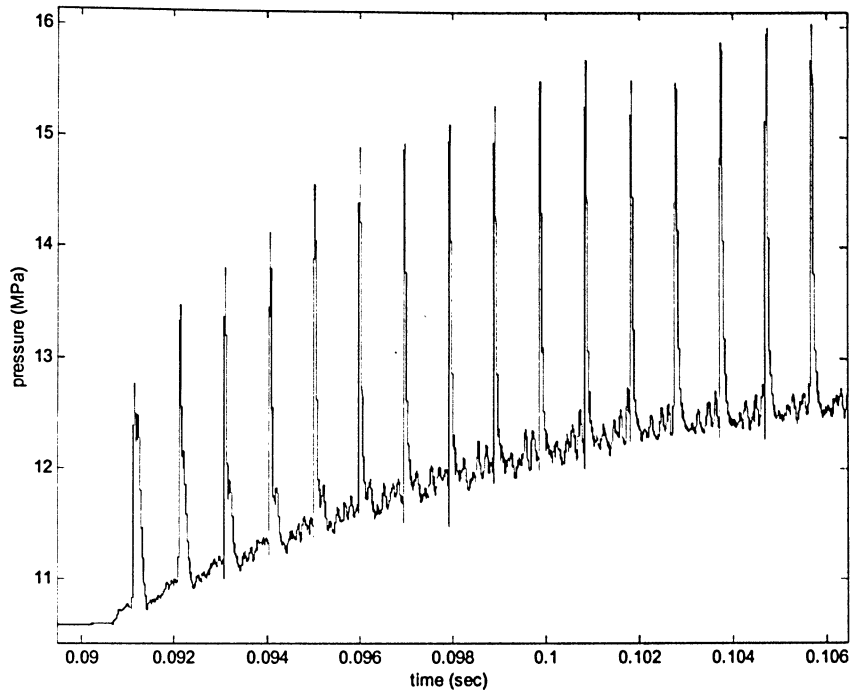

Figure 5-27 Head-end pressure: 1.0-MPa pulse

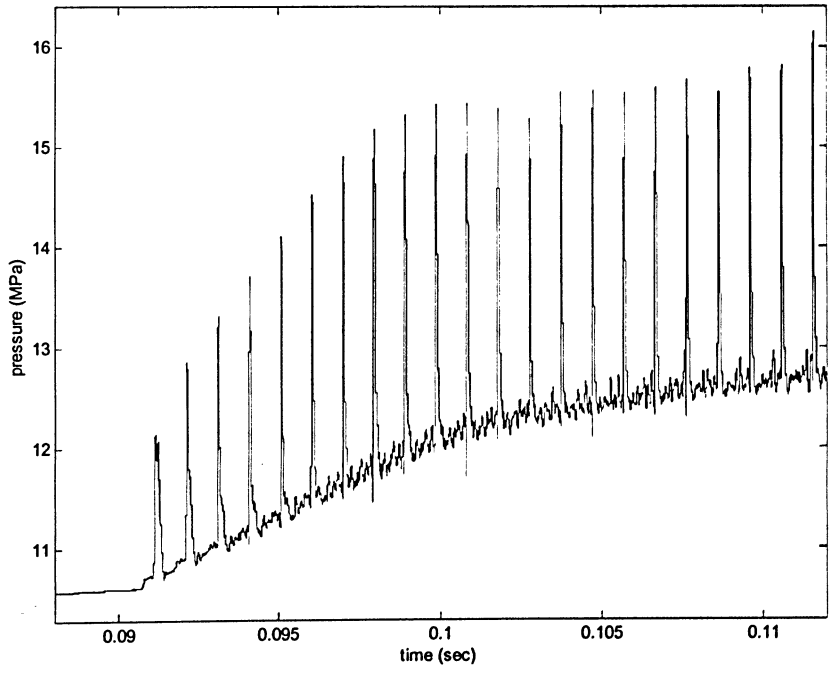

Figure 5-28 Head-end pressure: 0.8-MPa pulse

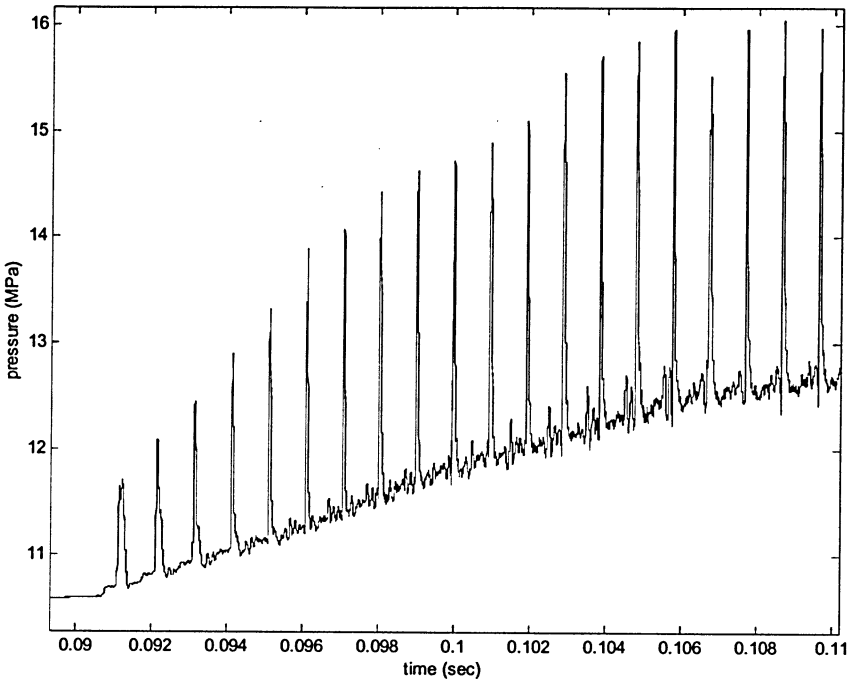

Figure 5-29 Head-end pressure: 0.6-MPa pulse

The next simulation consists of the use of the original disturbance pulse in lieu of the shock-fronted disturbance used in the previous simulations. The pulse strength is set to 1.2-MPa and a structural damping ratio of 0.35 is employed. The base pressure rise and sustained limit-cycle magnitude is approximately the same when compared to Figure 5-20, for this particular simulation. However, when using the original disturbance, a secondary low amplitude wave is evident in the early stages of the shock wave cycle, as shown in Figure 5-30. This secondary wave eventually dissipates and is no longer a factor in the simulation. With the shock-fronted disturbance, there is no secondary wave in the same simulation, which is consistent with the experimental firings. In this study, a secondary wave is not preferred, mainly because its effects in the earlier simulations during the development of the numerical model caused excessive oscillations with the acoustic and structural response. This is an important point to note, since the disturbance routine itself should be as close as possible to the pulse used in the experimental firings, for data comparison.

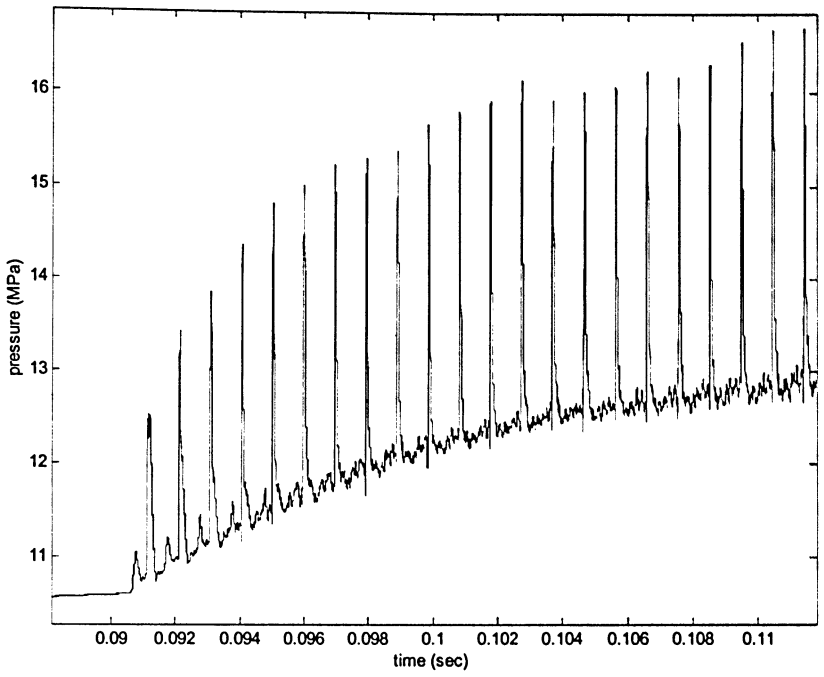

Figure 5-30 Head-end pressure: 1.2-MPa pulse, ζ=0.35, original pulse

5.2.3 Detailed Results

From the results presented in Sections 5.2.1 and 5.2.2, it seems evident that the simulation results with a damping ratio of 0.35, a pulse strength of 0.6 MPa and the shock-fronted disturbance have provided results that are more comparable to the experimental firings (based on the dc shift and the shock-front development). The head-end pressure profile was discussed and shown in Figure 5-29, with the remaining results included in full in Figure 5-31 to Figure 5-34. The mid-grain sleeve radial acceleration peaks shown in Figure 5-31 are comparable to the experimental results, with peak magnitudes of approximately $\pm$5000 m/s^2 when the wave cycle is fully developed. Also, the inner propellant surface negative radial acceleration peaks at the motor mid-grain shown in Figure 5-32 correspond well to previous numerical simulations.[32] The peaks of the propellant mid-grain burning rate profile shown in Figure 5-33 correspond well with the negative peaks in Figure 5-32, according to the burning rate theory presented. Also included in Figure 5-34 is the head-end propellant inner surface radial displacement-time profile. The structural response to the

applied head-end pressure is shown with the consistent peaks in both plots, which is not surprising. More importantly, it should be noted that the acoustic frequency between shock cycles (i.e., the pressure oscillation frequency from Figure 5-29) is approximately the same as the motor structural response frequency. This was also found with respect to the experimental firings and is a key factor in the success of the presented simulations.

The ability of the three simulation model components (i.e., structure, fluid and combustion) to couple successfully have been illustrated with the results presented in this section. Based on the propellant acceleration profiles, the propellant burning rate has been augmented to provide the energy necessary to sustain the acoustic wave system. In the next section, considerations for altering of the structural geometry and material properties, and the corresponding effects on the simulation results, are discussed.

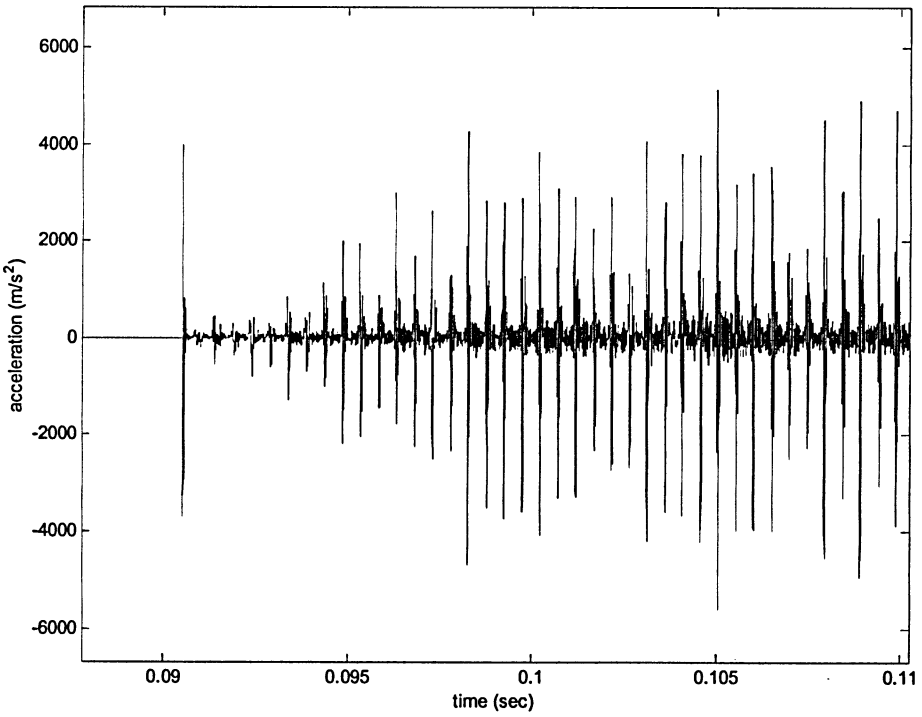

Figure 5-31 Steel radial acceleration: 0.6-MPa pulse, ζ=0.35, shock-fronted pulse

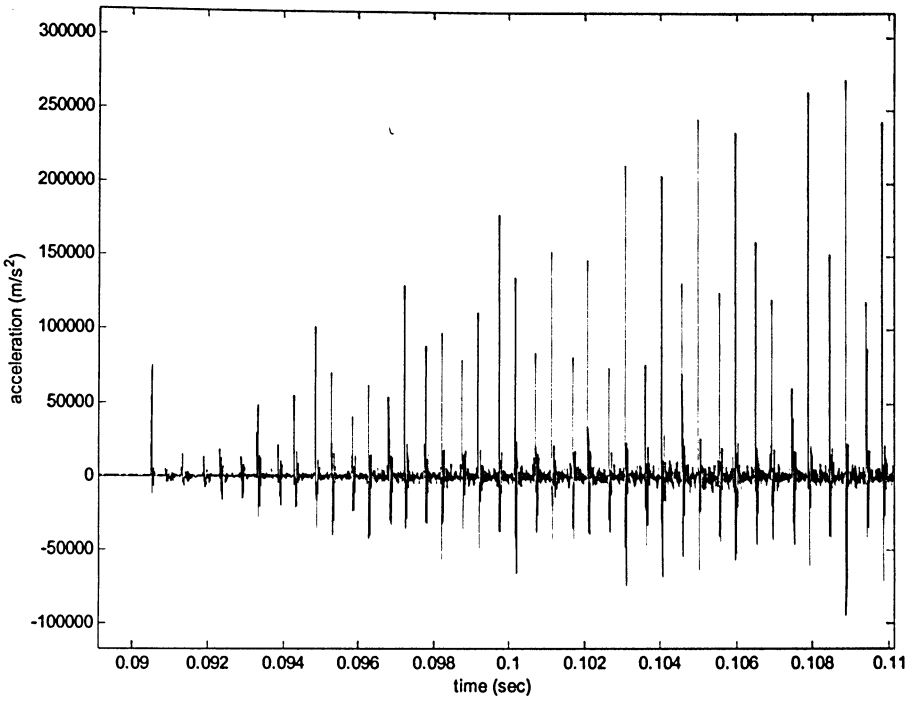

Figure 5-32 Propellant radial acceleration: 0.6-MPa pulse, ζ=0.35, shock-fronted pulse

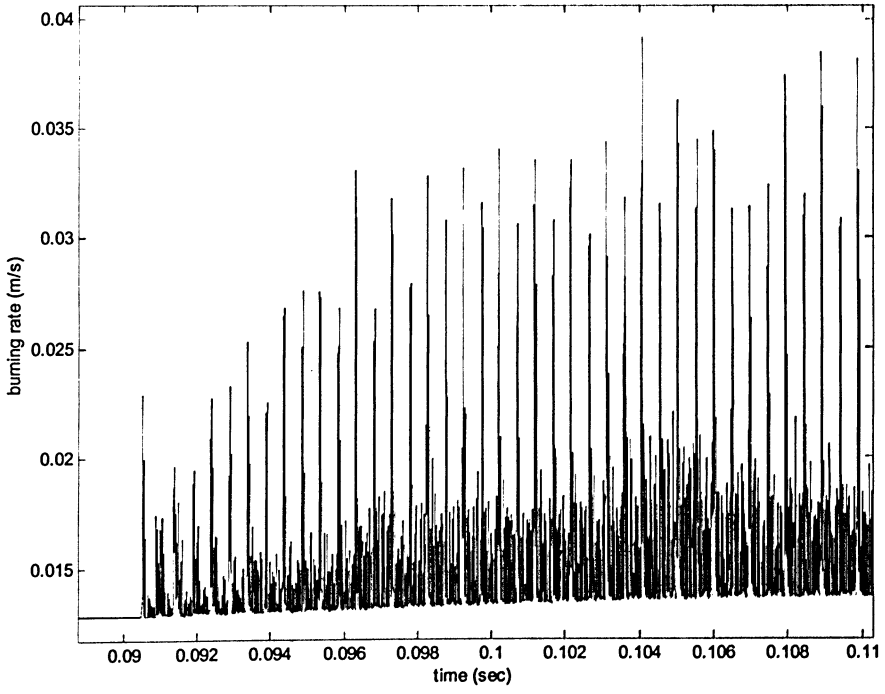

Figure 5-33 Propellant burning rate: 0.6-MPa pulse, ζ=0.35, shock-fronted pulse

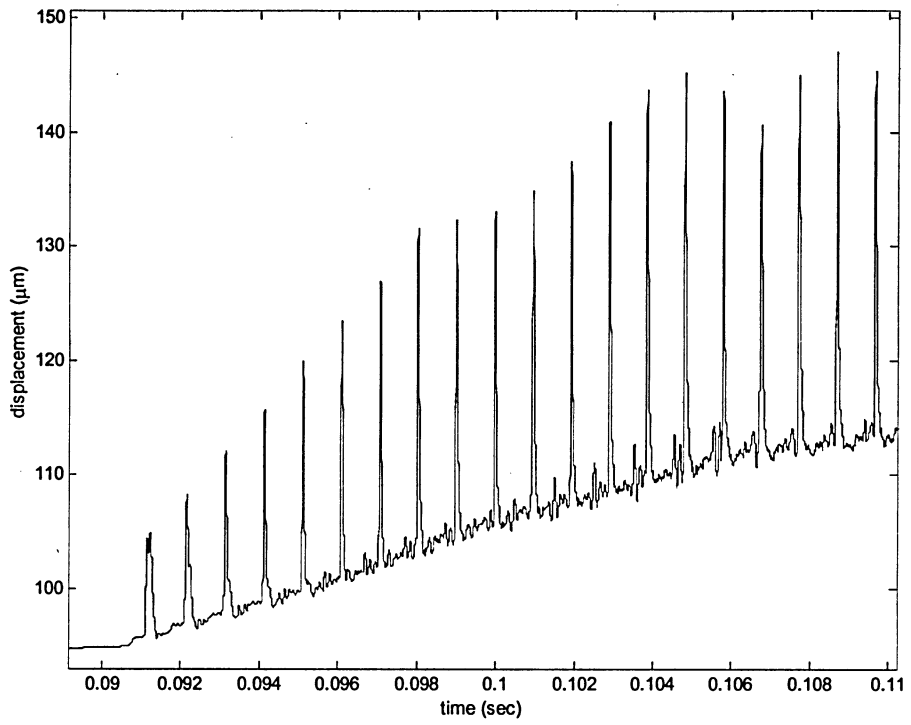

Figure 5-34 Propellant radial displacement: 0.6-MPa pulse, ζ=0.35, shock-fronted pulse

5.3 *Alternate Simulated Firings*

The purpose of this section is to further illustrate how the structure affects the simulation and the limited wave system in the SRM chamber. The *reference* simulation is that given in Section 5.2.1, where the damping ratio is set to 0.35 and the pulse-strength is 1.2-MPa. The corresponding pressure profile was shown in Figure 5-20. Two simulations are included here, where in the first simulation the steel sleeve thickness is increased to 1.41 cm (versus 0.467 cm). In the second simulation, the steel sleeve is replaced with an aluminium sleeve of identical geometry, with material properties the same as those of the motor casing.

The motor head-end pressure-time profiles for the thick-sleeve geometry and the aluminium sleeve are shown in Figure 5-35 and Figure 5-36, respectively. The dc shift and limited wave peak magnitudes are both similar to the reference simulation, with the aluminium sleeve simulation having slightly higher peak magnitudes than in the thick

sleeved case. The change in the sleeve thickness and material does not affect the wave development drastically, as was seen with the experimental firings using sleeves of varying thicknesses.[1] This is most likely due to the fact that the propellant web thickness remains fairly large when the disturbance is introduced. The propellant mid-grain inner surface radial acceleration peaks are shown in Figure 5-37 for the thick sleeve simulation and are similar in magnitude in comparison with both the thinner sleeve and aluminium cases. This corresponds to a similar burning rate augmentation, which is the reason the acoustic activity remains the same (i.e., similar dc shift). Also, the mid-grain sleeve outer radial acceleration peaks for the thicker sleeve are lower versus the thinner sleeve ($\pm 3000 m/s^2$ versus $\pm 6000 m/s^2$). The aluminium sleeve radial acceleration peaks are higher versus the reference simulation ($\pm 10{,}000 m/s^2$).

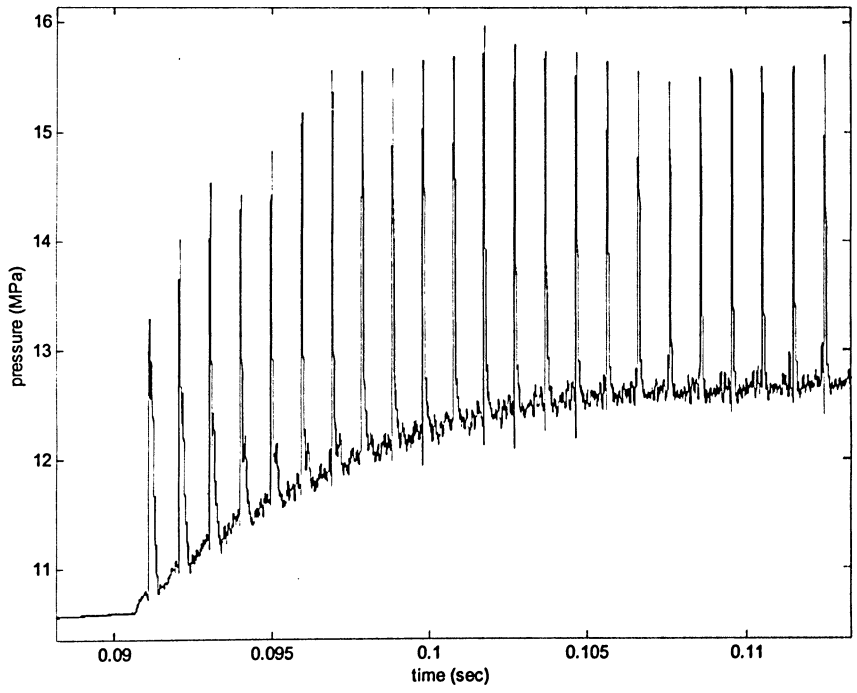

Figure 5-35 Head-end pressure: thicker sleeve

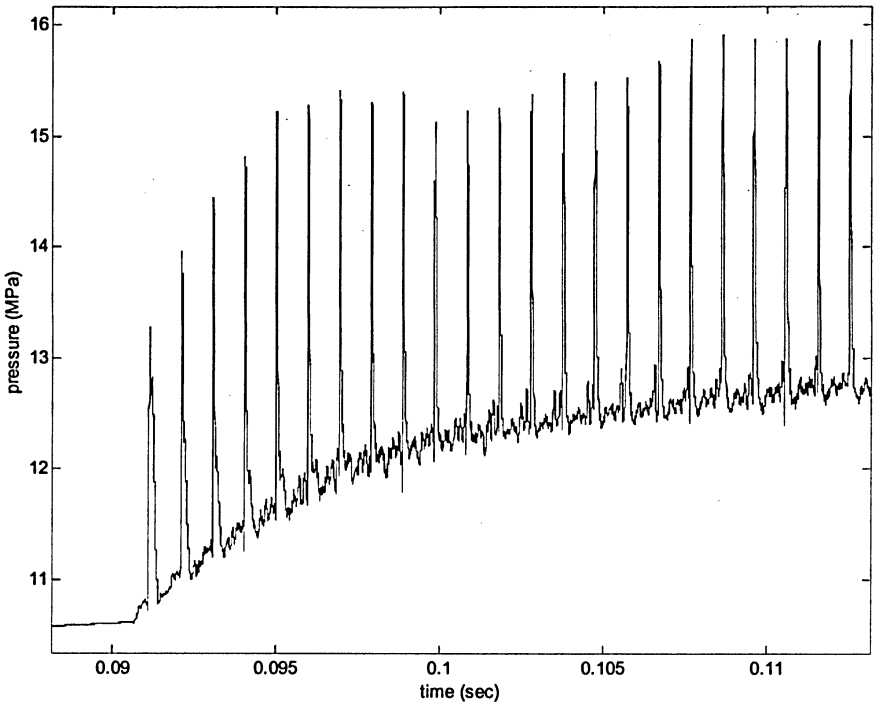

Figure 5-36 Head-end pressure: aluminium sleeve

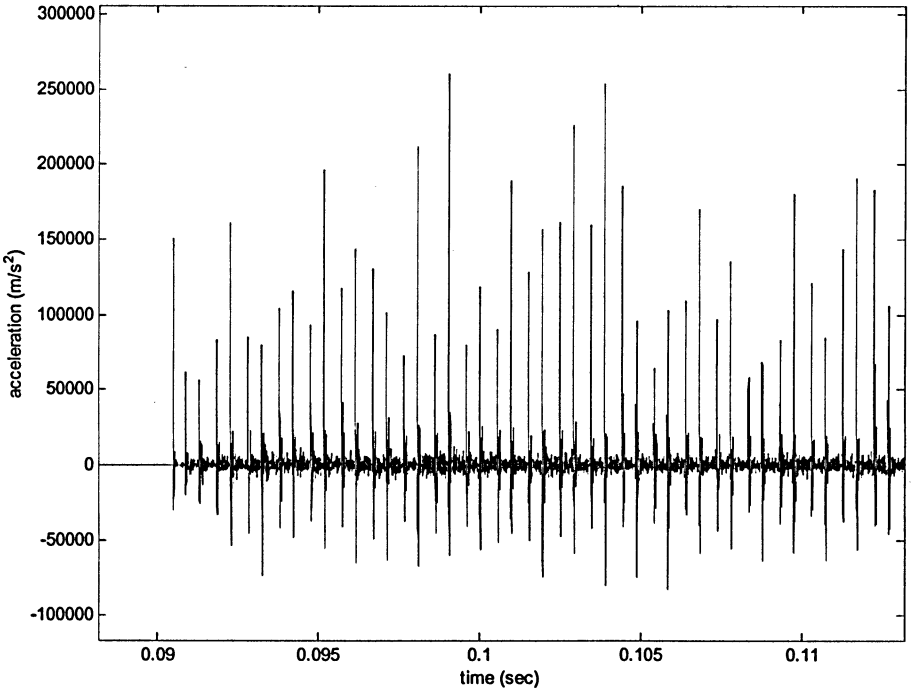

Figure 5-37 Propellant surface radial acceleration: thicker sleeve

6 Conclusion

6.1 Final Remarks

The predictive capability of the present numerical model has been demonstrated through the simulated cylindrical-grain motor firings, with the presented results illustrating the coupled effects of the simulation components. Considerations for modeling the unsteady nonlinear behaviour of SRMs have also been demonstrated through the results presented in Section 5.1. Through the simulation comparison of the two hexahedral elements, the sensitivity of the simulation to various modeling parameters is illustrated. The 8-node elements seem to be better suited for this application, possibly due to the low shear stresses experienced by the structure (quadratic-displacement elements are typically used for high-shear applications). The density of the FE mesh also proves to be a large factor in influencing the simulation results, as is the damping model employed. Generally, the simulations involving a Rayleigh damping model structurally respond more accurately; however, due to the time limitations, a coarse mesh is required and not sufficient in representing the structure. Conversely, the explicit formulation with mass-proportional damping allows for implementation of a refined mesh with computational efficiency, but with somewhat reduced accuracy. An implicit method including quicker computational capabilities with a refined FE mesh, or an explicit method with Rayleigh damping capabilities, could potentially remedy this issue (in Reference 15, an alternative formulation for the central difference method is presented; this was tested with the simulation components but is far too slow due to small time step restrictions). This is an obvious short-coming of the presented numerical model and algorithm.

The shock-front is not sustained with the refined FE mesh simulations, possibly due to the high axial response and acceleration of the propellant surface, which was not modeled in previous simulation attempts.[1, 32] Also, the numerical model may not be capturing the correct physical behaviour of the motor (possibly due to model simplifications or some sort of 'lagged' axial response not modeled) potentially causing the shock-front to decay.

However, the shock-front is sustained to a limited amplitude system when the propellant is fixed from moving in the axial direction. These results indicate good correlations to experimental data involving the same cylindrical-grain motor configuration. A parametric analysis involving the structural damping ratio and the pulse strength show some basic trends with the simulation model. Success with these simulations may be attributed to the fact that the reduced axial response and acceleration of the motor structure are not dissipating the shock-front, as indicated by the reduced solution noise in the radial acceleration-time and head-end pressure-time profiles. These results are analogous to the predicted results in References 1 and 32.

The alternate simulated firings presented in Section 5.3 further enforce the numerical model capabilities for SRM combustion instability analysis. The effects of changing the external sleeve structure geometry are illustrated and comparable to the experimental firings for the same motor. Furthermore, the effects of changing the external steel sleeve to an aluminium sleeve are shown, and not surprisingly, due to the motor propellant configuration, little change in the resulting behaviour was observed.

The main objectives of this study have been achieved. The effects of the structural response and acceleration field on the burning rate, and thus on the development of SRM nonlinear axial combustion instability symptoms, have been shown. A better understanding of the physical phenomena related to SRM combustion instability is a direct product of the various simulation results. The modeling insight gained in this study can be used for further improvement of the numerical model predictive capabilities and for the development effort as discussed in the subsequent section.

6.2 Recommendations for Future Work

Potential future work with modeling of the numerical simulation components may include the addition of structural nonlinearities. This pertains solely to the propellant structure, which, as mentioned, may exhibit nonlinear viscoelastic material behaviour. A

viscoelastic material model may provide the necessary response to sustain the axial shock-front by providing structural stiffness that is dependent on the exhibited strain or strain-rate (i.e., the stiffness matrix as a function of displacement, and thus time). Also, geometric nonlinearities due to the almost incompressible material may also be considered for modeling. Further considerations for structural modeling include adding the regression of the FE propellant mesh during the unsteady portion of the simulation, which would model any changes in material properties and damping. Elements with transient capabilities would be required for a successful implementation; however, time then becomes an issue. Other considerations with respect to structural modeling are to include a non-rigid nozzle structure in the FE mesh and to have a more detailed model of the motor head-end structure. Also, considerations for accurately determining the system damping ratio are necessary due to the very different damping properties of the propellant and surrounding structure (aluminium casing and external sleeve). Finally, the use of different elements may also be considered.

With respect to modeling of the core flow, a three-dimensional CFD component may be included to represent the IBF. This may potentially include any transverse (radial and/or tangential) waves in the motor chamber, which may act to assist with the axial wave development. Transverse waves in SRMs have been known to oscillate at a much higher acoustic frequency than axial waves. Other modeling considerations include the use of a more sophisticated burning rate model. A combustion model with transient or frequency-dependent capabilities may also support axial wave development, potentially accounting for any lagging in the structural response. This model may also respond better to the structural acceleration oscillations, potentially minimizing the numerical effects of such response.

The aforementioned modeling suggestions may help to provide more accurate simulated firings and a better representation of the physical motor behaviour. Other considerations are with the actual simulations themselves. The application of the present model to different grain geometries, such as star-, wagon-wheel- or dog-bone-grains, may also be considered. Moreover, different grain compositions such as the addition of particles may also be considered. Also, changing the speed of the propellant regression (i.e., through the burn rate coefficient) to provide a different base pressure and changing the nozzle throat

diameter can be simulated. Furthermore, testing a motor in-flight without an external sleeve, testing of various sleeve geometries and materials, pulse-triggering the motor at a different propellant web-thickness, or applying angular spin to the motor structure may also be tested. The possibilities are endless and are left for the reader to explore.

References

1. Greatrix, D.R. and Harris, P.G. "Structural Vibration Considerations for Solid Rocket Internal Ballistics Modeling", AIAA/ASME/SAE/ASEE 36th Joint Propulsion Conference, AIAA Paper No. 2000-3804, Huntsville, July 17-19, 2000.

2. Greatrix, D.R. "Transverse Vibration and Rocket Combustor Internal Ballistics", AIAA/ASME/SAE/ASEE 33rd Joint Propulsion Conference, AIAA Paper No. 97-3338, Seattle, July 7-9, 1997.

3. Blomshield, F.S. and Beiter, C.A. "Nonlinear Stability Testing and Pulsing of Full Scale Tactical Motors", AIAA/ASME/SAE/ASEE 27th Joint Propulsion Conference, AIAA Paper No. 91-1953, June 22-26, 1991.

4. Sutton, G.P. and Biblarz, O., Rocket Propulsion Elements, 7th ed., John Wiley and Sons Inc., New York, 2001.

5. Greatrix, D.R. "Structural Vibration and Solid Rocket Combustion Instability", *Canadian Aeronautics and Space Journal*, Vol. 44, No. 1, March 1998, pp. 9-24.

6. Chopra, H.S., Greatrix, D.R. and Kawall, J.G. "Transient Shock Wave Interaction With Rocket Nozzle – Cold-Flow Study", AIAA/ASME/SAE/ASEE 39th Joint Propulsion Conference, AIAA Paper No. 2003-4669, Huntsville, 2003.

7. Gottlieb, J.J. and Greatrix, D.R. "Numerical Study of the Effects of Longitudinal Acceleration on Solid Rocket Motor Internal Ballistics", *Journal of Fluids Engineering*, Vol. 114, No. 3, Sept. 1992, pp. 404-410.

8. Greatrix, D.R. "Parametric Analysis of Combined Acceleration Effects on Solid Propellant Combustion", *Canadian Aeronautics and Space Journal*, Vol. 40, No. 2, 1994, pp. 68-73.

9. Greatrix, D.R. "Combined Structural Oscillation Effects on Solid Rocket Internal Ballistics", AIAA/ASME/SAE/ASEE 35th Joint Propulsion Conference, AIAA Paper No. 99-2509, Los Angeles, June 20-24, 1999.

10. Loncaric, S., Greatrix, D.R. and Fawaz, Z. "Star-Grain Rocket Motor – Nonsteady Internal Ballistics", *Aerospace Science and Technology*, Vol. 8, No. 1, January 2004, pp. 47-55.

11. Parsons, I.D. *et al.* "Fluid-Structure Interaction through a Non-material Interface: Simulations of Solid Rocket Motors". CDROM Proceedings of the 14th ASCE Engineering Mechanics Conference (EM2000), Austin, Texas, May 2000.

12. Majdalani, J. and Flandro, G.A. "Some Recent Developments in Rocket Core Dynamics", AIAA/ASME/SAE/ASEE 39th Joint Propulsion Conference, AIAA Paper No. 2003-5112, Huntsville, 2003.

13. Greatrix, D.R. "Fluid-Structure Interactions in Solid Rocket", 9th Aerodynamics Symposium, 49th Annual CASI Conference, Montreal, April 28-30, 2003.

14. Callister Jr., W.D. Material Science and Engineering: An Introduction, 5th ed., John Wiley and Sons, New York, 2000.

15. Cook, R.D., Malkus, D.S. and Plesha, M.E. Concepts and Applications of Finite Element Analysis, 3rd ed., John Wiley and Sons Inc., New York, 1989.

16. Petyt, M. Introduction to Finite Element Vibration Analysis. Cambridge University Press, Cambridge, UK, 1990.

17. ANSYS Finite Element Program Ver. 5.5, ANSYS Inc., Houston, PA.

18. Craig Jr., R.R. Mechanics of Materials, 2nd ed., John Wiley and Sons, New York, 2000.

19. Bathe, K.J. Finite Element Procedures. Prentice Hall, New Jersey, USA, 1996.

20. Meguid, S.A. "The Finite Element Method in Mechanical Engineering", Department of Mechanical and Industrial Engineering, Internal Report, University of Toronto, Canada. September, 1999.

21. Thomson, W.T. and Dahleh, M.D. Theory of Vibration with Applications, 5th ed., Prentice Hall, Upper Saddle River, New Jersey, 1998.

22. Greatrix, D.R. and Kudriavtsev, V. "Modeling of Structural Vibration for Motor Chamber Internal Flow Studies", ASME Pressure Vessels and Piping Conference, Vancouver, Aug. 4-8, 2002.

23. Boresi, A.P. and Schmidt, R.J. Advanced Mechanics of Materials, John Wiley and Sons, New York, 2003.

24. Nise, N.S. Control Systems Engineering, 3rd ed., John Wiley and Sons, New York, 2000.

25. Greatrix, D.R. and Gottlieb, J.J. "Erosive Burning Model for Composite-Propellant Rocket Motors with Large Length-to-Diameter Ratios", *Canadian Aeronautics and Space Journal*, Vol. 33, No. 3, Sept. 1987, pp. 133-142.

26. Glimm, J. "Solution in the Large for Nonlinear Hyperbolic Systems of Equations", *Communications in Pure and Applied Mathematics*, Vol. 18, 1965, pp. 697-715.

27. Ben-Artzi, M. and Falcovitz, J. "An Upwind Second-Order Scheme for Compressible Duct Flows", *SIAM Journal on Scientific and Statistical Computing*, Vol. 7, No. 3, July 1986, pp. 744-768.

28. Sod, G.A. "A Numerical Study of a Converging Cylindrical Shock", *Journal of Fluid Mechanics*, Vol. 83, 1977, pp. 785-794.

29. Greatrix, D.R. and Gottlieb, J.J. "Higher-Order Random-Choice Method for Internal Ballistic Flows", 7th Annual Conference of the CFD Society of Canada (CFD99), May 30 – June 1, 1999.

30. Burden, R.L. and Faires, J.D. Numerical Analysis, 6th ed, Brooks/Cole Pub. Co., Pacific Grove, CA, 1997.

31. Leyland, P. *et al.* "Fully Coupled Fluid-Structure Algorithms". Fluid-Structure Interaction. Kogan Page Science, London, 2003, pp. 137-178.

32. Loncaric, S. "Internal Ballistic Modeling of a Star-Grain Solid Rocket Motor". Master's Thesis, Ryerson University. December, 2002.

Appendix A

The algorithm for this study consists of three main components: the FE structural solver, the IBF solver and the burning rate or combustion solver. The source code listing is far too long to include in its entirety, thus only schematic representations of the algorithm are included in the thesis. The burning rate and IBF algorithm schematics were shown in Figure 3-5 and Figure 3-6, respectively. Also, the overall simulation schematic was shown in Figure 4-5. The objective here is to show the schematic of the FE structural solver. The FE structural algorithm was written in FORTRAN (as were the rest of the simulation components), with the details of the structural component discussed in Chapter 2. A flow chart outlining the main elements of the structural component and its typical operation is included in Figure A- 1, details of which will now follow.

The first part of the FE component in a simulation is to read the input file data and initialize the size of arrays and vectors. Since the density of the FE mesh (i.e., number of elements) governs the size of the arrays, the dynamic memory allocation option available in FORTRAN was utilized. This enabled the arrays to be exact sizes depending on the number of nodes and the total degrees-of-freedom for the system. The algorithm then scans the FE mesh to determine the nodes and elements on the propellant inner boundary; this assists with applying external loads and constraints and regressing the appropriate nodes in the FE mesh. Next, the FE mesh element calculations are performed and the element mass, stiffness and force vectors are determined and stored appropriately. At this point, an optional static and free vibration analysis can be performed. The algorithm then initializes the transient routines by determining the system damping coefficients (α and β) and, for explicit methods, calculating the time step size. The transient calculations continue depending on the type of time integration method chosen, while the main loop denoted by the iteration variable 'TSTOP' is repeated in-between the IBF half-time steps depending on the parameter value of T_{sub}. The force vector calculations are performed at every iteration due to the continuous changing of the applied external loading, as are the regression of the propellant and the interpolation of the flow and structural parameters (done by the FSI interface component).

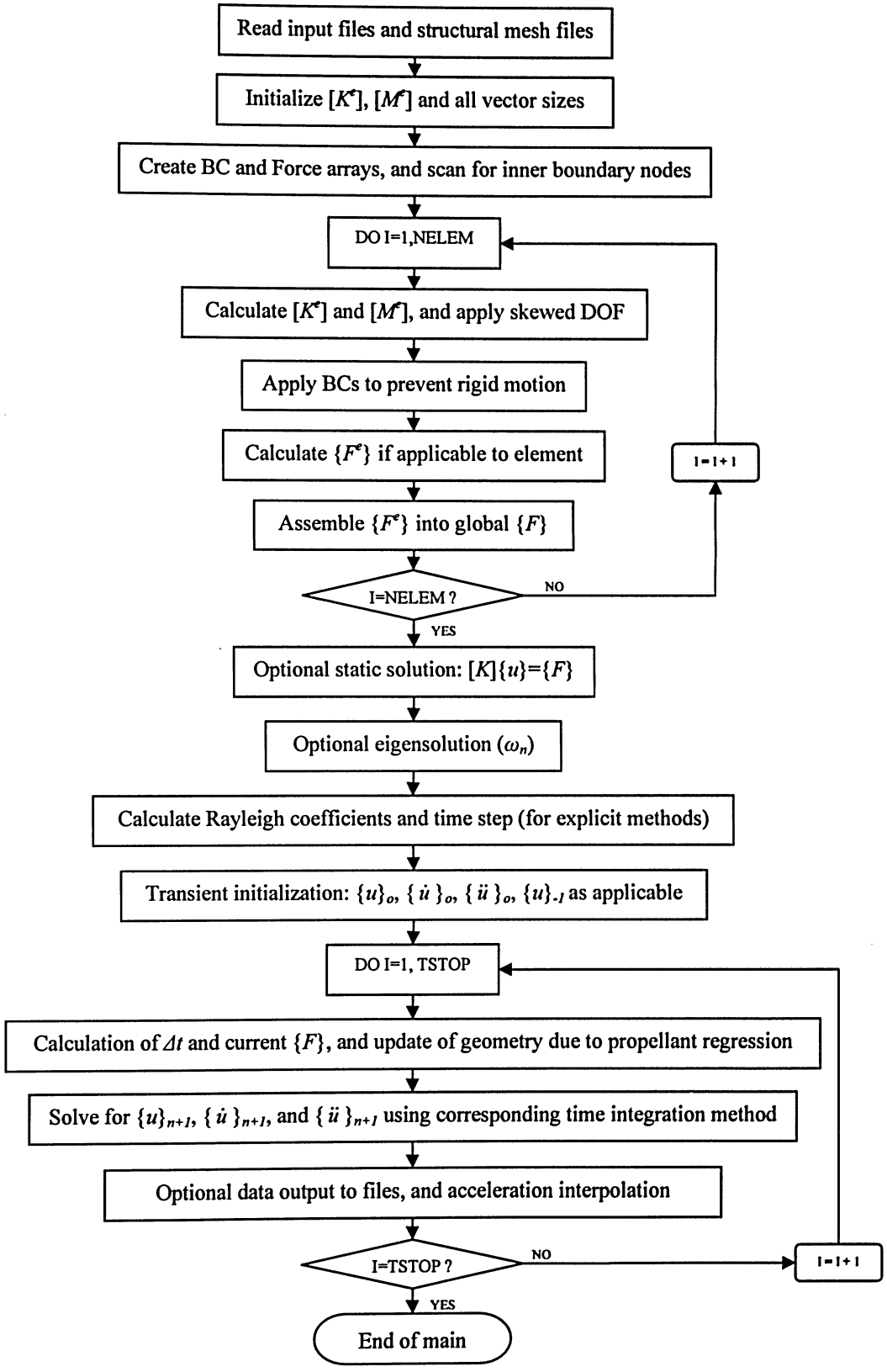

Figure A- 1 FE component algorithm solution schematic

The options available in the FE structural code such as the choice of static or free vibration analysis, the system damping ratio and natural frequencies, the numerical constants (γ and β), the mass matrix, the time integration method, the damping model and the FE Courant number are governed by the data in the FE input file. These options are determined at discrete points in the algorithm, and the solution procedure follows accordingly. Also, the FE mesh (nodal coordinates and element connectivity) and material data (elastic modulus, material density and Poisson's ratio) are read by the algorithm via input files. The data output to files (shown in the flow chart) is usually performed every iteration and includes variables such as the nodal displacements and accelerations at particular locations on the motor structure. These variables are all listed as arrays in the output files, which can be input to any graphing program for plotting purposes.